Chapter 4
Power-Stroke-Driven Muscle Contraction

Raman Sheshka and Lev Truskinovsky

Abstract To show that acto-myosin contraction can be propelled directly through a conformational change, we present in these lecture notes a review of a recently developed approach to muscle contraction where myosin power-stroke is interpreted as the main active mechanism. By emphasizing the active role of power stroke, the proposed model contributes to building a conceptual bridge between processive and nonprocessive motors.

4.1 Introduction

Broadly accepted chemo-mechanical models of muscle contraction operate with kinetic constants depending on a continuous variable, the elongation of an effective spring. This leads to an appearance of phenomenological functions, which brings into the theory an infinite number of parameters. In an attempt to avoid such 'freedom' we make a tacit assumption that the structural elements of force producing machinery are purely mechanical and can be in principle built in a lab.

To model the phenomenon of muscle contraction at a purely mechanical level we follow the approach developed in the theory of Brownian ratchets which replaces the conventional chemistry-based interpretation of active force generation by the study of Langevin dynamics of mechanical systems. In ratchet-based models describing acto-myosin contraction, the ATP activity is usually associated with actin binding potential while the power-stroke mechanism, residing inside myosin heads, is viewed as passive. Instead, in view of the reasons discussed below, we assume that power-stroke is the main active mechanism. Implicitly, our basic assumption is that

R. Sheshka
NeoXam, Paris, France

L. Truskinovsky (✉)
ESPCI, PMMH, CNRS – UMR 7636 PSL-ESPCI, Paris, France
e-mail: lev.truskinovsky@espci.fr

A. DeSimone et al., *The Mathematics of Mechanobiology*,
Lecture Notes in Mathematics 2260, https://doi.org/10.1007/978-3-030-45197-4_4

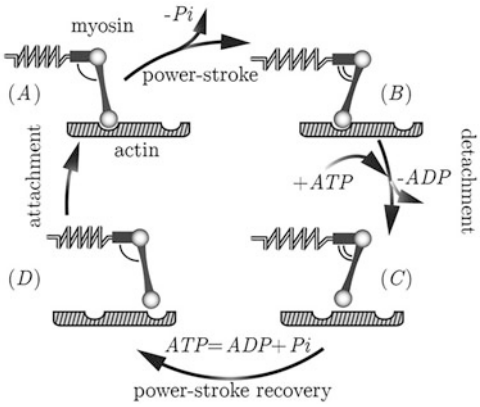

Fig. 4.1 Schematic illustration of the four-step Lymn–Taylor cycle showing the power-stroke $A \rightarrow B$, the detachment $B \rightarrow C$, the re-cocking of the power-stroke $C \rightarrow D$ and the final re-attachment $D \rightarrow A$ bringing the system back into the original state

the fundamental mechanism behind active force generation is the same in the linear molecular motors (myosins, kynesins, dyneines).

Muscle contraction takes the form of a relative motion of thick (myosin) and thin (actin) filaments [3]. Active force generation results from stochastic interaction between individual myosin heads (cross-bridges) and the adjacent actin binding sites. It includes cyclic attachment of myosin cross-bridges to actin filaments together with a concurrent conformational change in the core of the myosin catalytic domain (of folding-unfolding type). A lever arm amplifies this structural transformation producing the power-stroke, which allows the attached cross bridges to generate macroscopic forces [53].

Myosin motors convert chemical energy into mechanical work by catalyzing the hydrolysis of adenosin triphosphate (ATP) to the adenosine di-phosphate (ADP), freeing phosphate (Pi) and using the released energy for generating motion. A prototypical biochemical model of the myosin ATPase reaction in solution, linking together the attachment-detachment, the power-stroke and the hydrolysis of ATP, is known as the Lymn–Taylor cycle [72], see Fig. 4.1. While this minimal description of enzyme kinetics is common for most myosins motors [113], its association with microscopic structural details and its relation to micro-mechanical interactions remains a subject of debate [22, 111, 112].

In physiological literature it is usually implied that muscle contraction is to a large degree driven by the power-stroke which is then perceived as an active mechanism [42]. This opinion is supported by observations that both the power-stroke and the reverse-power-stroke can be induced by ATP even in the absence of actin filaments [112], that contractions can be significantly inhibited by antibodies which impair lever arm activity [84], that sliding velocity in mutational myosin forms depends on the lever arm length [117] and that the directionality can be reversed as a result of modifications in the lever arm domain [15, 116].

A perspective that the power-stroke is the driving force of active contraction was challenged by the suggestion that myosin catalytic domain could operate as a Brownian ratchet, which means that it can move and produce contraction without

assistance from the power-stroke mechanism [49, 95, 130]. In this interpretation the contraction is driven directly by the attachment-detachment machinery which rectifies correlated noise and selects directionality following, for instance, the polarity of actin filaments [57, 58].

Although the simplest models of Brownian ratchets neglect the conformational change, some phases of the attachment-detachment cycle can be interpreted as the power-stroke when the actin potential is assumed to undergoe additional externally driven horizontal shifts [122, 126]. Ratchet models were also proposed where the periodic spatial landscape is supplemented by a reaction coordinate, representing the conformational change [93, 127]. In all these models, however, the role of the power stroke was viewed as secondary and the contraction could be generated even if the power stroke mechanism was disabled. The main functionality of the power-stroke mechanism would be then attributed to passive fast force recovery [2, 19, 54].

An alternative viewpoint that the power-stroke mechanism consumes chemical energy and can be viewed as active, is the underpinning of the broadly accepted phenomenological chemo-mechanical models [52, 88]. These models pay great attention to structural details and in their most comprehensive versions faithfully reproduce the main experimental observations [83, 109]. The chemo-mechanical models, however, are not transparent mechanistically because they deal with elastic interactions implicitly. In these models chemical states are interpreted as continuous manifolds (parameterized by the strain) and to characterize jump processes between the points on these manifolds the authors choose the transition rate functions phenomenologically. While this functional freedom compensates the lack of knowledge of the underlying multidimensional energy landscape, the inherent arbitrariness of some of these choices limits the ultimate predictive power of this approach.

In an attempt to reach a synthetic description, several hybrid models, allowing chemical states to coexist with springs and forces, have been also proposed [26, 46, 65]. The phenomenological side of these models is minimal, however, they still combine continuous dynamics with jump transitions which makes the precise identification of structural prototypes and the underlying micro-mechanical interactions challenging. In this class of models the power-stroke in an individual cross-bridge was reproduced most faithfully by Geislinger and Kawai who introduced a 2D energy landscape by coupling a bi-stable potential with a symmetric periodic potential [43]. In this model both the attachment-detachment mechanism and the power stroke mechanism were effectively endowed with activity, however, the ATP hydrolysis was still represented by a flashing actin potential.

In these lecture notes we review a set of models which suggest that the power stroke can be, at least in principle, the main driving force behind muscle contraction. The discussed models are fully mechanistic in the sense that all ambiguous jump processes are replaced by a fully mechanistic Langevin dynamics. To focus exclusively on the idea of an active power stroke, driven directly by the ATP hydrolysis, we intentionally simplify the real picture and at some point even model actin filaments as passive non-polar tracks. The power-stroke mechanism is represented by a symmetric bi-stable potential associated with an internal degree of freedom and the ATP activity is modeled by a correlated component of the external

noise. We show that even in this simple setting one can obtain a fully mechanical interpretation of all four chemical states in the minimal Lymn–Taylor cycle which opens a possibility of building artificial engineering devices mimicking enzymatic activity.

We start with a discussion of the three main force generation mechanisms: motor driven contraction, power stroke driven contraction and the model where power stroke not only drives the process but also controls the attachment/detachment mechanism. The idea that the symmetry breaking mechanism rests in internal conformational transition [23, 75] is borrowed from the theory of processive motors [24, 82, 104, 124]. Thus, in the description of dimeric motors it is usually assumed that ATP hydrolysis induces a conformational transformation which then changes the relative position of the motor legs ensuring motility [119]. Here we use the same idea to describe a non-processive motor with a single leg that remains on track due to the presence of a thick filament.

To be realistic, a model of the power stroke driven contraction must contain an assumption that the strength of the attachment depends on the state of the power stroke element. To justify the implied coupling, we argue that the conformational state of the power-stroke element provides steric regulation of the distance between the myosin head and the actin filament. More specifically, we assume that when the lever arm swings, the interaction of the head with the binding site weakens. This and other aspects of steric rotation-translation coupling in ratchet models are discussed in [43, 68, 90].

The proposed framework allows for three different modes of power stroke driven contractility which may operate simultaneously.

The first mode is activated only if correlations are present in the additive noise as in the conventional rocking ratchets [74]. The peculiarity of our rocking ratchet is that the periodic potential is symmetric and time independent. The correlated component of the noise affects the bi-stable potential and, since it is also symmetric, the directional motion is due exclusively to an asymmetry induced by the coupling between the internal degrees of freedom and the center of mass of the motor.

The second mode does not necessitate correlations in the noise but instead requires that the coupling between the power-stroke element and the actin filament is hysteretic. The motor can then extract energy directly from the delay mechanism which represents a non-equilibrium reservoir. We show that the two active mechanisms, correlations-induced and hysteresis-induced, can favor motions in different directions and can play complimentary roles.

Finally, the third mode functions if the internal forces acting between the myosin head and the actin filament are non-potential even without being hysteretic [73, 93, 130]. This assumption introduces another active mechanism which can drive the motor even if the environment is in equilibrium. The correlations-induced and non-potentiality-induced mechanisms can impose opposite directionality, in particular, they can operate in combination to slow down and even to stop the motor.

The variety of the available regimes is particularly rich when the forces are non-potential and the coupling between the power-stroke and the actin filament is hysteretic. The resulting ratchet shows complex reversals of current depending

on the amplitude of the external driving and temperature. The importance of the hysteretic coupling is revealed by the observation that only in this case the model can reproduce all four steps of the Lymn–Taylor cycle.

In the last section of these lecture notes we show that the power-stroke-driven active rigidity can emerge as a result of resonant nonthermal excitation of the power stroke machinery. Building upon the idea of active drift [96] we consider a family of stall states in a power stroke driven system parameterized by a meso-scopic measure of total deformation. We compute the time and ensemble averaged potential at the fixed value of the deformation parameter and interpret the deformation derivative of this potential as an effective stiffness.

Of particular interest is the effect on active rigidity of the stochastic nature of the nonequilibrium reservoir. We show that while in periodic or dichotomous environments, the noise induced pseudo well exists, active stabilization disappears if the noise is of Ornshtein–Uhlenbeck type. The sensitive dependence of the mechanical performance of the molecular scale devices on the shape of the power spectrum of the noise, has been previously observed in the studies of active drift [25, 81] and here we broaden the picture by covering molecular machines generating active rigidity. Various features captured by our minimal model of active rigidity are in common not only with inertial stabilization [17], but also with the performance of the Ising model in periodic magnetic field [40], the folding/unfolding of proteins subjected to periodic forces [38] and the parametric behavior of more complex actively driven systems [11, 20, 85].

While some of the material collected in these lecture notes is new, the main ideas are based on the published papers [107, 108].

4.2 General Ratchet Model

Even the simplest mechanical model of a cross-bridge capable of both, the attachment detachment and the power stroke, must involve at least two continuous variables [52, 73, 74].

Suppose that the position of the motor head is modeled by the variable $x(t)$, while the variable $y(t)$ describes the internal degree of freedom representing the configuration of the lever-arm, see Fig 4.2a. Suppose also that the interaction between the myosin head and the actin filament is modeled by a space periodic potential. Finally, assume that the molecular link between the motor head and the motor tail can be described by a bi-stable spring, see Fig 4.2b.

Using these assumptions we can now formulate the general stochastic dynamics of a cross-bride in terms of the system of Langevin equations:

$$\boldsymbol{\eta} d\mathbf{X}/dt = -\nabla G(\mathbf{X}, t) + \boldsymbol{\sigma}\boldsymbol{\xi}(t). \tag{4.1}$$

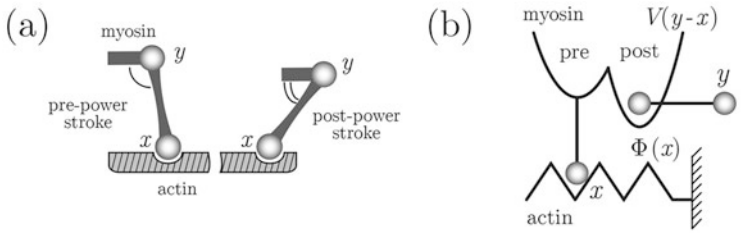

Fig. 4.2 (**a**) Sketch of one-legged molecular motor in pre-power stroke and post-power stroke configurations. (**b**) The mechanical model

Here $\boldsymbol{\eta}$ is a diagonal matrix defining drift coefficients, $\boldsymbol{\sigma}$ is another diagonal matrix with components $\sqrt{2\eta_i k_B \Theta}$, and $\boldsymbol{\xi}(t)$ is the Gaussian random vector with zero mean $\langle \xi_i(t) \rangle = 0$, and with correlations $\langle \xi_i(t)\xi_j(s) \rangle = \delta_{ij}\delta(t-s)$, $i, j = x, y$. The terms $\eta_i dx_i/dt$ describe frictional forces and the corresponding drag coefficients are assumed to be constant. The function $G(\mathbf{X}, t)$ introduces the energy landscape of the motor device.

The mechanical action of the ATP hydrolysis will be represented by a correlated component of the external noise $\mathbf{f}$. Suppose that such a noise can affect both, the actin/myosin bound states and the conformational state of the lever-arm. This means that the corresponding force can act on coordinates x and y. Writing a generic expression for a tilted energy landscape $G(\mathbf{X}, t)$ we obtain

$$G(\mathbf{X}, t) = G_0(x, y) - x f_x(t) - y f_y(t). \tag{4.2}$$

Here $G_0(x, y) = \Phi(x) + V(y - x)$ is the intrinsic energy landscape, see Fig. 4.4a, where the bi-stable potential $V(y - x)$ describes two conformational states of the power stroke mechanism. We identify one energy well with the pre-power-stroke state and another energy well with the post-power-stroke state. We also assume that the potential $\Phi(x)$ has period L so what $\Phi(x + L) = \Phi(x)$. The simplest representation of the correlated noise $f_i(t)$ imitating the ATP activity is through periodic functions with zero average (over the corresponding periods τ_i).

Since our goal is to develop the model with active power stroke we will not consider the most general case, when the components $f_y(t)$ and $f_x(t)$ are independent. Instead, we focus on three specific models. In 'X model' the rocking/tilting force acts on the variable x,

$$f_x(t) = f(t), \;\; f_y(t) = 0; \tag{4.3a}$$

this model was already introduced and studied in [76]. In 'Y model' the rocking force will be acting on the variable y

$$f_x(t) = 0, \;\; f_y(t) = f(t). \tag{4.3b}$$

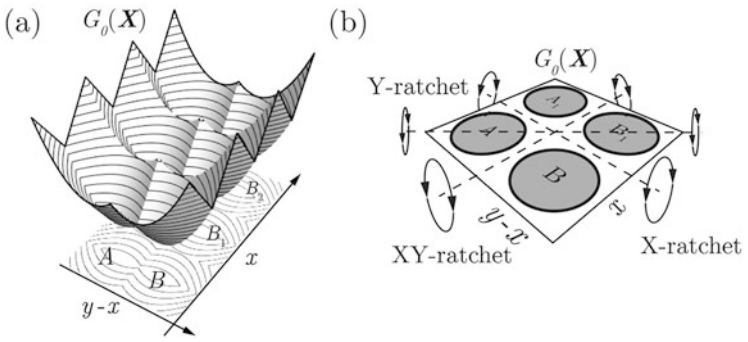

Fig. 4.3 (**a**) The surface and contour plot of the function $G_0(x, y)$. (**b**) The scheme illustrating three different rocking mechanism: X-ratchet (4.3a), Y-ratchet (4.3b), XY-ratchet (4.3c)

Finally, in 'XY model' the rocking couple will act on the difference $y - x$,

$$f_x(t) = -f(t), \;\; f_y(t) = f(t). \tag{4.3c}$$

In Fig. 4.3a we illustrate our two-dimensional energy landscape identifying four different mechanical configurations A, B, A_1, B_1 which represent different local minima of the energy. The schematic illustration of the three different rocking mechanisms is shown in Fig. 4.3b.

In the X-tilted ratchet model (4.3a) the correlated force is applied to the x variable while the power-stroke mechanism remains passive. Applying the correlated force to the y variable in the Y-tilted ratchet model (4.3b) we make the first step in the direction of bringing activity to the power stroke mechanism. Finally, in the XY-tilted ratchet model (4.3c), the active force is applied directly to the $y - x$ variable. The non-equilibrium noise in this model is then acting directly on the internal degree of freedom characterizing the motor mechanism.

A model closely related to XY-tilted ratchet and coupling translational and rotational degrees of freedom was considered in [43]. The XY-tilted ratchet also resembles some models of Kinesin where ATP acts on the internal bi-stable device forcing two legs to move along the actin filament. In this sense the XY-tilted cross-bridge can be viewed as a "single-leg" analog of a Kinesin motor [78] with both mechanisms driven through the power stroke.

In these lecture notes we consider two loading devices–hard and soft, see Fig. 4.4. In the case of hard (or, rather, mixed) device the total energy is

$$G_0^h(x, y) = \Phi(x) + V(y - x) + \frac{1}{2}k_m(y - z)^2, \tag{4.4}$$

where $V_m = \frac{1}{2}k_m(y - z)^2$ is the potential of a linear spring and the variable z is treated as a fixed external parameter, see Fig. 4.4a. In this case, it is of interest to compute the average tension generated by such system $T = k_m(\overline{\langle y \rangle} - z)$, where the

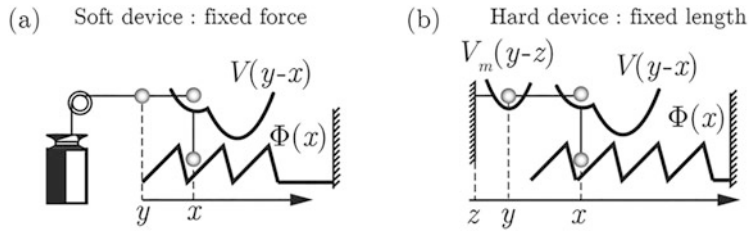

Fig. 4.4 (**a**) Soft device configuration; (**b**) hard device configuration

notation $\overline{\langle y \rangle}$ indicates the averaging of the stochastic variable $y(t)$ over the ensemble and over the time. In the case of soft device the total energy is

$$G_0^s(x, y) = \Phi(x) + V(y - x) - y f_{ext}, \tag{4.5}$$

where f_{ext} is an external force, see Fig. 4.4b. In this case, the parameter of interest is the drift velocity $v = \lim_{t\to\infty}\langle x(t)\rangle/t$.

4.3 X-Tilted Ratchet

We recall that in this case the correlated noise $f(t)$ is acting on the x variable. In Fig. 4.5 we present a schematic illustration of the rocking axis for the corresponding energy landscape in coordinates $(y - x, x)$. The implied tilting biases the states A', B' during the first half of the period and the states A, B during the second half of the period.

It will be convenient to rewrite our equations in the dimensionless form. We use the following definitions of the non-dimensional variables: $\tilde{X}\left(\tilde{t}\right) \equiv (1/a)X\left(t = \tau^\star\tilde{t}\right)$, $\tilde{V}\left(\tilde{x}, \tilde{y}\right) \equiv (1/(k_m a^2))V\left(x = a\tilde{x}, y = a\tilde{y}\right)$, $\tilde{f}(\tilde{t}) \equiv (1/(k_m a))f(t)$ and $\tilde{\xi}_i(\tilde{t}) \equiv \xi_i(t)/\sqrt{\tau^\star}$ Here $\tau^\star$ is the main time scale of the problem $\tau^\star = \eta_y/k_m$. The distance a between two minima of the potential $V(y-x)$ introduces the characteristic length scale, while the natural energy scale is $k_m a^2$. The remaining nondimensional parameters are $\tilde{D} \equiv k_B\Theta/(k_m a^2)$ and $\alpha = \eta_y/\eta_x$. Below, for simplicity, we omit the tildas.

In the soft device the dimensionless system takes the form:

$$\begin{cases} dx/dt = -\alpha\left[\partial_x\Phi(x) + \partial_x V(y-x) - f(t)\right] + \sqrt{2\alpha D}\ \xi_x(t), \\ dy/dt = -\partial_y V(y-x) + f_{\text{ext}} + \sqrt{2D}\ \xi_y(t), \end{cases} \tag{4.6}$$

while in the hard device we obtain

$$\begin{cases} dx/dt = -\alpha\left[\partial_x\Phi(x) + \partial_x V(y-x) - f(t)\right] + \sqrt{2\alpha D}\ \xi_x(t), \\ dy/dt = -\partial_y V(y-x) - k_m(y-z) + \sqrt{2D}\ \xi_y(t). \end{cases} \tag{4.7}$$

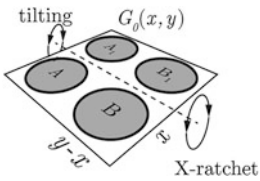

Fig. 4.5 X-tilted ratchet model: the energy landscape with a fictive axis showing how the rocking is applied

The Fokker–Planck equations corresponding to the normalized systems of Langevin equations (4.6) and (4.7) take the form:

- in the soft device configuration:

$$\partial_t P^s(x,y,t) = \alpha D \partial_x \left[\frac{P^s(x,y,t)}{D} \partial_x G^s(x,y,t) + \partial_x P^s(x,y,t) \right] + D \partial_y \left[\frac{P^s(x,y,t)}{D} \partial_y G^s(x,y,t) + \partial_y P^s(x,y,t) \right], \tag{4.8}$$

  where $G^s(x,y,t) = \Phi(x) + V(y-x) - xf(t) - yf_{ext}$.
- in the hard device configuration:

$$\partial_t P^h(x,y,t) = \alpha D \partial_x \left[\frac{P^h(x,y,t)}{D} \partial_x G^h(x,y,t) + \partial_x P^h(x,y,t) \right] + D \partial_y \left[\frac{P^h(x,y,t)}{D} \partial_y G^h(x,y,t) + \partial_y P^h(x,y,t) \right], \tag{4.9}$$

  where $G^h(x,y,t) = \Phi(x) + V(y-x) - xf(t) + \frac{1}{2}k_m(y-z)^2$.

In what follows, we adopt the simplest descriptions of the functions $\Phi(x)$, $V(y-x)$ and $f(t)$. Thus, we assume that

$$\Phi(x) = \begin{cases} \dfrac{\Phi_{max}}{\lambda_1}(x - nL), & \text{for } nL \le x < nL + \lambda_1 \\ \dfrac{\Phi_{max}}{\lambda_2}((n+1)L - x), & \text{for } nL + \lambda_1 \le x < (n+1)L,\ n \in \mathbb{N} \end{cases} \tag{4.10}$$

where $\Delta = \lambda_1 - \lambda_2$ is the parameter, which controls the potential asymmetry, when $\lambda_1 = (L + \Delta)/2$ and $\lambda_2 = (L - \Delta)/2$. The bi-stable element will be described by a piece-wise quadratic function

$$V(y-x) = \begin{cases} \frac{1}{2}k_0 (y-x)^2 + \varepsilon_0, & (y-x) \leqslant l, \\ \frac{1}{2}k_1 (y-x-a)^2, & (y-x) \geqslant l, \end{cases} \tag{4.11}$$

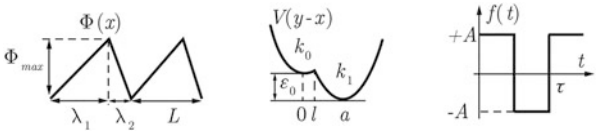

Fig. 4.6 The adopted simplified structure of the functions $\Phi(x)$,$V(y-x)$ and $f(t)$

where $\varepsilon_0 = 1/2\left(k_1(l-a)^2 - k_0 l^2\right)$. A periodic force $f(t)$ with period τ is assumed to be a square signal

$$f(t) = A(-1)^{n(t)} \quad \text{with} \quad n(t) = \lfloor 2t/\tau \rfloor, \tag{4.12}$$

where brackets $\lfloor\rfloor$ denote integer part. We illustrate the functions $\Phi(x)$, $V(y-x)$ and $f(t)$ in Fig. 4.6.

4.3.1 Typical Cycles

Soft Device We begin with a series of numerical experiments in the soft device. We perform computations by using the standard Euler scheme with the time step $\Delta t = 10^{-3}$ and then conduct the averaging over $N_r = 10^3$ realizations of the noise.

In Fig. 4.7a we illustrate the typical average trajectory of the X-tilted motor when the system reaches the steady state with the average velocity $v_x = v_y \equiv v$. Our Fig. 4.7b shows the time evolution of the system in coordinates $(t, y-x)$. Observe the emerging oscillations between the two wells of the bi-stable potential and note that the motor crosses a succession of space periods, see Fig. 4.7c.

We define the cycle as a segment of the average trajectory corresponding to one period of the driving $f(t)$. During the cycle we associate the transition $A'' \to B'$ with the release of the power stroke mechanism and the transition $B \to A''$ with its recharging.

In order to make sure that during each cycle the motor performs only one attachment-detachment step, we need to adjust our parameters. Suppose that $\alpha = 0.2$ (which controls the drift along x coordinate), take $L = 3$, and, in order to preserve the value of the force acting on the particle, choose $\Phi_{max} = 4.5$. In Fig. 4.8 we show the ensuing average behavior of the motor. As in the case shown in Fig. 4.7, the system reaches the steady state with a particular value of the average velocity, see Fig. 4.7a. The visible fluctuations can be explained by the relatively small number of stochastic realization in this case where we took $N_r = 200$.

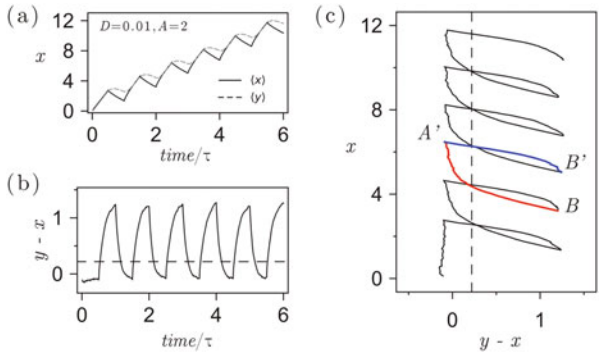

Fig. 4.7 The behavior of the X-tilted ratchet model in soft device with $f_{ext} = 0$. (**a**) The trajectories $\langle x(t)\rangle$ (solid black line) and $\langle y(t)\rangle$ (dashed gray line); (**b**) the time evolution of the system in coordinates $\{t, y - x\}$; (**c**) the average trajectory in coordinates $\{y - x, x\}$. Parameters: $k_0 = 1.5$, $k_1 = 0.43$, $l = 0.22$, $a = 1$, $\lambda_1 = 0.35$, $L = 0.5$, $\Phi_{max} = 0.75$, $\alpha = 1$, $A = 2$, $\tau = 16$

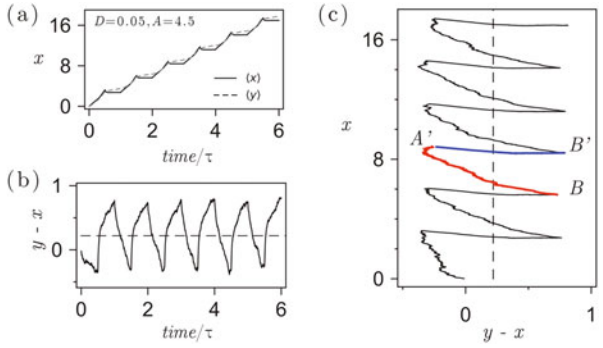

Fig. 4.8 The X-tilted ratchet in the soft device configuration with $f_{ext} = 0$. (**a**) The trajectories $\langle x(t)\rangle$ (solid black line) and $\langle y(t)\rangle$ (dashed gray line); (**b**) the time evolution of the system in coordinates $\{t, y-x\}$; (**c**) the average trajectory in coordinates $\{y-x, x\}$. The red line corresponds to $f(t) = +A$, blue line—to $f(t) = -A$. Parameters: $k_0 = 1.5$, $k_1 = 0.43$, $l = 0.22$, $a = 1$, $\lambda_1 = 2.4$, $L = 3$, $\alpha = 0.2$, $A = 4.5$, $\tau = 16$

The ensuing X motor cycle can be presented as a combination of two steps (see Fig. 4.9a):

- $1 \rightarrow 2$. First, because of the broken space symmetry, the motor advances in the x direction and crosses the energy barriers associated with the maxima of the periodic potential $\Phi(x)$. In the meanwhile the motor recharges the power stroke mechanism.

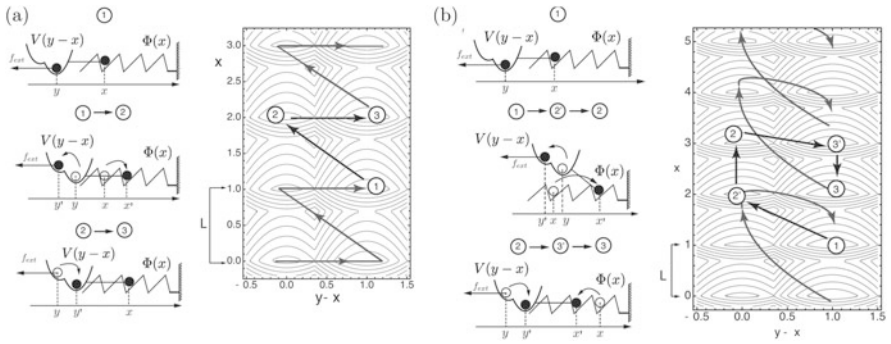

Fig. 4.9 The X-tilted ratchet model in the soft device configuration. With the solid gray lines we show the surface contours of the energy landscape $\Phi(x) + V(y-x)$. (**a**) The simplest motor cycle. (**b**) More complex motor cycle

- 2→3. As the rocking force changes its sign, the new configuration of the energy landscape drives the motor into the backward direction along the x axis. However, the motor is now trapped and instead of going backwards, it performs the power-stroke. Then the motor cycle starts again.

Note that in both studied cases the detachment and re-attachment take place simultaneously with the power stroke. Since the power stroke in this model is passive, the advance of the motor is due exclusively to the asymmetry of the potential $V(y-x)$: the motor must advance along the x axis in order to ensure the recharging of the power stroke mechanism. Note also that the ratchet must make a sufficiently large step in the forward direction in order to recharge the power stroke mechanism.

By varying the parameters of the model we can obtain other cycles as well. For instance, the motor step $1 \to 2$ can be made longer than a simple jump between the two nearest periods. Also, we can force the motor to move according to the scheme $1 \to 2' \to 2$, shown in Fig. 4.9b. Moreover, the motor can advance few periods along the x axis in the forward direction before accomplishing the power-stroke $2 \to 3$ and can also move backward during a few periods following the path $2 \to 3' \to 3$. Note, however that while both motor positions, $3'$ and 3, correspond to the same energy well 0 in the bi-stable potential, they are associated with different wells of the periodic potential.

Hard Device To study the effect of temperature we vary the parameter D while keeping the amplitude of the nonequilibrium driving fixed at $A = 6$ and in Fig. 4.10 we show the average trajectories during one time period of the force $f(t)$. With solid lines we show the energy landscape in the positive phase and with dashed black lines in the negative phase of rocking. We illustrate the average trajectory using different colors depending on the phase of rocking.

We observe that the cycle get stabilized after a short transient period. At low temperatures the response is localized around one minimum of the bi-stable

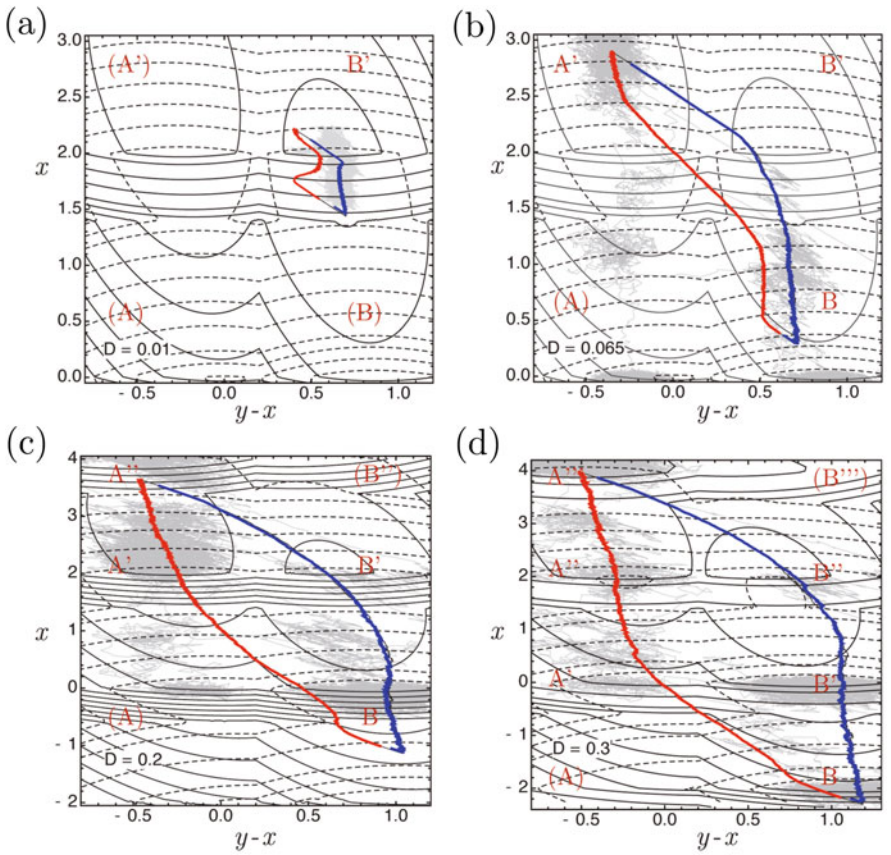

Fig. 4.10 The X-tilted ratchet model in the hard device configuration at different values of the temperature D and constant amplitude $A = 6$. The light gray lines depict a single stochastic realization during one time period. (**a**) $D = 0.01$; (**b**) $D = 0.065$; (**c**) $D = 0.08$; (**d**) $D = 0.3$. The other parameters are: $k_0 = k_1 = 7,\ l = 0.22,\ a = 1,\ L = 2, \lambda_1 = 1.4,\ \Phi_{max} = 5,\ \alpha = 5$ and $\tau = 20$

potential, see Fig. 4.10a. The increase of temperature allows the configurational particle to cross the potential barriers along both $y - x$ and x directions, in particular it allows for a transition between the energy wells of the bi-stable potential, see Fig. 4.10b, c. An (almost) three-state cycle is formed if the motor can displace itself along x sufficiently far in order to be able to recharge the power stroke element. If we increase the parameter D further, the particle makes larger jumps along the x direction, see Fog. 4.10d. At even higher temperatures the system loses its ability to generate force.

In Fig. 4.11 we present a schematic illustration of the attainable three-state cycle in the hard device. After a transient stage the motor follows the following trajectory in the clockwise direction $1 \to 2 \to 3 \to 1$ where:

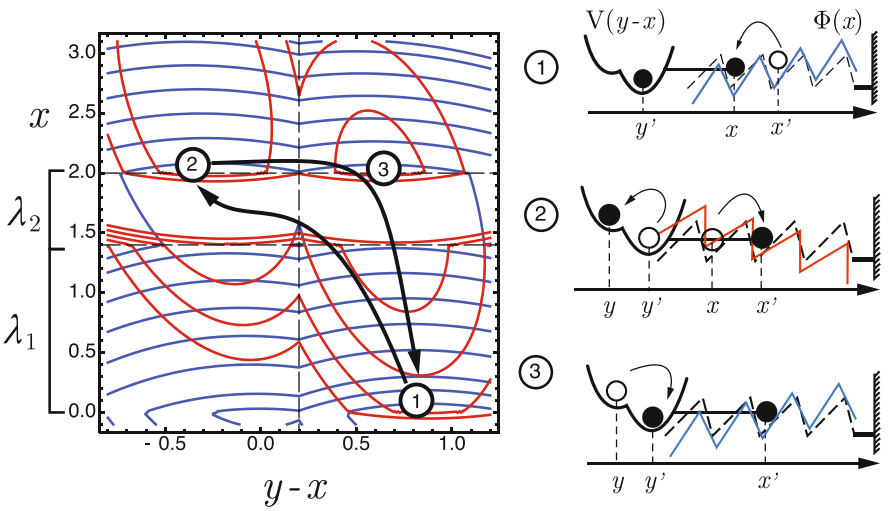

Fig. 4.11 The schematic representation of the typical X-tilted ratchet cycle in the hard device loading configuration. The average trajectory is shown by solid black arrows

- Transition $1 \rightarrow 2$. The average trajectory is shown schematically by black arrows. During the positive phase of the driving $f(t)$, motor crosses the barrier in the forward direction along the saw-tooth actin potential. It recharges the power stroke element, see Fig. 4.10 (phase plotted in red).
- During the negative phase of the driving $f(t)$ the motor makes the transition $2 \rightarrow 3 \rightarrow 1$, see Fig. 4.10 (phase plotted in blue). The change of sign of the force $f(t)$ biases the transition in the backward direction along the potential $\Phi(x)$. At the same time, the transition $2 \rightarrow 3$ takes place which we can identify with the power stroke. After the transition $3 \rightarrow 1$ the motor cycle starts again.

The main characteristic feature of the X model is that the power stroke is recharged purely mechanically, together with the advance of the motor along the actin filament. This unavoidably combines two different steps of the Lymn–Taylor cycle into one.

4.3.2 *Force-Velocity Relations and Stochastic Energetics*

Next we study the force-velocity relation for the X-tilted ratchet placed in the soft device. In Fig. 4.12 we present our numerical results for different temperatures D and two amplitudes of the non-equilibrium driving: $A = 2.5$ and $A = 4.5$. At $A = 2.5$ and small temperature we observe the characteristic concave shape of the force velocity curve. The area limited by the curve and the axes increases with temperature until the maximum is reached at $D = 0.1$. The subsequent increase

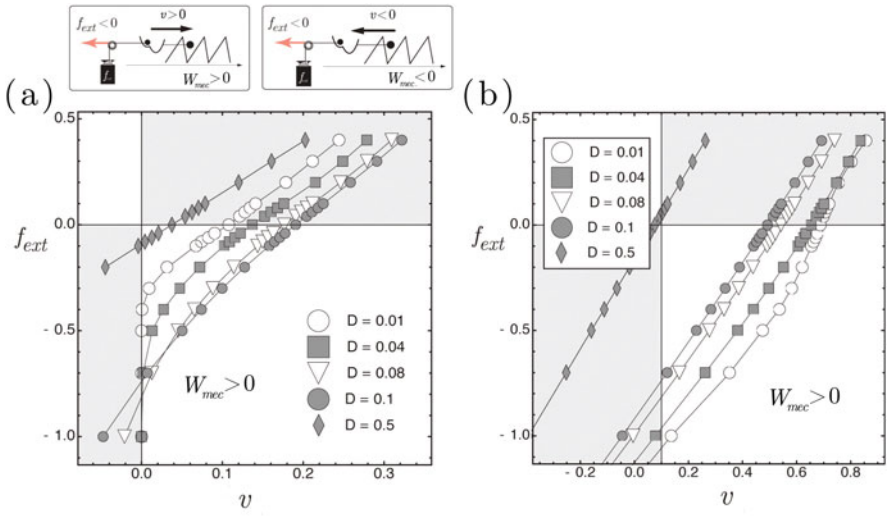

Fig. 4.12 Force-velocity relations for the X-tilted ratchet: (**a**) $A = 2.5$; (**b**) $A = 4.5$. The parameters: $k_0 = 1.5$, $k_1 = 0.43$, $l = 0.22$, $a = 1$, $L = 1$, $\lambda_1 = 0.7$, $\Phi_{max} = 1.5$, $\alpha = 1$, $\alpha = 1$ and $\tau = 20$

of temperature leads to the loss of the performance of the motor. The stall force, defined in soft device as the value of force at zero average velocity, increases with increasing temperature until the threshold value of D and decrease afterwards. At $A = 4.5$ we observe that the force velocity curves become convex. With the increase of temperature D we first approach the linear regime but then start to lose the active performance.

We define the active work performed by the motor against the load as $-f_{ext}v$ which means that it is positive when the average velocity and the external force have opposite signs. In these regimes the system is anti-dissipative, the motor uses (instead of dissipating) the external energy and can therefore perform some useful work, see the gray quadrants in 4.12. The predominantly passive regimes correspond to the cases where the average velocity and the external load have the same sign. Such systems are mostly dissipative and the energy is released rather than being absorbed, see the white quadrants in Fig. 4.12.

In Fig. 4.13a we present the average velocity of the motor as a function of temperature D for several values of the rocking amplitude A. At small amplitudes the motor shows a maximum of the velocity at a finite temperature. At high amplitudes the average velocity is a monotonically decreasing function of D which suggests that we deal with a purely mechanical ratchet. By light green color we identify the region with negative velocity where the motor is dragged by the cargo.

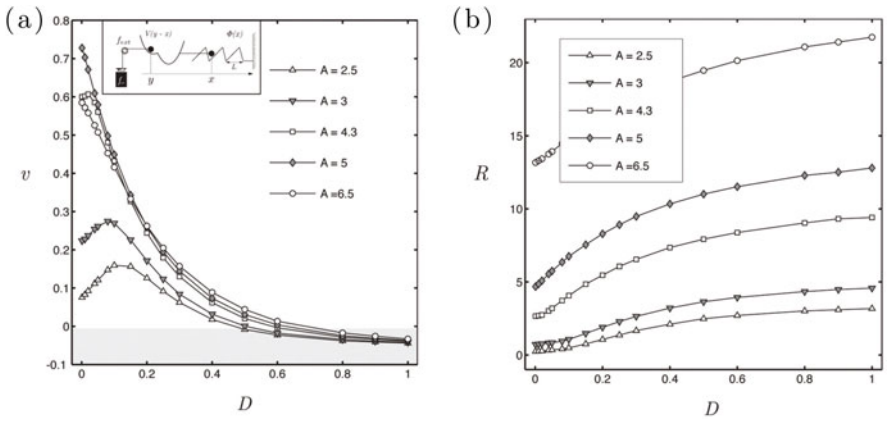

Fig. 4.13 X-tilted ratchet in the soft device configuration, $f_{ext} = -0.1$. (**a**) The dependence of the average velocity v on temperature D for the different values of the amplitude A. (**b**) The consumed energy R. The parameters: $k_0 = 1.5,\ k_1 = 0.43,\ l = 0.22,\ a = 1,\ L = 1,\ \lambda_1 = 0.7,\ \Phi_{max} = 1.5,\ \alpha = 1$ and $\tau = 30$

To study the energetics of the X-tilted ratchet we rewrite the equations of the model in the soft device (4.6) in the form

$$\begin{cases} \partial_x[\Phi(x) + V(y-x)] - f(t) = -\dfrac{1}{\alpha} d_t x + \sqrt{\dfrac{2D}{\alpha}}\ \xi_x(t), \\ \partial_y V(y-x) - f_{ext} = -d_t y + \sqrt{2D}\ \xi_y(t). \end{cases} \tag{4.13}$$

If we now multiply these equations by the vector $d\mathbf{X}$ in the Stratonovich sense and use the conventional definition of the exchanged heat $\delta Q_i = \left(-\eta d_t x_i + \sqrt{2\eta_i D}\xi_i(t)\right) \circ dx_i$ [105] we obtain

$$\begin{cases} \partial_x\left[\Phi(x) + V(y-x)\right] \circ dx - f(t) \circ dx = \delta Q_x, \\ \partial_y V(y-x) \circ dy - f_{\text{ext}} \circ dy = \delta Q_y. \end{cases} \tag{4.14}$$

Using the definition $G_0(x_t, y_t) = \Phi(x_t) + V(y_t - x_t) - y f_{ext}$ we can rewrite these equations in the form

$$\begin{cases} \partial_x G_0 \circ dx - f(t) \circ dx = \delta Q_x, \\ \partial_y G_0 \circ dy = \delta Q_y. \end{cases} \tag{4.15}$$

If we now average these equations over one time period τ, we obtain

$$\frac{1}{\tau} \int_{\mathbf{X}_t}^{\mathbf{X}_{t+\tau}} dG_0(\mathbf{X}_t) - \frac{1}{\tau} \int_{x_t}^{x_{t+\tau}} f(t) dx_t = \frac{1}{\tau} \int_{\mathbf{X}_t}^{\mathbf{X}_{t+\tau}} (\delta Q_x + \delta Q_y). \tag{4.16}$$

Here we can identify the input energy $R = \frac{1}{\tau}\int_{x_t}^{x_{t+\tau}} f(t)dx_t$. Our Fig. 4.13b shows the value of R for the system in a soft device as a function of D for several values of A. One can see that with the increase of the level of thermal fluctuations the motor needs more energy in order to preform the work. At large temperatures we observe saturation, showing that the motor dragged by the cargo consumes energy at a fixed rate.

If we now define the (active or passive) mechanical work

$$W_{mec} = \frac{1}{\tau}\int_{\mathbf{X}_t}^{\mathbf{X}_{t+\tau}} dG_0(\mathbf{X}_t) = -\frac{1}{\tau}\int_{y_t}^{y_{t+\tau}} f_{ext}dy = -f_{ext}v_y \equiv -f_{ext}v, \tag{4.17}$$

we can then write the energy balance in the form $W_{mec} = R + Q$ where the heat term is $Q = \frac{1}{\tau}\int_{\mathbf{X}_t}^{\mathbf{X}_{t+\tau}} (\delta Q_x + \delta Q_y)$ [105]. For the system in the soft device, the mechanical efficiency of the system can be defined by the expression

$$\epsilon_{mec} = \frac{W_{\text{mec}}}{R}. \tag{4.18}$$

If we associate the functional work of an unloaded motor with overcoming viscous drag $W_{\text{Stokes}} = \alpha^{-1}v_x^2 + v_y^2$. we can also define the Stokes efficiency

$$\epsilon_{Stokes} = \frac{W_{Stokes}}{R}. \tag{4.19}$$

Finally, we can define the rectifying efficiency by combining Stokes and mechanical efficiencies:

$$\epsilon_{rec} = \frac{W_{mec} + W_{Stokes}}{R}. \tag{4.20}$$

In Fig. 4.14a we illustrate for the system in the soft device the mechanical work as a function of D at increasing values of A. By color, we mark the region of positive and negative mechanical work. In Fig. 4.14b we show the temperature dependence of the mechanical efficiency. In the regime of small amplitude A we observe a maximum of efficiency at finite temperature. With increasing amplitude A, the maximum vanishes and the efficiency becomes a monotonically decreasing function of D, which is the behavior characteristic for mechanical ratchets. By light green we indicate the regime of negative efficiency, where our motor is unable to perform a positive mechanic work against the external force and performs instead as an active breaking mechanism. In Fig. 4.14c we plot the Stokes efficiency as a function of D; the rectifying efficiency is shown in Fig. 4.14d. The shape of these functions is dominated by the quadratic Stokes term, however, the cumulative efficiency can

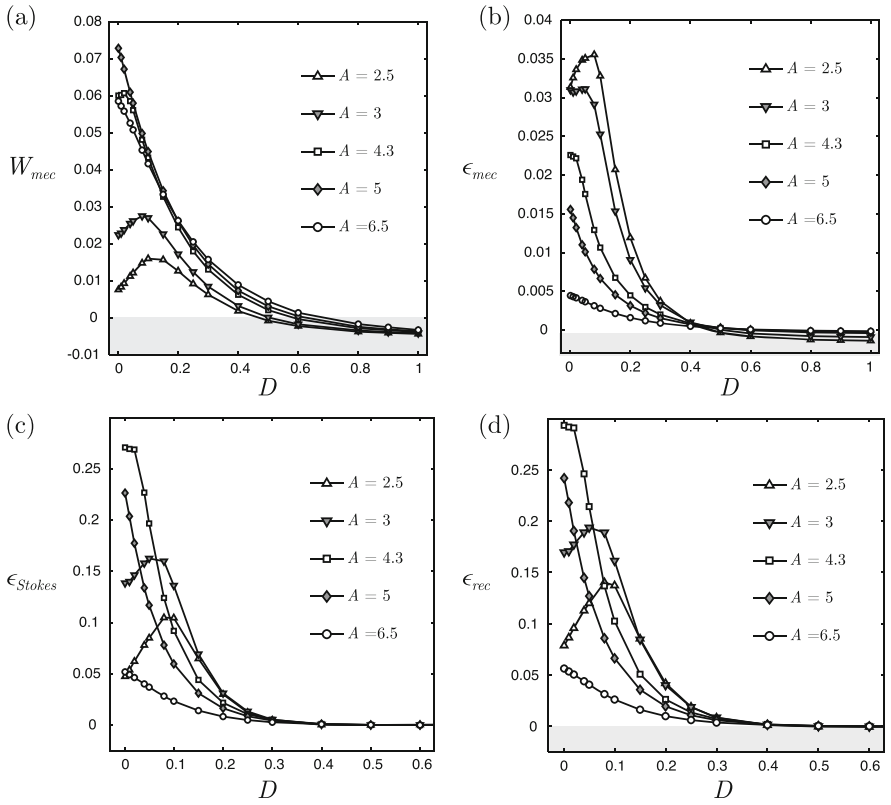

Fig. 4.14 X-tilted ratchet in the soft device configuration with $f_{ext} = -0.1$. (**a**) The dependence of the mechanical work W_{mec} on temperature D for different amplitudes A; (**b**) the mechanical efficiency ϵ_{mec}; (**c**) the stokes efficiency; (**d**) the rectifying efficiency. Parameters are the same as in Fig. 4.13

have a maximum at a finite temperature also if the amplitude of the rocking is small and the device works as a Brownian ratchet.

4.4 Y-Tilted Ratchet

The Y-tilted ratchet coupes the bi-stable potential $V(y - x)$ with the space periodic potential $\Phi(x)$. On the scheme presented in Fig. 4.15 we show again one period of the two-dimensional energy landscape with four mechanical configurations A, B, A', B' representing local minima of the energy. The applied periodic tilting acts along the diagonal and biases either the state B', during the positive phase of rocking, or the state A, during the negative phase.

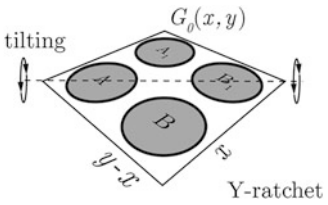

Fig. 4.15 Y-tilted ratchet energy landscape

The dimensionless system of Langevin equation for the Y-tilted motor in the soft device takes the form

$$\begin{cases} dx/dt = -\alpha\,[\partial_x \Phi(x) + \partial_x V(y-x)] + \sqrt{2\alpha D}\;\xi_x(t), \\ dy/dt = -\partial_y V(y-x) + f_{\text{ext}} + f(t) + \sqrt{2D}\;\xi_y(t). \end{cases} \tag{4.21}$$

In the hard device we obtain

$$\begin{cases} dx/dt = -\alpha\,[\partial_x \Phi(x) + \partial_x V(y-x)] + \sqrt{2\alpha D}\;\xi_x(t), \\ dy/dt = -\partial_y V(y-x) - k_m(y-z) + f(t) + \sqrt{2D}\;\xi_y(t). \end{cases} \tag{4.22}$$

Here we use the same potentials as before: $\Phi(x)$, see (4.10), $V(y-x)$, see (4.11) and $f(t)$, see (4.12). They are all schematically illustrated in Fig. 4.6.

4.4.1 Typical Cycles

Soft Device In Fig. 4.16 we show the two-dimensional representation of the motor trajectory in the case of zero external load, $f_{ext} = 0$. The main new observation is that the Y-tilted ratchet is able to generate a four-state cycle $A \to B \to B' \to A'$. This cycle is realistic and can be in principle directly compared with the biochemical Lymn–Taylor cycle.

The schematic representation of such cycle is shown in Fig. 4.17. It can be represented as a sequence of the following steps:

- $1 \to 1' \to 2$. We start at the end of the negative phase of the driving $f(t)$ when the system is in the state A. As $f(t)$ changes the phase (to positive), the energy switches to $\Phi(x) + V(y-x) - yA$. After an immediate advance $1 \to 1'$, the bi-stable element goes through the major transition $1' \to 2$ which we identify with the power stroke.
- $2 \to 3$. While the system remains in the positive phase of the loading $f(t)$, the motor makes a step along x direction from the state B to the state B'. This advance along the actin filament is the direct consequence of the power stroke which is here the driving force behind the detachment and reattachment.

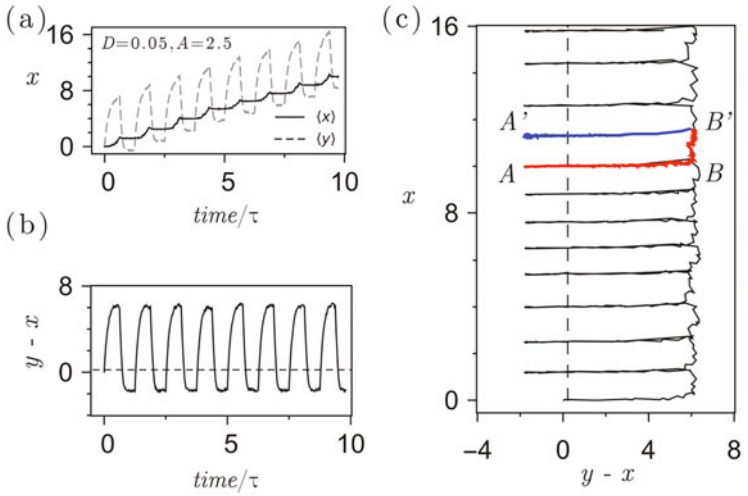

Fig. 4.16 Y-tilted ratchet in the soft device configuration with $f_{ext} = 0$. (**a**) The average trajectories $/\langle x(t)\rangle$ (solid black line) and $\langle y(t)\rangle$ (dashed gray line). (**b**) The time evolution of the system in coordinates $\{t, y - x\}$; (**c**) the average trajectory in coordinates $\{y - x, x\}$. The red lines correspond to the positive phase of the rocking $f(t) = +A$, the blue lines—to the negative phase of rocking $f = -A$. The parameters: $k_0 = 1.5$, $k_1 = 0.43$, $l = 0.35$, $a = 1$, $L = 1$, $\lambda_1 = 0.7$, $\Phi_{max} = 1.5$, $\alpha = 1$, $A = 2.5$, $\tau = 16$, $D = 0.06$

- $3 \to 3' \to 4$. Now the system is in state B', see Fig. 4.16d. The correlated force changes its sign and the energy landscape becomes tilted in the other direction. Following an immediate transition $3 \to 3'$ the power stroke element is recharged through the transition $3' \to 4$. Because of the asymmetry of the actin potential $\Phi(x)$ the coordinate x gets trapped and does not move in the backward direction. Therefore the advance along the actin filament has taken place and the cycle can start again.

Depending on the amplitude of the correlated noise term, the motor step $2 \to 3$ can be longer or shorter. In particular, the system can jump over several periods of the potential $\Phi(x)$. The length of such 'step' is influenced by the fine structure of the energy landscape and also depends on the stiffness of the bi-stable spring.

Hard Device We assume that $z = 0$. The cycles emerging after short transients are illustrated in Fig. 4.18.

At small temperature $D = 0.01$ we observe oscillations between the conformational states A and B inside the same space period of the actin potential ($x = 0$), see Fig. 4.18a. This behavior can be interpreted as a power-stroke (red path) followed by the recharging (blue path) in the attached state. The little loop around the state B is a consequence of the distorted landscape in the hard device. We can therefore speak here about a two-state cycle. With the increase of temperature the Brownian particle is able to explore larger areas of the two-dimensional landscape and at $D = 0.1$ we can stabilize the oscillations between the state A' and B', see Fig. 4.18b. In this case

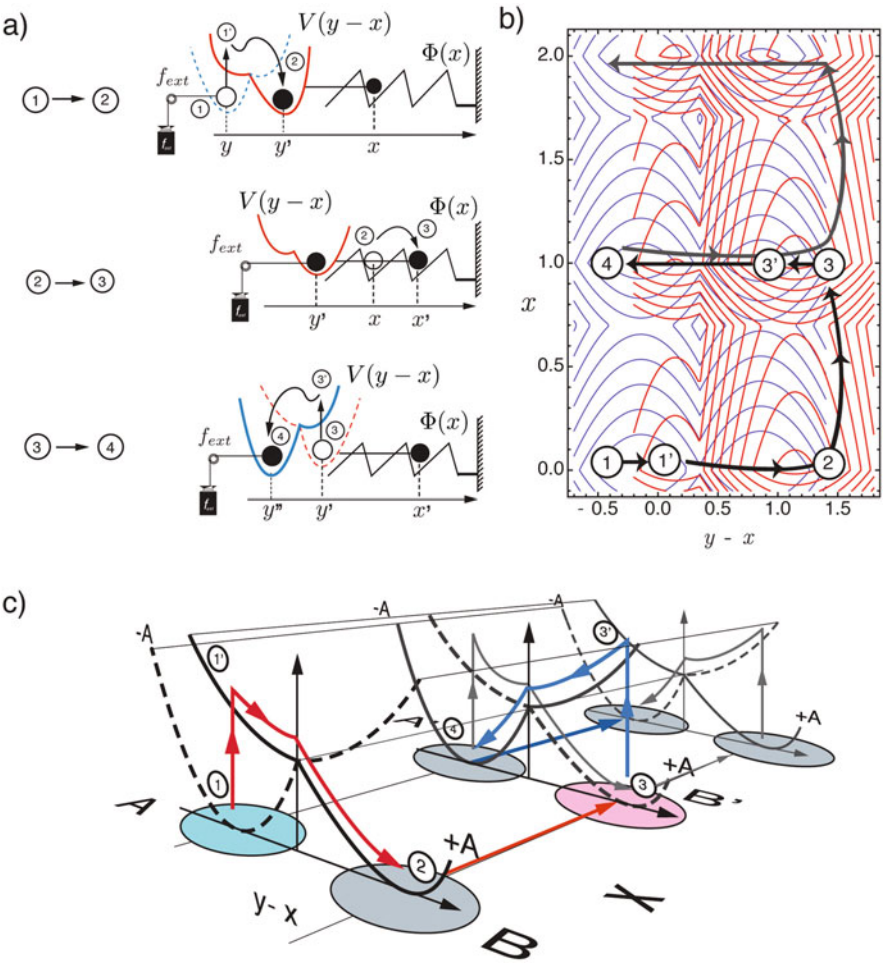

Fig. 4.17 Y-tilted ratchet in the soft device configuration. (**a**) Mechanical representation of the motor cycle. (**b**) Average trajectory superposed with the energy landscape in the positive (solid red lines) and in the negative (solid blue lines) phases of the loading. (**c**) Schematic representation of the major transitions associated with the power stroke element

the system reattaches to a new cite on the actin filament and stretches the spring. As a result, the motor generates much larger average tension, however, the cycle is still composed of only two states. By increasing the temperature further, we are forcing the system to go through a four state cycle, see Fig. 4.18c. Interestingly, in this regime the motor generates smaller tension then in the regime of slightly lower temperature when the cycle consists of two states only. At even higher values of D we still have the four-state cycle but we now occasionally encounter also disadvantageous transitions in the backward direction, see Fig. 4.18d.

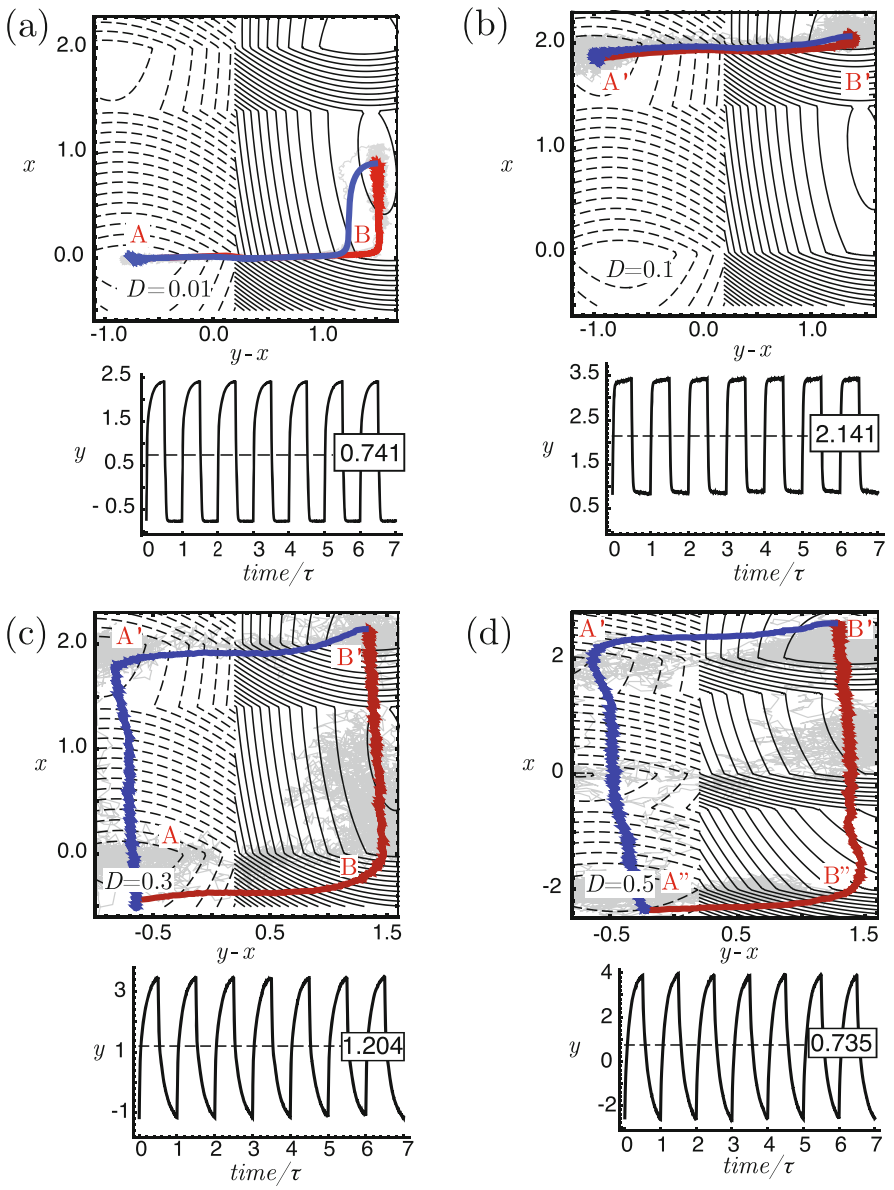

Fig. 4.18 Y-tilted ratchet in the hard device configuration at different temperatures and constant amplitude of non-equilibrium driving $A = 6$. Solid lines represent the energy landscape in the positive and dashed lines—in the negative phase of rocking. The average motor trajectory is shown by the thick red line during the positive and by the thick blue line during the negative phase. The light gray lines follow the single stochastic realization during one time period: (**a**) $D = 0.01$; (**b**) $D = 0.1$; (**c**) $D = 0.3$; (**d**) $D = 0.8$. The parameters: $k_0 = k_1 = 7$, $l = 0.22$, $a = 1$, $L = 2, \lambda_1 = 1.4$, $\Phi_{max} = 5$, $\alpha = 5, k_m = 1$ and $\tau = 20$

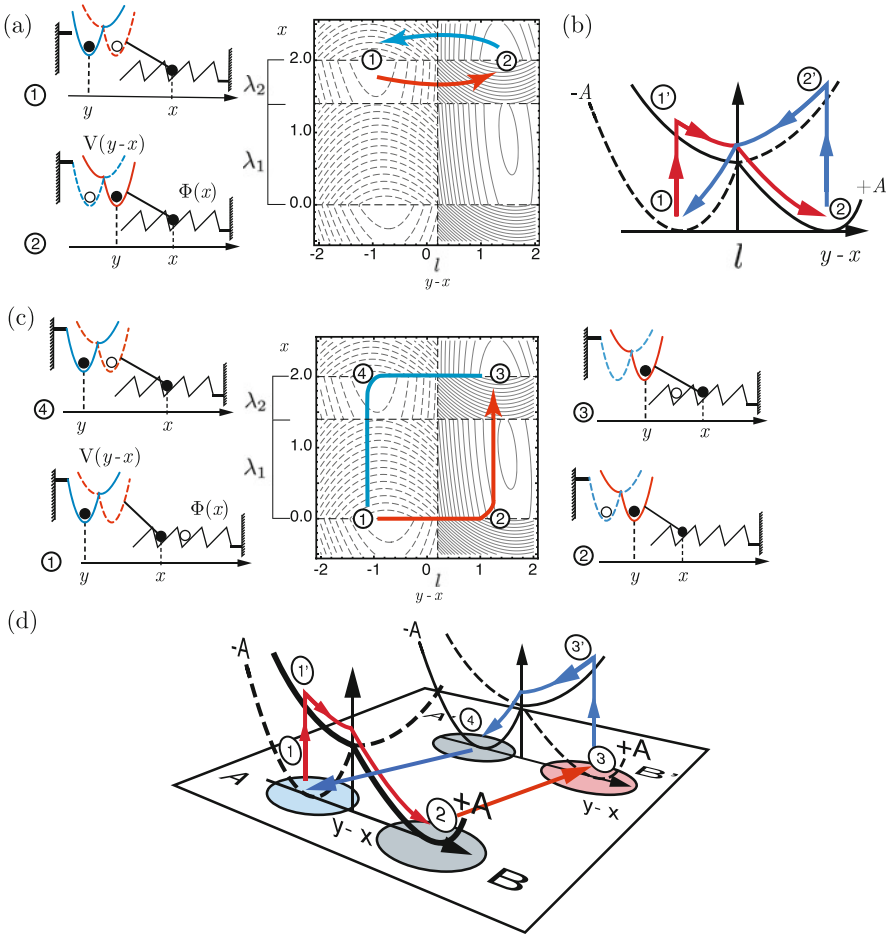

Fig. 4.19 Y-tilted ratchet in the hard device configuration. With solid gray lines we show the energy level contours in positive phases of the rocking when potential is $\Phi(x) + V(y-x) + 1/2k_m y^2 - yA$ while with dashed gray lines we show the energy level contours in the negative phase of rocking when the potential is $\Phi(x) + V(y-x) + 1/2k_m y^2 + yA$. (**a**) The two-state motor cycle, the average trajectory is shown schematically by red arrows in the positive phase and by blue arrows in the negative phase; (**b**) schematic structure of the two-state cycle; (**c**) the four-state motor cycle; (**d**) schematic structure of the four-states cycle

In Fig. 4.19 we present a more systematic comparison of the observed two-state and four-state cycles. In the 'two- state cycle' we observe the following steps:

- $1 \to 1' \to 2$. We start at the end of the phase with the negative tilt. The system explores the state A, see Fig. 4.19b. As the tilt switches to positive, the system makes an immediate transition $1 \to 1'$. From this new configuration the system performs the power stroke $1' \to 2$. The motor then remain in the state B.

- $2 \to 2' \to 1$. While the system is in the state B, see Fig. 4.19b, the correlated noise changes sign, creating again the negative tilt of the energy landscape. The system undergoes an immediate transition $2 \to 2'$. Because of the spatial asymmetry of the actin potential the system remains trapped in the same period of the periodic potential $\Phi(x)$ while the power stroke is recharged performing the transition $2' \to 1$. Then the cycle starts again.

In the 'four-state cycle' the steps are:

- $1 \to 1' \to$. We start again at the end of the negative phase of the rocking. The system explores the state A. As the noise term $f(t)$ changes the value from negative to positive, the system makes an immediate transition $1 \to 1'$, see Fig. 4.19d. From this new configuration the system performs the power stroke $1' \to 2$.
- $2 \to 3$. While in the positive phase of $f(t)$, the system makes a jump into the next nearest well in the positive x direction which is the consequence of the power stroke.
- $3 \to 3' \to 4$. The system is now in the state 3 and the corresponding energy well is B', see Fig. 4.19d. The correlated noise term changes the sign and the system undergoes a transition $3 \to 3'$. Then the instability causes the particle to perform the transition $3' \to 4$, which we interpret as the recharging of the power stroke mechanism.
- $4 \to 1$. From the state A' the motor jumps in backward direction making the transition $4 \to 1$. The system returns into the initial state and the cycle can start again.

To summarize, in the two-state regime the system is residing in a distant, force generating well of the periodic potential while performing periodic oscillations between the two conformational states of the power stroke element. The level of the generate force is high because the cross bridge is firmly attached throughout the cycle. In the four-state regime, the system is periodically reaching the distant well of the periodic potential but remains there only for a limited time before returning back to the original attachment site. In this regime the average force is smaller, however the mechanical cycle is closer to its biochemical analog.

4.4.2 Force-Velocity Relations and Stochastic Energetics

In Fig. 4.20a we show the force-velocity relation at different temperatures D and fixed amplitude of rocking $A = 2.5$. Observe that it is mostly convex at this level of driving. With the increase of temperature the system generates smaller average velocity at zero load and is characterized by smaller stall force. These trends were similar in the case of X-tilted ratchet, see Fig. 4.12. In Fig. 4.20b we show how the force-velocity relation changes when we vary the amplitude of rocking A at the fixed temperature $D = 0.01$. We obtain concave force-velocity relations at small

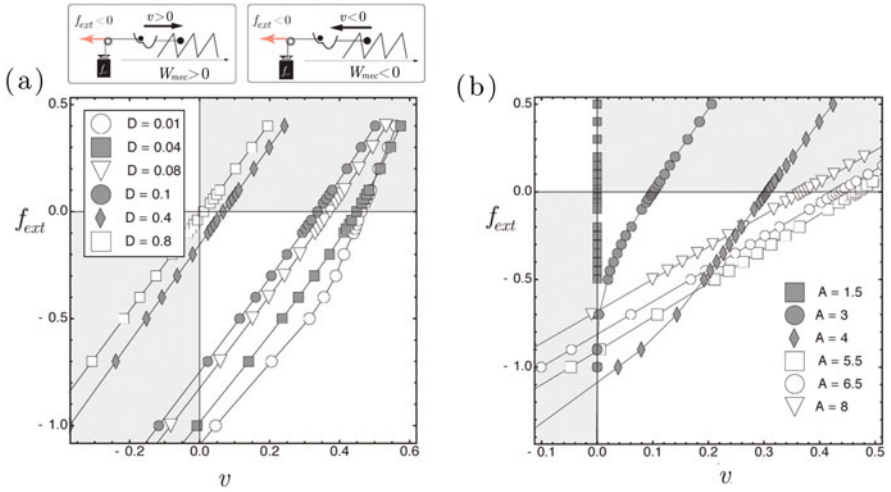

Fig. 4.20 Force velocity relations for the Y-tilted ratchet: (**a**) temperature dependence at $A = 2.5$; (**b**) non-equilibrium noise amplitude dependence at the temperature $D = 0.01$

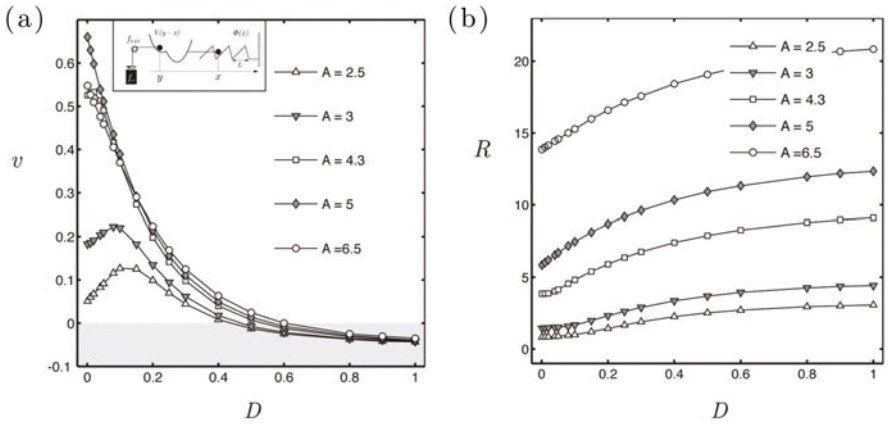

Fig. 4.21 Y-tilted ratchet in the soft device configuration working against the load $f_{ext} = -0.1$: (**a**) temperature dependence of the drift velocity at different values of A; (**b**) Consumed energy R dependence on temperature D at different values of A. The parameters $k_0 = 1.5,\ k_1 = 0.43,\ l = 0.22,\ a = 1,\ L = 1,\ \lambda_1 = 0.7,\ \Phi_{max} = 1.5,\ \alpha = 1$ and $\tau = 60$

amplitude of the driving where we expect that the system to work as a thermal ratchet but then recover the convexity in the interval $1.5 < A \leq 3$.

In Fig. 4.21a we show the average velocity as a function of temperature at different values of the amplitude A. For small amplitudes (thermal ratchet regime) the motor exhibits a maximum of velocity at finite temperature. At higher amplitudes A (mechanical ratchet) the average velocity decreases monotonically with D. Overall the Y-tilted model is generating smaller average velocities than the X-tilted model at the same values of parameters.

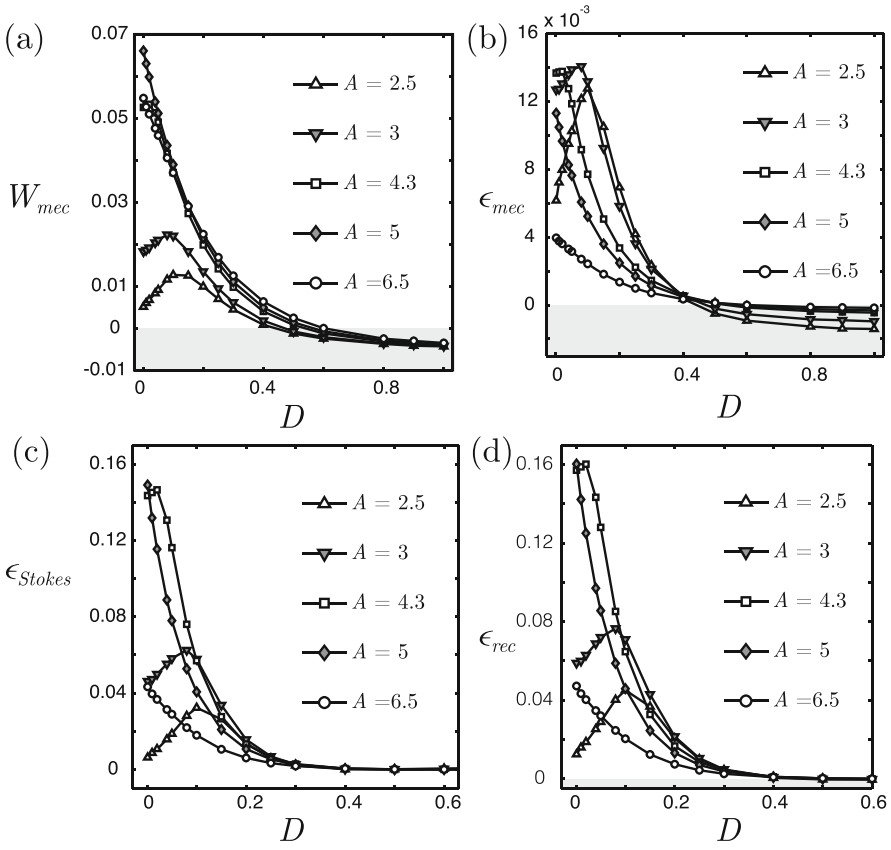

Fig. 4.22 Y-tilted ratchet in the soft device working against the load $f_{ext} = -0.1$. Temperature dependence at different values of A: (**a**) the mechanic work W_{mec}; (**b**) the mechanic efficiency; (**c**) the Stokes efficiency; (**d**) the rectifying efficiency. The parameters are the same as in Fig. 4.21

In Fig. 4.21b we show the consumed energy R as a function of D and use the same range of amplitudes A. As the temperature increases, the motor consumes more and more energy in order to preform useful work. We also again observe a saturation at high temperatures meaning that there is a limit of how much thermal energy the motor can rectify.

Finally, in Fig. 4.22 we show the temperature dependence of the various measures of efficiency at increasing values of A. The qualitative behavior of all these functions is basically the same as in the case of X-tilted ratchet.

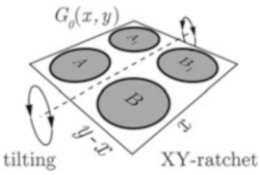

Fig. 4.23 XY-tilted ratchet: the effective tilting of the energy landscape

4.5 XY-Tilted Ratchet

In the XY-tilted ratchet the correlated force $f(t)$ acts on the combination of variables $y - x$, which can be identified with an internal strain inside the bi-stable element. This means that the rocking force affects the power stroke mechanism directly instead of implicitly modifying the internal state of this device through other external degrees of freedom. In Fig. 4.23 we illustrate the mechanical action of the rocking force on the two dimensional energy landscape: note that the ATP activity is now fully decoupled from the actin filament.

In the non-dimensional variables the main system of equations describing the activity of the XY-tilted ratchet in the case of soft device takes the form

$$\begin{cases} dx/dt = -\alpha\left[\partial_x \Phi(x) + \partial_x V(y-x) + f(t)\right] + \sqrt{2\alpha D}\ \xi_x(t), \\ dy/dt = -\partial_y V(y-x) + f_{\text{ext}} + f(t) + \sqrt{2D}\ \xi_y(t). \end{cases} \tag{4.23}$$

In the case of hard device we obtain

$$\begin{cases} dx/dt = -\alpha\left[\partial_x \Phi(x) + \partial_x V(y-x) + f(t)\right] + \sqrt{2\alpha D}\ \xi_x(t), \\ dy/dt = -\partial_y V(y-x) - k_m(y-z) + f(t) + \sqrt{2D}\ \xi_y(t). \end{cases} \tag{4.24}$$

In the corresponding Fokker–Planck equations (4.8) and (4.9) we must use the potential $G^s(x, y, t) = \Phi(x) + V(y-x) - (y-x)f(t) - yf_{ext}$ in the case of the soft device and $G^h(x, y, t) = \Phi(x) + V(y-x) - (y-x)f(t) + \frac{1}{2}k_m(y-z)^2$ in the case of the hard device. In our numerical experiments we used the same choices for the functions $\Phi(x)$, see (4.10), $V(y-x)$, see (4.11) and $f(t)$, see (4.12) as in the previous sections, see Fig. 4.6.

Before turning to the structure of the generated cycles we remark that a conceptually similar approach was used before to describe Kinesin modeled as two coupled rocking ratchets which move along the same periodic potential [78]. The corresponding system of over-damped Langevin equation can be written ass:

$$\begin{cases} dx/dt = -\partial_x \Phi(x) - \partial_x V(x-y) - f(t) + \sqrt{2D}\ \xi_x(t), \\ dy/dt = -\partial_y \Phi(y) - \partial_y V(x-y) + f(t) + \sqrt{2D}\ \xi_y(t), \end{cases} \tag{4.25}$$

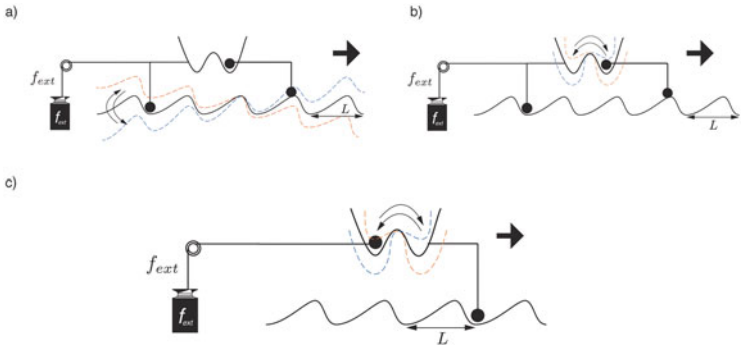

Fig. 4.24 Kinesin-type molecular motors: (**a**) ratchet concept developed in [79]; (**b**) ratchet concept developed in [78]; (**c**) ratchet concept developed here, XY-tilted ratchet

where $\Phi(x)$ and $\Phi(y)$ are two identical ratchet potentials, $V(x-y)$ is the bistable potential describing the interaction between the two legs of the Kinesin motor, whose positions are given by coordinates x and y. Note that here, as in our model, the time periodic rocking acts on the coordinate $x-y$, which indicates the implicit activity of the bistable element, see Fig. 4.24. In contrast to such 'two-leg' designs describing processive motors, our 'one-leg' design concerns non-processive motors.

4.5.1 Motor Cycles

Soft Device In Fig. 4.25 we show the averaged trajectory of the XY-tilted ratchet exposed to a rocking force with amplitude $A = 0.6$ and simultaneously subjected to a thermal noise with $D = 0.02$. The system follows a three-state cycle: it performs a power-stroke while being attached to one particular state on the periodic landscape and then moves in the forward direction along this landscape, while recharging the power-stroke mechanism. The change of sign of the tilting force $f(t)$ both re-activates the power-stroke mechanism and causes the directional motion of the motor. The amplitude of the tilting strongly influences the shape of the energy landscape, in particular, in each phase, positive and negative, the intrinsic bi-stability of the potential in the $y-x$ direction may be either preserved or not. In Fig. 4.26 we schematically show the states visited by the motor during one cycle:

- $1 \rightarrow 1' \rightarrow 2$. We start the cycle at the very end of the negative phase of the rocking, see Fig. 4.26 when the system explores the state A. As the force $f(t)$ changes from negative to positive, the energy becomes $\Phi(x)+V(y-x)-(y-x)A$ and the particle makes a transition $1 \rightarrow 1'$. During the positive phase of the rocking the system undergoes the transition $1' \rightarrow 2$ which we identify with the power stroke.

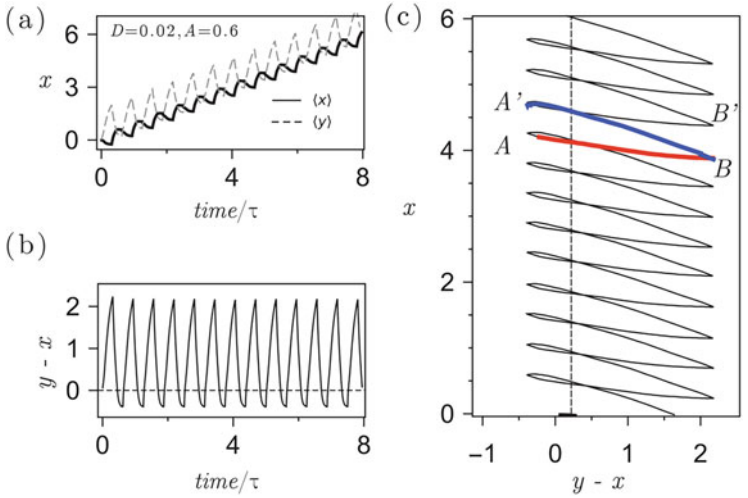

Fig. 4.25 XY-tilted ratchet in the soft device configuration with $f_{ext} = 0$: (**a**) Trajectories $\langle x(t)\rangle$ (solid black line) and $\langle y(t)\rangle$ (dashed gray line); (**b**) time evolution of the system in coordinates $\{t, y-x\}$; (**c**) average trajectory in coordinates $\{y-x, x\}$; red line correspond to the rocking phase $f(t) = +A$, blue lines—to the phase $f = -A$. The parameters $k_0 = 1.5$, $k_1 = 0.43$, $l = 0.35$, $a = 1$, $\lambda_1 = 0.35$, $L = 0.5$, $\Phi_{max} = 1$, $\alpha = 1$ and $\tau = 16$

- $2 \to 3' \to 3$. We are now in state 2 corresponding to the state B, see Fig. 4.25. The rocking force changes the sign and the energy becomes $\Phi(x) + V(y-x) + (y-x)A$. The system makes the step $2 \to 3'$, and since the bistable potential is now biased, the motor performs an additional transition $3' \to 3$, finalizing the recharging of the power stroke element. Because of the spatial asymmetry of the periodic potential the attachment site does not change during such recharging. Then the cycle starts again.

Note that the motor advance and the recharging of the power stroke take place simultaneously. Those are the two stages where the external energy supply is necessary and they cannot be separated in this setting.

Hard Device We fix the total displacement at $z = 0$ and show in Fig. 4.27 the simplest motor cycles. At low temperatures the system moves only between the states A and B. This means that the cross bridge is attached to a particular site of the actin potential while performing random work between two configurations of the power stroke element. With the increase of temperature D the motor eventually crosses the energy barrier (detaches) and then stabilizes (attaches) in the next site on the actin filament. In this new attached position the motor continues to perform the transitions between state A' and state B', see Fig. 4.27b. Observe that now the attachment site is distant from the reference position, the spring is stretched and the motors shows higher levels of tension comparing to the cycle shown in Fig. 4.27a.

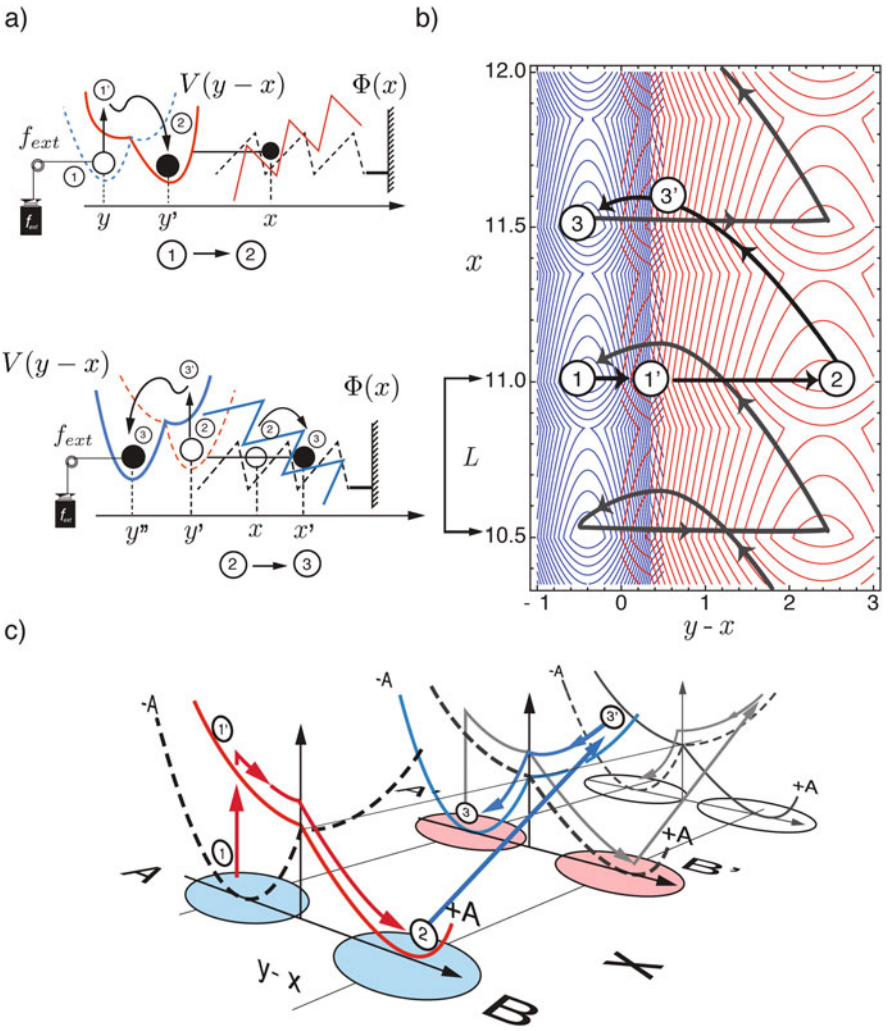

Fig. 4.26 Schematic cycle of the XY-tilted ratchet in the soft device configuration: (**a**) mechanical representation of the motor cycle; (**b**) averaged trajectory; (**c**) the cycle showing the energy changes associated with different moves of the system in the space $((y-x), x)$

By increasing the temperature and the amplitude of rocking further, we force the motor to visit more sites on the energy landscape. Thus in Fig. 4.27c the motor periodically changes the attachment site: the cycle is performed between the state A' and the state B, corresponding to different attachment sites along the potential $\Phi(x)$. In this regime the motor is able to generate the highest level of average tension. We see first motor detachment and advance, accompanied by the recharging of the power stroke element, and then the power stroke combined with re-attachment

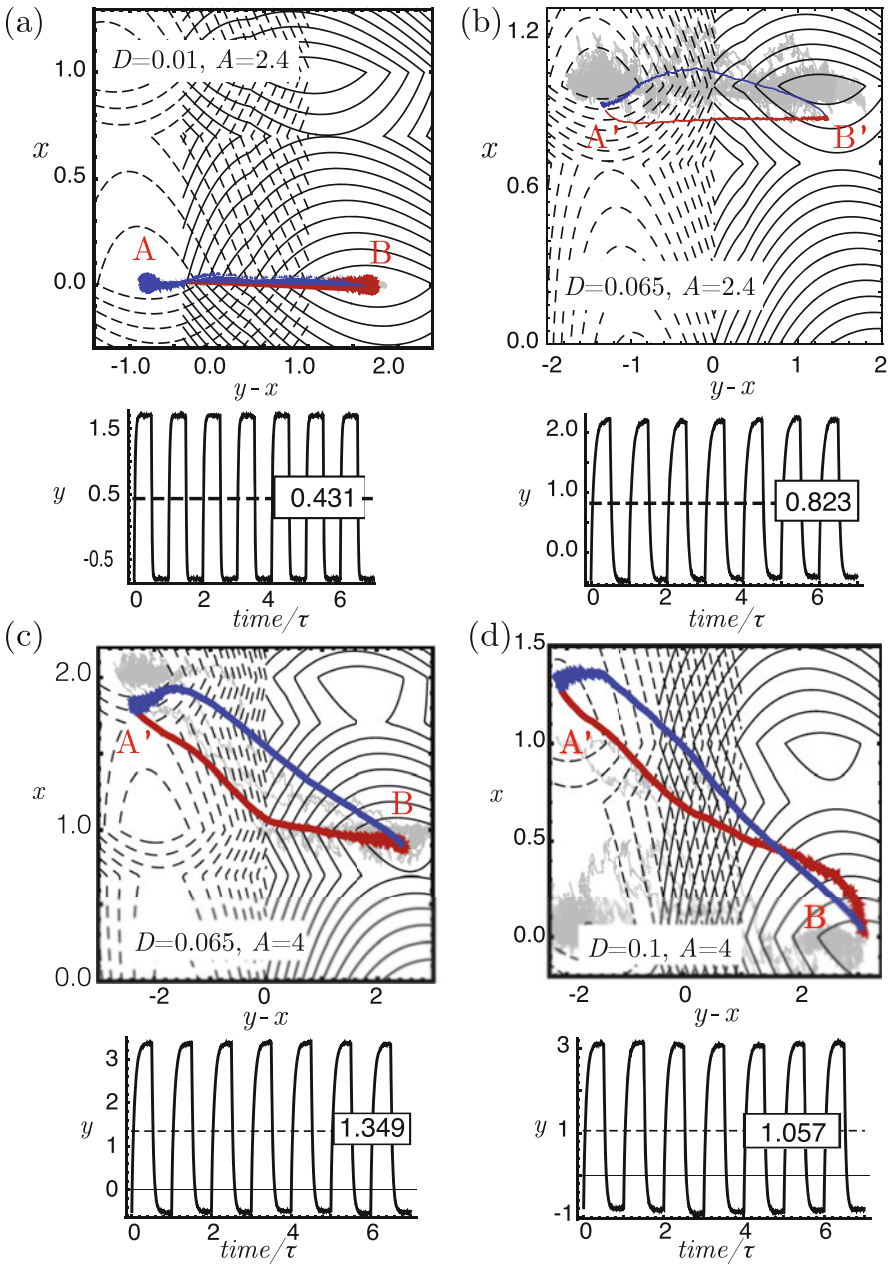

Fig. 4.27 XY-tilted ratchet model in the hard device configuration with $z = 0$. The dependence of the motor cycle on the temperature D and the rocking amplitude A: (**a**) $D = 0.01$, $A = 2.4$; (**b**) $D = 0.065$, $A = 2.4$; (**c**) $D = 0.08$, $A = 4$; (**d**) $D = 0.1$, $A = 4$. The parameters $k_0 = 1.5$, $k_1 = 0.43$, $l = 0.35$, $a = 1$, $\lambda_1 = 0.7$, $L = 1$, $\Phi_{max} = 1.5$, $\alpha = 1$ and $\tau = 10$

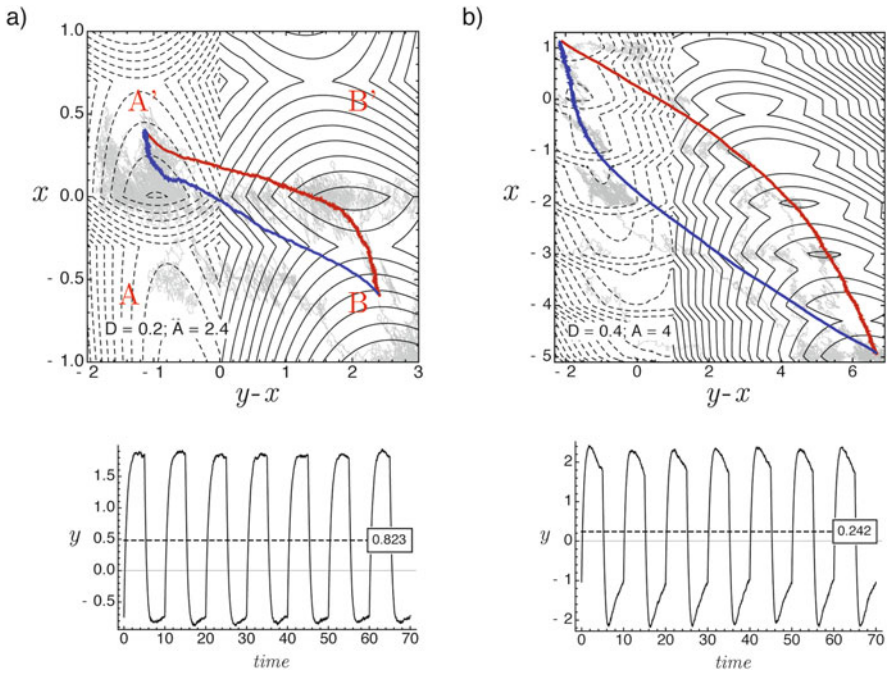

Fig. 4.28 XY-tilted ratchet model in the hard device configuration: (**a**) $D = 0.2,\ A = 2.4$; (**b**) $D = 0.4;\ A = 4$. Other parameters are the same as in Fig. 4.27

bringing the system to the original site. Once again, the two biochemical steps appear coupled in this mechanical setting. The slanted two-state cycle is preserved also at higher values of D, see Fig. 4.27d. The fine structure of the cycle, however, is now a bit different because higher level of noise stimulates additional spurious transitions inside the landscape. At even larger temperature the device progressively looses its ability to rectify thermal fluctuations. In particular, at sufficiently high temperatures the motor changes the direction in which the motor cycle is performed. Thus, in Fig. 4.28a, b the cycle is performed in the direction opposite to what we have seen in Fig. 4.27.

To summarize, we now present the schematic structure of the simplest two-state hard device cycle shown in Fig. 4.29.

- $1 \to 1' \to 2$. We start at the end of the negative phase of the rocking when the system explores the state A. Then the force f changes sign and the system makes the transition $1 \to 1'$. During the positive phase of the rocking the particle performs the transition $1' \to 2$, which we associate with the power stroke.
- $2 \to 2' \to 1$. We are now in the state B. The rocking force changes sign and the system makes the transition $2 \to 2'$. Because of the spatial asymmetry of the periodic potential, the system remains trapped in the 'distant minimum' of $\Phi(x)$

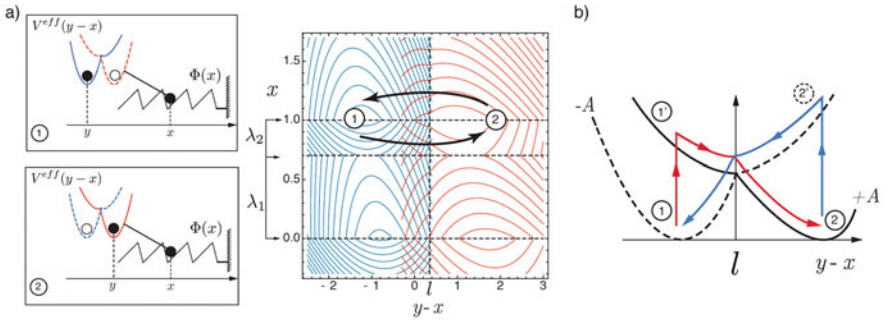

Fig. 4.29 Schematic representation of the XY-tilted ratchet cycle in the hard device corresponding to the trajectory shown in Fig. 4.27a: (**a**) two-state motor cycle; (**b**) energetics of the two-state cycle

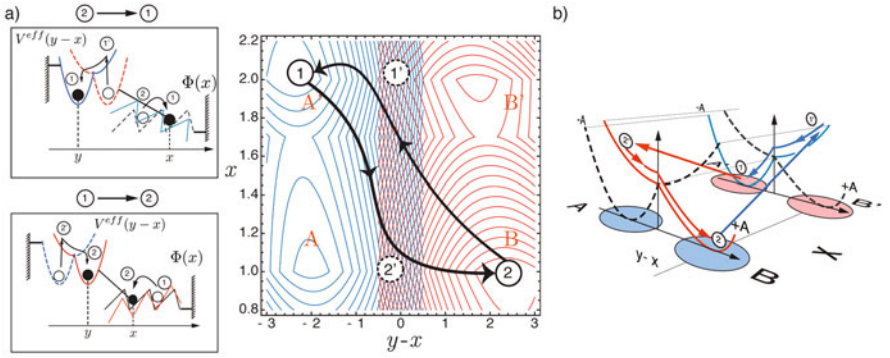

Fig. 4.30 Schematic representation of the XY-tilted ratchet cycle in the hard device corresponding to the trajectory shown in Fig. 4.27d: (**a**) 'slanted' two-state motor cycle; (**b**) energetics of the 'slanted' two-state cycle

while performing the transition $2' \to 1$, which we interpret as the recharging of the power stroke. Then the cycle can start again.

In Fig. 4.30 we similarly illustrate the (low temperature) 'slanted' two-state cycle corresponding to what we have seen in Fig. 4.27d. Formally, the motor visits only two sites corresponding to the stable states A' and B', see Fig. 4.30a. However, because of the peculiar shape of the cycle we can distinguish two additional intermediate states marked as $1'$ and $2'$. With these additional states taken into consideration we can interpret the ensuing periodic trajectory as the following four-states cycle:

- $1 \to 2' \to 2$. We start again at the end of the negative phase of the rocking when the system explores the state A'. Then the force f changes its sign from negative to positive and the system makes a transition $1 \to 2'$ 'moving back' along the x coordinate. During the positive phase of the rocking the system performs an

additional transition $2' \rightarrow 2$ and finds itself in the state B. We interpret the transition $2' \rightarrow 2$ as the power stroke.

- $2 \rightarrow 1' \rightarrow 1$. We now are in the state 2, point B. The correlated force changes its sign again, from positive to negative. The system detaches and makes a 'forward jump' to the next site along the actin filament performing the transition $2 \rightarrow 1'$. Subsequently the particle continues with the transition $1' \rightarrow 1$ which we interpret as the recharging of the power stroke mechanism. Then, the cycle can start again.

4.5.2 Force-Velocity Relations and Stochastic Energetics

In Fig. 4.31a we show the effect of temperature at low amplitudes of rocking $A = 2.5$ on the force velocity relations for a XY-tilted ratchet. At zero temperature the system exhibits purely mechanical behavior without any 'anti-dissipation' (no entrance into the white quadrants). The growth of temperature D increases the area between the force-velocity curve and the axes in the domain of anti-dissipative behavior. We observe the pronounced concave character of the force-velocity relations at sufficiently low temperatures. After the threshold in D the concavity progressively vanishes and the profile becomes linear, while the motor loses its ability to carry the cargo. In Fig. 4.31b we illustrate the dependence of the force-velocity relation on A at fixed $D = 0.02$. At small amplitudes of rocking the motor follows closely the external force f_{ext} and does not perform useful mechanical work.

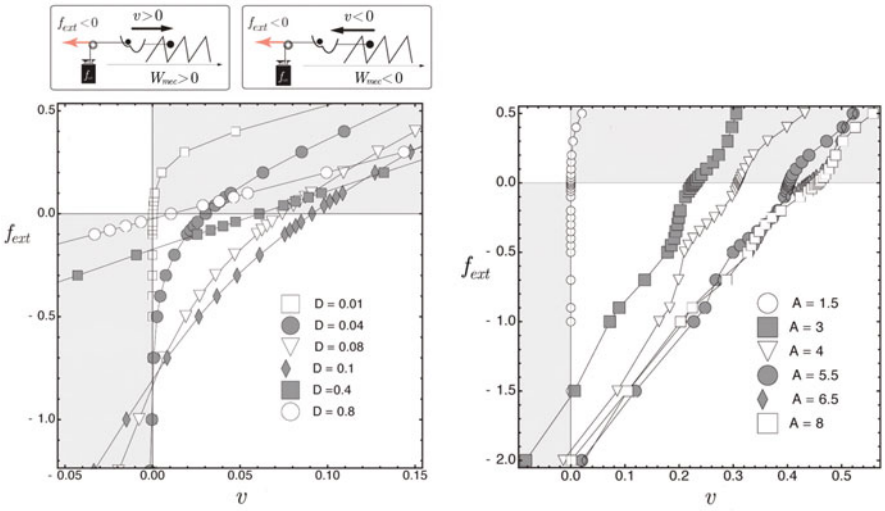

Fig. 4.31 The XY-tilted ratchet in soft device configuration: (**a**) dependence of the force-velocity relation on temperature D at the fixed $A = 2.5$; (**b**) dependence of the force-velocity relation on A at the fixed temperature $D = 0.02$. Parameters are the same as in Fig. 4.27

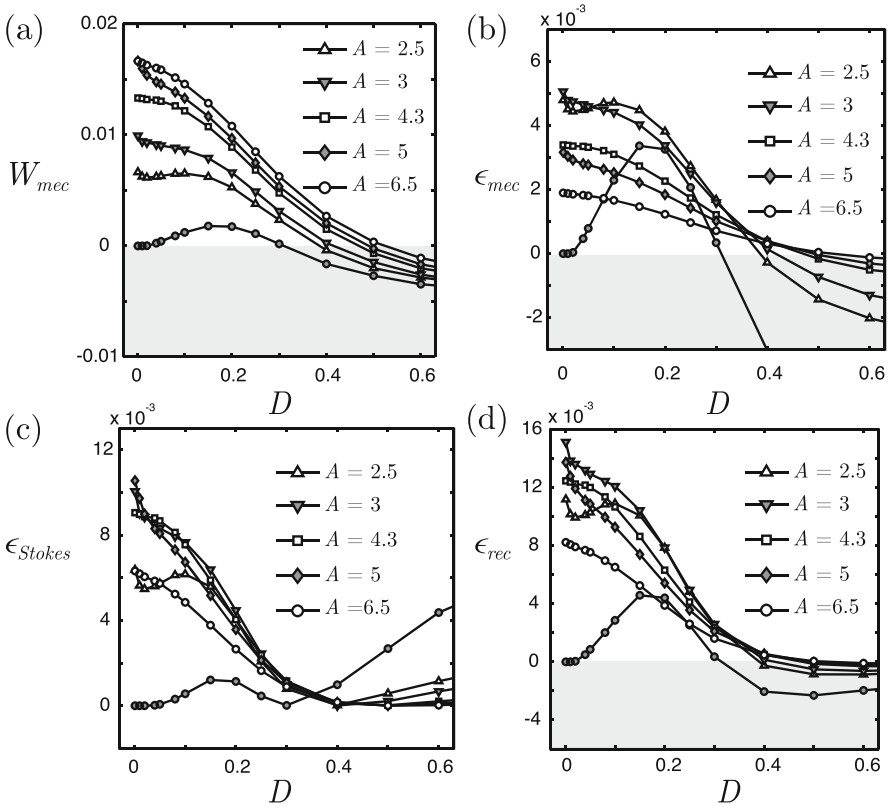

Fig. 4.32 XY-tilted ratchet in the soft device configuration working against the fixed load $f_{ext} = -0.1$. (**a**) the mechanical work W_{mec}; (**b**) the mechanical efficiency; (**c**) the Stokes efficiency; (**d**) the rectifying efficiency. Parameters are the same as in Fig. 4.27

Only after a certain threshold in amplitude the motor starts to generate active drift against the load.

In Fig. 4.32a we show the mechanical work as a function of D at different amplitudes of the rocking amplitude A. We observe two regimes: with positive and with negative mechanic work. In Fig. 4.32b we present the mechanical efficiency. At small amplitudes A we observe a maximum of the efficiency at finite temperature. With increasing A the maximum vanishes and the efficiency becomes a monotonically decreasing function of D, as one can expect in a purely mechanic ratchet. By light green color we indicated the regimes with the negative efficiency, where dissipation prevails. In Fig. 4.32c we present the Stokes efficiency as a function of D. We observe maxima on the efficiency vs D curve corresponding to finite temperatures and low rocking amplitudes regimes and also see that in some regimes the Stokes efficiency may increase with temperature. The rectifying efficiency is shown in Fig. 4.32d. Once again, at small amplitudes of rocking we see

thermal ratchet behavior with a maximum of efficiency at finite temperature while at high rocking amplitudes we see the mechanical ratchet behavior with efficiency decreasing with temperature.

4.6 Comparison of the Three Models

We introduced above three minimal mechanistic models which all describe muscle contraction in terms of Langevin dynamics of a mechanical system. By localizing the mechanical effects of the ATP-related activity on a single internal degree of freedom, we could study separately the possibilities that actin filament is active (X model), that the coupling between the attachment/detachment and the power stroke elements is active (Y model) and that the power stroke element itself is active (XY model). Now we chose a single set of parameters and compare directly the resulting force-velocity relations and the efficiencies of the associated energy transduction mechanisms. To allow such a comparison we continue to use the simplest descriptions of the functions $\Phi(x)$, $V(y-x)$ and $f(t)$ shown in Fig. 4.6.

To produce a realistic description of muscle contraction we use the time scale $t^\star = \eta_y/k_m \sim 0.2\,\text{ms}$ where $\eta_y \sim 0.38\,\text{ms}\cdot\text{pN/nm}$ is the micro-scale viscosity [19] and where $k_m \sim 2\,\text{pN/nm}$ is the stiffness of the elastic part of the myosin motor [7, 67]. The spatial scale is then $l^\star = a$ where $a \sim 10\,\text{nm}$ is the distance between two minima of the pre and post power stroke wells [69]. Then the energy scale is $\epsilon^\star = k_m a^2 \sim 200\,\text{pN}\cdot\text{nm}$. We assume that $D = k_B\Theta/(k_m a^2) \sim 0.02$ where $k_B = 4.10\,\text{pN}\cdot\text{nm}$ is the Boltzmann constant, $\Theta \sim 300\,\text{K}$ is the ambient temperature, and $a = 10\,\text{nm}$ is the characteristic size of a motor power-stroke [69]. For the active driving we obtain $\tau = \tau_{ATP}/(\eta/k_m) \sim 100$ where $\tau_{ATP} = 40\,\text{ms}$ is the characteristic time of ATP hydrolysis [53]. We can now write $A = \sqrt{\Delta\mu/(k_m a^2)} \approx 1$ where $\Delta\mu = 20 k_B\Theta$ is the typical value of degree of non-equilibrium in terms of the affinity of ATP hydrolysis reaction [53]. Finally we assume that the non-dimensional parameters of the bi-stable potential take the values [19]: $k_0 = 1.5,\ k_1 = 0.43,\ l = 0.35,\ a = 1$. The space periodic potential is characterized by the parameters $\lambda_1 = 0.7,\ L = 1,\ \Phi_{max} = 1.5$ and in most illustrations we suppose for simplicity that $\alpha = 1$.

4.6.1 Soft Device

In Fig. 4.33 we compare the drift velocities generated by X, Y and XY-tilted ratchets in the soft device. The common feature of all three systems is that they exhibit the phenomenon of stochastic resonance: the average velocity is maximized at a particular value of temperature. At large temperatures all three systems progressively lose the capacity to rectify thermal fluctuations. In the regimes with high amplitude of the rocking the stochastic resonance disappears and the average

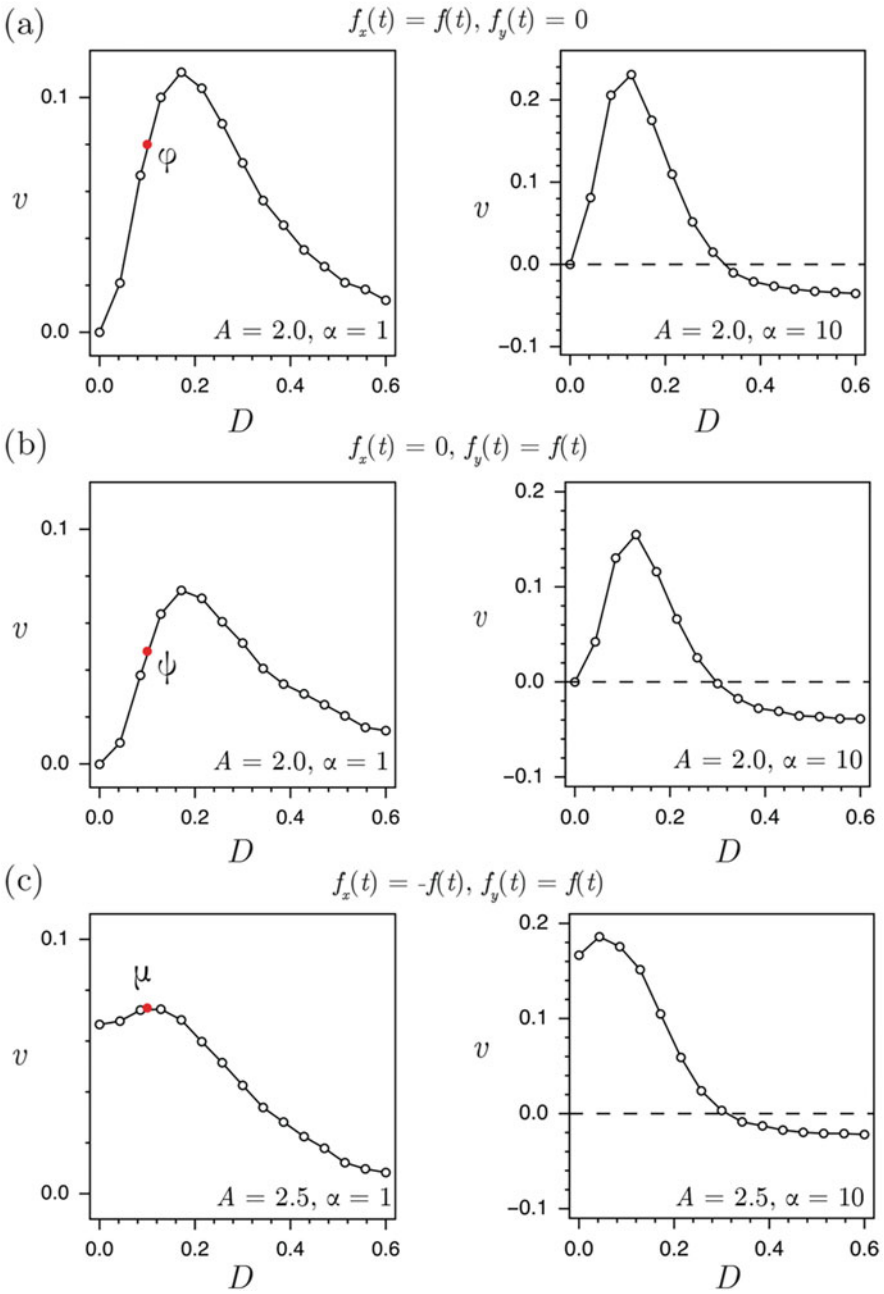

Fig. 4.33 The performance of different motors in soft device conditions with $f_{ext} = 0$. Average velocity v as a function of temperature D at different values of the amplitude A for X ratchet (**a**), Y ratchet (**b**), XY ratchet (**c**). Here the correlation time $\tau = 30$

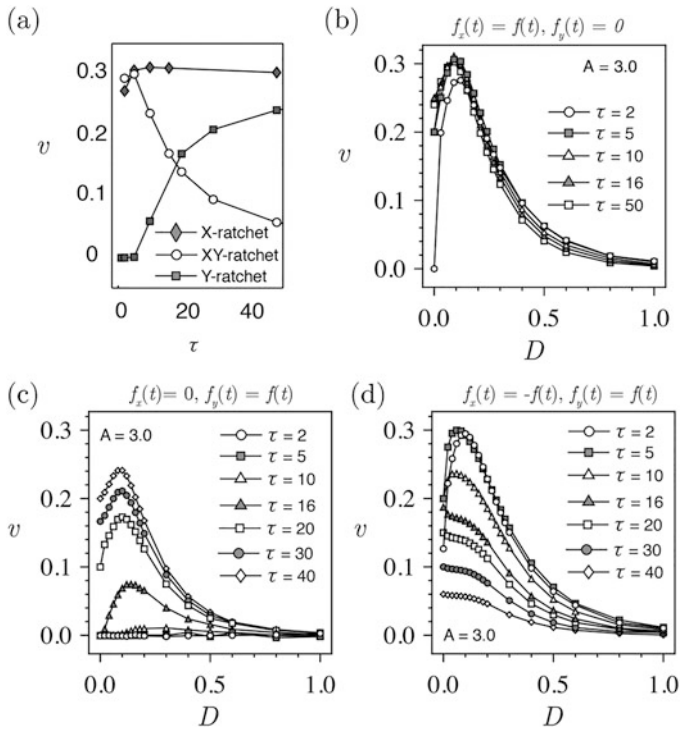

Fig. 4.34 (**a**) The dependence of the average velocity on the correlation time τ at $A = 3$ and $D = 0.08$. The variation of the average velocity with temperature D for X-ratchet (**b**), Y-ratchet (**c**) and XY-ratchet (**d**). Here $\alpha = 1$

velocity becomes a monotonically decreasing function of D. This is an indication that in all three cases the nature of the ratchet changes from Brownian to purely mechanical. Observe also that at $\alpha = 10$ (in the right column of Fig. 4.33) all three motors change their direction of the motion because of an additional asymmetry in the system which competes with polarity of the actin filament.

In Fig. 4.34 we compare the average velocities in the three models at different values of the correlation time τ characterizing the driving $f(t)$. In the case of X ratchet, Fig. 4.34a, the influence of τ is minimal. This suggests that for small and moderate amplitudes of rocking, the ratchet behavior can be well approximated by the effective model with adiababtically eliminated fast variable y. The Y ratchet is operational over a broad interval of the periods τ. Instead, the XY ratchet is functional only for sufficiently small values of τ. In Fig. 4.35, we compare the dependence of the average velocity v on temperature D at several values of the rocking amplitude A.

In Fig. 4.36 in the left column we compare the average trajectories for X, Y and XY ratchets at the points φ, ψ and μ marked in Fig. 4.33. As before, we use red color to identify the part of the cycle associated with the positive phase of the rocking, and

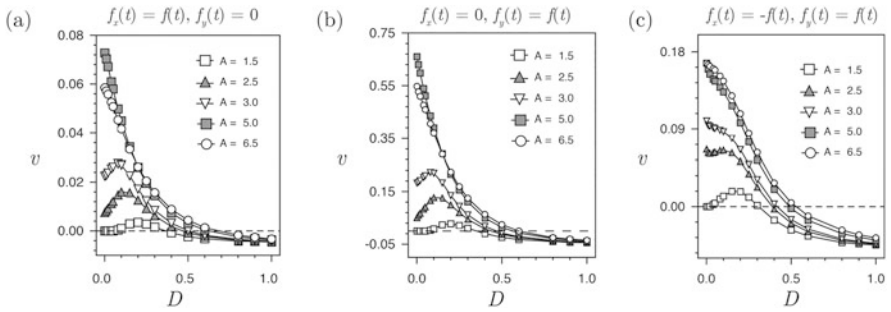

Fig. 4.35 The dependence of the average velocity v on temperature D at $f_{ext} = -0.1$; X ratchet (**a**); Y ratchet (**b**); XY ratchet (**c**). The parameters: $\alpha = 1$ and $\tau = 30$

blue color for the path associated with the negative phase. The dotted line shows the boundary between left and right wells of the bi-stable potential and we associate its crossing with either release or re-cocking of the power stroke mechanism.

For the X-tilted ratchet shown in Fig. 4.36a we obtain a three-state cycle, where the detachment and the re-attachment take place simultaneously with the recharge of the power stroke. For the Y-tilted ratchet shown in Fig. 4.36b we obtain a four -state cycle. Note that here, the motor releases and recharges the power-stroke mechanism actively, moreover without the power-stroke activity the motor won't be able to move. Finally, for the XY -tilted ratchet shown in Fig. 4.36c we again obtain a three-state cycle. First, it performs a power-stroke while being attached to one particular site on the periodic landscape $\Phi(x)$ and after that it moves forward along the potential $\Phi(x)$, while in same time recharging the power-stroke mechanism. Here again the motor advance and the recharging of the power stroke take place simultaneously.

In Fig. 4.37 we compare the force velocity relations at different temperatures D and fixed rocking amplitude $A = 2.5$. At zero temperature all three systems exhibit purely mechanical depinning behavior without showing any "anti-dissipation". At finite temperatures we obtain the concave force-velocity relations in agreement with experimental observations [62, 87, 125]. After the threshold $D \approx 0.1$ the force velocity relations becomes almost linear and eventually the motors lose their ability to carry cargo. The XY-tilted ratchet shows the highest stall force value among the three type of devices.

4.6.2 Hard Device

In Fig. 4.38 we compare the average tension generated by the motors in the hard device at different temperatures D and rocking amplitudes amplitude A. The active tension is optimized at a finite value of D for all configurations given that the amplitude of the correlated noise is sufficiently low.

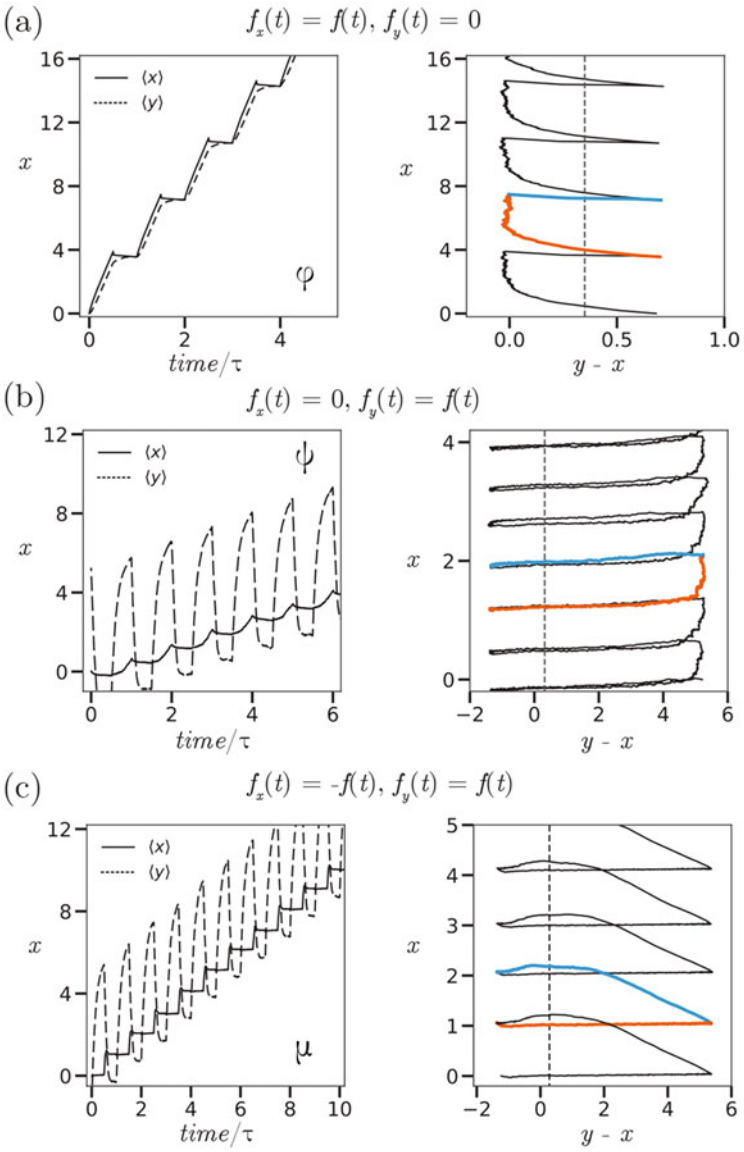

Fig. 4.36 Typical trajectories of the three motors in the soft device with $f_{ext} = 0$: (**a**) X-tilted ratchet; (**b**) Y-tilted ratchet; (**c**) XY-tilted ratchet. The parameters: $\alpha = 1$ and $\tau = 30$

At low temperatures and low amplitudes of rocking the X-tilted ratchet generates small tension because the energy transmitted to the motor is not sufficient to activate the bi-stable element. The Y-tilted ratchet shows the plateau regimes, where the system acts as simple mechanical bi-stable element. The XY-tilted

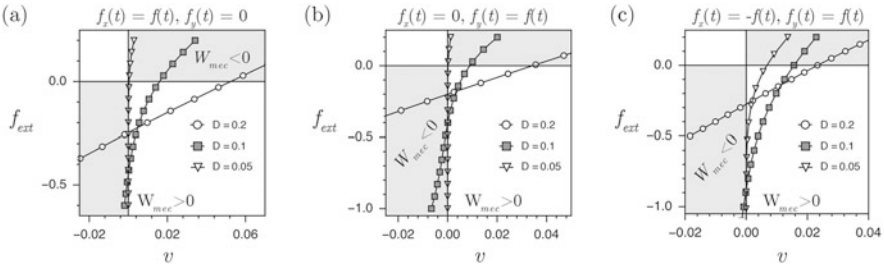

Fig. 4.37 Comparison of the force-velocity relations at fixed $A = 1.5$ for: X ratchet (**a**), Y ratchet (**b**), XY ratchet (**c**). The parameters: $\alpha = 1$ and $\tau = 30$

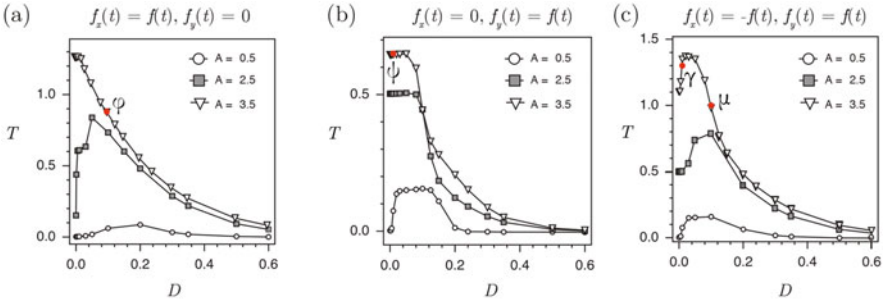

Fig. 4.38 The dependence of the average tension T on temperature D for: X-tilted ratchet (**a**), Y-tilted ratchet (**b**) and XY -tilted ratchet (**c**). The parameters $k_0 = 1.5$, $k_1 = 0.43$, $l = 0.35$, $L = 1$, $\lambda_1 = 0.7$, $\Phi_{max} = 1.5$,$\tau = 30$, $\alpha = 1$, $k_m = 1$ and $z = 0$. Under these conditions the averaged tension T is equal to $\langle\langle y \rangle\rangle$

ratchet demonstrates a hybrid behavior exhibiting the temperature and the amplitude thresholds whose crossing allows the motor to form a cycle. Such regime takes advantage of both, the thermal fluctuations and the correlated noise.

The structure of the motor cycle—the sequence of visited energy minima during different stages of the rocking—is the unique signature of each device. The most interesting motor cycles generated at $z = 0$ in each of our three devices are presented in Fig. 4.39. Again, the average motor trajectory is plotted by red during the positive and in blue line during the negative phase of the rocking. The light gray trajectories show single stochastic realizations. The corresponding tension curves are shown in Fig. 4.40.

As we have already seen, in the hard device, the X-tilted is trapped in a single energy well of the double well potential and the power stroke element does not contribute to force generation. We can force the X-tilted ratchet to visit both minima of the double well potential if we use somewhat less realistic parameters, $k_0 = 7$, $k_1 = 7$, $l = 0.22$, $L = 2$, $\lambda = 1.4$, $\Phi_{max} = 5$ and $\alpha = 5$. Such cycle is formed only when the motor makes sufficiently large steps along the coordinate x and can therefore recharge the power stroke element. After a transient stage, an X-tilted ratchet with these parameters performs the cycle in the clockwise direction:

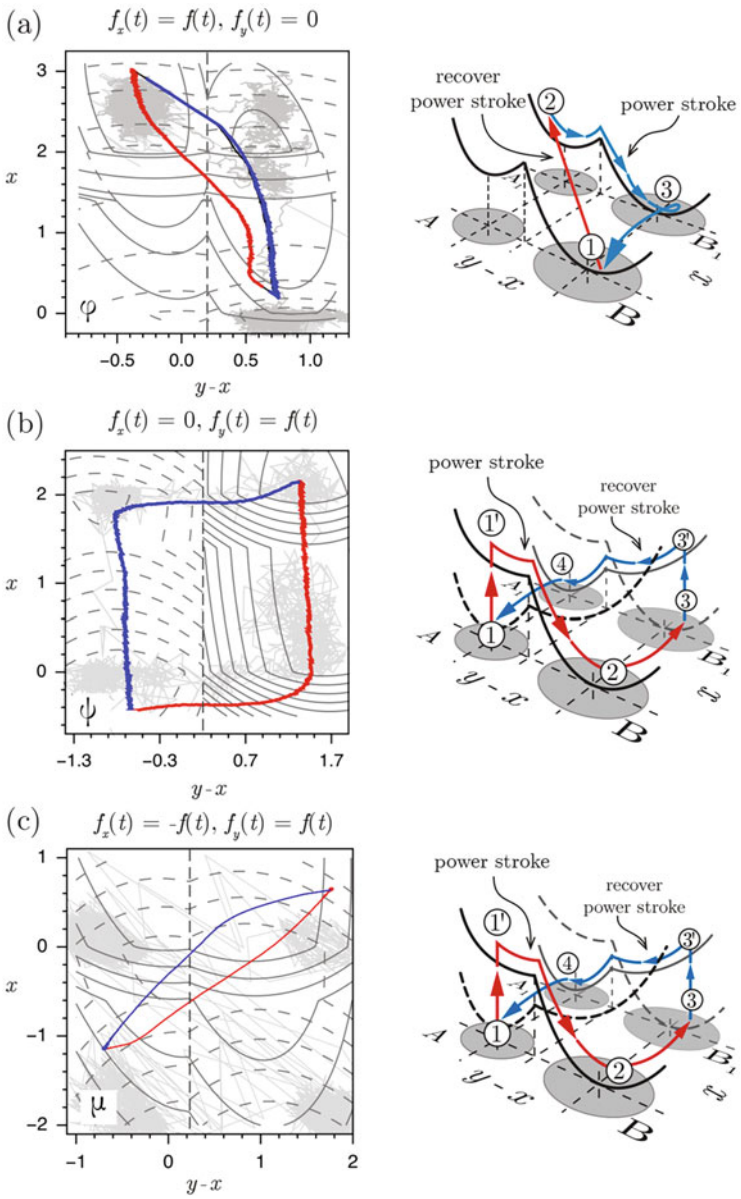

Fig. 4.39 The most complex motor cycles in hard device at $z = 0$: (**a**) X ratchet, (**b**) Y ratchet, (**c**) XY ratchet. The parameters $k_0 = 7,\ k_1 = 7,\ l = 0.22,\ L = 2,\ \lambda = 1.4,\ \Phi_{max} = 5, \tau = 20,\ \alpha = 5$

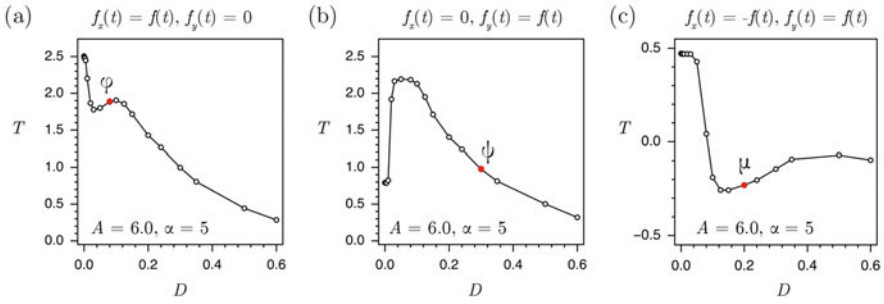

Fig. 4.40 Average tension T versus temperature D in: X ratchet (**a**), Y rathet (**b**) and XY ratchet (**c**). The parameters are the same as in figure above

$1 \rightarrow 2$. Due to the broken space symmetry, the motor advances in the x direction and crosses the energy barrier along the periodic potential $\Phi(x)$. In the meanwhile the motor recharges the power stroke element (performs the transition from the lower energy well B to the higher energy well A_1 in the bistable potential). During the next step $2 \rightarrow 3$, as the rocking force changes its sign, the new configuration of the energy landscape forces the motor into backward direction along the x axis. However, the motor is now trapped and instead of going backwards, it performs the power-stroke. Then the motor cycle starts again.

Consider now the Y-tilted ratchet. If we choose parameters as in the case of X-ratchet above we obtain the four-state cycle shown in Fig. 4.39b. The system reattached and jumps to a new cite on the actin filament while stretching the bistable spring. This behavior can be interpreted as a power-stroke (red path) followed by the recharging (blue path) in the attached state. The motor first goes through mechanical configurations A, B and then through the configurations B_1, A_1. In the ensuing four-state cycle the stages are: the transition $1' \rightarrow 2$ is the power stroke, then, as the motor makes a jump into the next nearest well along the actin filament (in the positive x direction) the rocking force changes sign forcing the recharging of the power stroke mechanism, $3' \rightarrow 4$.

Note that in the corresponding two-state cycle obtained in the section on Y-tilted ratchets, the system was residing in a distant, force generating well of the periodic potential while performing periodic oscillations between the two conformational states of the power stroke element. The level of the generate force was high because the cross bridge was firmly attached throughout the cycle. In the four-state regime studied here, the system is periodically reaching the distant well of the periodic potential as well, but remains there only for a limited time before returning back to the original attachment site. In such regimes the average force is necessarily smaller.

Our Fig. 4.39c shows the typical cycle exhibited by the XY ratchet in the hard device. The motor periodically changes the attachment site: the cycle is performed between the state A_1 and the state A, B, corresponding to different attachment sites along the actin filament. In this regime the motor is able to generate the highest level of average tension. The three- state cycle can be interpreted as follows: first motor detachment and advance accompanied by the recharging of the power stroke device

and then the power stroke combined with re-attachment brings the system into the original site.

4.6.3 Stochastic Energetics

We now apply to all devices the same conservative load $f_{ext} = -0.1$. In Fig. 4.41a we illustrate the temperature dependence of the mechanical efficiency for the X-tilted ratchet. In the regime of small amplitudes A we observe a maximum at finite temperature. The negative values of efficiency indicate the regimes where the motor is unable to perform a positive mechanic work against the external force and works instead as an active breaking mechanism. The Stokes efficiency, also shown in Fig. 4.41a, is always positive by definition.

We illustrate the efficiency of the Y-ratchet in Fig. 4.41b. Overall this ratchet is less efficient when the X ratchet. We can explain this difference by the design of the active mechanism: the metabolic energy is taken by the bi-stable element and therefore only partially consumed by the forward steps long the x direction.

Finally, the performance of the XY tilted ratchet is illustrated in Fig. 4.41c. At small amplitudes A we again observe a maximum of the mechanical efficiency at finite temperature. Interestingly, we find the XY device is the least efficient among all. One problem with our XY-tilted ratchet model is that it still interprets ambiguously the detached state which is present only implicitly. To deal with this conceptual problem we consider in the next section a more sophisticated model of the XY-tilted ratchet where we also take into consideration the explicit feedback between the state of the power stroke element and the degree of interaction between the myosin heads and the actin filament.

4.7 XY-Tilted Ratchet with a Steric Feedback

In this section we argue that the conformational state of the power-stroke element can provide steric regulation of the distance between the myosin head and the actin filament. More specifically, we assume that when the lever arm swings, the interaction of the head with the binding site weakens, see Fig. 4.42a. This and other aspects of steric rotation-translation coupling in ratchet models have been previously discussed in [43, 68, 90].

A schematic representation of the proposed model is shown in Fig. 4.42b, where x is the observable position of a myosin head, y is the internal variable characterizing the phase configuration of the power stroke element and z is another internal variable responsible for the coupling. The "macroscopic" variable x sees a symmetric energy landscape and is not directly affected by the ATP hydrolysis. Both asymmetry and driving can then originate only from the coupling between the external and the internal degrees of freedom.

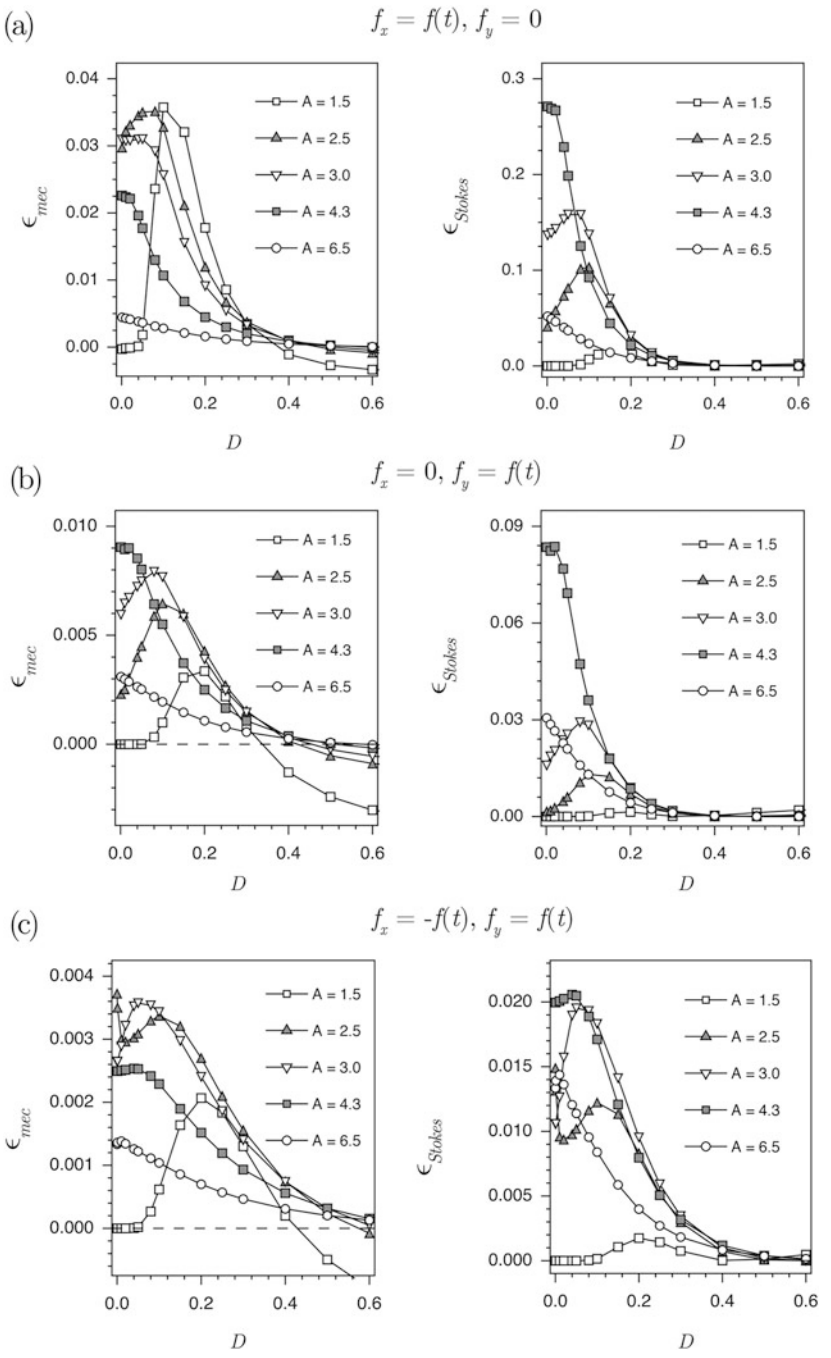

Fig. 4.41 Comparison of the efficiency in the three models loaded in the soft device with $f_{ext} = -0.1$; (**a**) X ratchet. (**b**) Y ratchet. (**c**) XY ratchet. The parameters $k_0 = 1.5$, $k_1 = 0.43$, $l = 0.3$, $L = 1$, $\lambda_1 = 0.7$, $V_{max} = 1.5$, $\alpha = 1, \tau = 30$

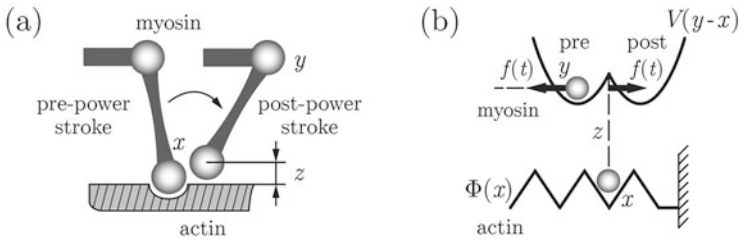

Fig. 4.42 (**a**) An illustration of the steric effect associated with the power-stroke; (**b**) sketch of the mechanical model

4.7.1 The Model

We identify the external degree of freedom with the variable x representing the location of actin binding face on the actin filament. We recall that the natural internal degree of freedom, describing the configurational state of the power-stroke element, is $y - x$, where the variable y was defined in the Introduction. By adding the second internal variable z, characterizing the separation of the myosin head and the actin filament, we attempt to capture the higher-dimensional effects of detachment in the simplest 1D setting.

The role of different variables is clear from the way we write the energy of the system

$$\hat{G}(x, y, z) = z\Phi(x) + V(y - x), \tag{4.26}$$

where $\Phi(x)$ is a non-polar periodic potential representing the binding strength of the actin filament and $V(y - x)$ is a double-well potential describing the power-stroke element. The two-well structure of the potential implies that the power-stroke mechanism can be either folded into the post-power-stroke state or unfolded into the pre-power-stroke state. For simplicity, we assume that the two wells of the potential $V(y - x)$ are symmetric which eliminates a redundant polarity.

The coupling between the state of the power-stroke element $y - x$ and the spatial position of the motor x is implemented through the internal variable z. In the simplest version of the model z is assumed to be a function of the state of the power-stroke element

$$z(x, y) = \Psi(y - x). \tag{4.27}$$

This function must have a particular structure in order to mimic the underlying steric interaction, see Fig. 4.43. We assume that when a myosin head executes the power-stroke it moves away from the actin filament and therefore the control function $\Psi(y - x)$ should progressively switch *off* the actin potential. Similarly, when the power-stroke is recharging the myosin head moves closer to the actin filament and the function $\Psi(y - x)$ should bring the actin potential back into *on* configuration.

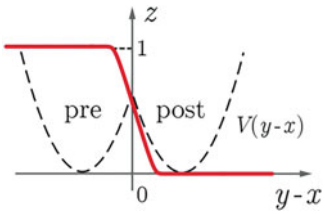

Fig. 4.43 The coupling function $\Psi(y-x)$ linking the degree of attachment z with the state of the power-stroke element $y-x$

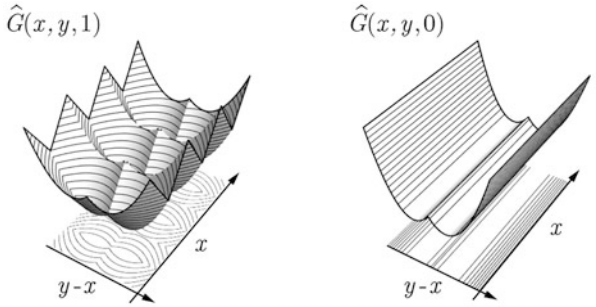

Fig. 4.44 The energy landscapes: $\hat{G}(x, y, 1)$, describing the attached state where $\Psi(y-x)=1$, and $\hat{G}(x, y, 0)$, describing the detached state, where $\Psi(y-x)=0$

We observe that since the double-well potential $V(y-x)$ is fully symmetric, the assignment of the wells to pre- or post-power-stroke states is arbitrary. Had we decided to invert the choice presented in Fig. 4.43 by relabeling the energy wells, we would have to replace $\Psi(s)$ by $\Psi(-s)$. As we see later in the paper, such switch results in a simple reversal of the directionality of the motion.

By using the coupling (4.27) we can simply eliminate the variable z and introduce the redressed potential

$$G(x, y) = \hat{G}(x, y, \Psi(y-x)). \tag{4.28}$$

As it tracks the state of the power-stroke element the potential $G(x, y)$ effectively "flashes" between the periodic and flat (in x) configurations, see Fig. 4.44. However, in contrast to conventional flashing ratchets, the switch here is not imposed from outside but results from the coupling with a fluctuating internal variable.

The overdamped stochastic dynamics of the system with energy (4.28) is described by the following 2D system of (dimensionless) Langevin equations

$$\begin{cases} dx/dt = -\partial_x G(x, y) - f(t) + \sqrt{2D}\xi_x(t), \\ dy/dt = -\partial_y G(x, y) + f(t) + \sqrt{2D}\xi_y(t). \end{cases} \tag{4.29}$$

Here $\xi(t)$ is a conventional white noise with $\langle \xi_i(t) \rangle = 0$, and $\langle \xi_i(t)\xi_j(s) \rangle = \delta_{ij}\delta(t-s)$. The parameter $D = k_B\theta/E$ is a dimensionless measure of temperature θ and k_B is the Boltzmann constant; for simplicity the viscosity coefficients are assumed to be the same for variables x and y. The force couple $f(t)$ with zero average represents a correlated component of the noise and characterizes mechanistically the degree of non-equilibrium in the external reservoir (the abundance of ATP).

We can say that the system (4.29) describes the power-stroke-driven ratchet because the correlated noise $f(t)$ acts on the relative displacement $y - x$. It effectively "rocks" the bi-stable potential and the control function $\Psi(y-x)$ converts such "rocking" into the "flashing" of the periodic potential $\Phi(x)$. Various other types of rocked-pulsated ratchet models have been previously studied in [99, 102].

The goal of any ratchet design is to generate a systematic drift $v = \lim_{t\to\infty}\langle x(t)\rangle/t$ without applying a biasing force. This is possible in the model governed by Eq. (4.29) because of an implicit symmetry breaking imposed by the control function (4.27).

To justify this claim, let us for simplicity set $f(t) = 0$ and rewrite (4.29) in the variables representing the position of the center of mass $q = (x + y)/2$ and the power-stroke configuration $r = y-x$, which is a conventional step in such problems [32]. The new potential is

$$G(q, r) = \Psi(r)\Phi(q - r/2) + V(r),$$

and if we recall that the equilibration of the variable r takes place at much faster time scale than the overall drift, we can adiabatically eliminate it and obtain a one dimensional stochastic system with an effective periodic potential

$$G_{eff}(q) \sim \ln\left[\int_{-\infty}^{\infty} \exp\left(-G(q, r)/D\right)dr\right].$$

In the absence of the feedback $\Psi(s) = 0$ this potential is symmetric $G_{eff}(q) = G_{eff}(-q)$ because $\Phi(s) = \Phi(-s)$ and $V(s) = V(-s)$. When $\Psi(s) \neq \Psi(-s)$, it loses symmetry because pre- and post-power-stroke configurations are no longer equivalent. It is also clear that by reverting the control function $\Psi(s) \to \Psi(-s)$, we change the directionality of the average motion, see Fig. 4.48 below.

To understand the dependence of the average velocity on the parameters of the model, we studied the system (4.29) numerically. In our computational illustrations we use again a periodic extension of the symmetric triangular potential $\Phi(x)$ with amplitude Φ_{max} and period L, see Fig. 4.42a

$$\Phi(x) = \begin{cases} \dfrac{2\Phi_{max}}{L}x \text{ if } 0 \le x < L/2, \\ \dfrac{2\Phi_{max}}{L}(L - x) \text{ if } L/2 \le x < L. \end{cases}$$

The symmetric potential $V(y-x)$ is assumed to be bi-quadratic with the same stiffness k in both phases. The distance between the bottoms of the wells is denoted by a, see Fig. 4.42b, so

$$V(y-x) = \begin{cases} \frac{1}{2}k\,(y-x+a/2)^2 & \text{if } y-x < 0, \\ \frac{1}{2}k\,(y-x-a/2)^2 & \text{if } y-x \geqslant 0. \end{cases}$$

The correlated component of the noise $f(t)$ is again interpreted as the simplest ac driving described by a periodic extension of a rectangular shaped function with amplitude A and period τ

$$f(t) = A(-1)^{n(t)} \quad \text{with} \quad n(t) = \lfloor 2t/\tau \rfloor,$$

where brackets $\lfloor\rfloor$ denote integer part. Finally, the steric control ensuring the gradual switch of the actin potential is described by a gradual step function

$$\Psi(s) = (1/2)\,[1 - \tanh(s/\varepsilon)]\,, \tag{4.30}$$

where ε is a small parameter.

To fix the parametrization, we need to specify the dimensional scales. It is natural to use the distance between the bottoms of the wells in the bi-stable potential as the length scale l so $a = 1$. We have also made a standard assumption that the separation between the binding cites along the actin filament is of the same order as the power-stroke size and therefore $L = 1$. The height of the barrier between the binding sites was chosen as the energy scale E, so we put $\Phi_{max} = 1$. The relaxation time scale was set by the viscosity coefficient η and therefore $\tau^\star = \eta l^2/E$. To ensure that the ac driving is slow at the scale of internal relaxation we took $\tau = 10$. The curvature of the energy wells in the bistable potential should be comparable with E/l^2 and therefore we took a generic value $k = 1.5$. In the computations we used the value of the small parameter $\varepsilon = 0.2$ which made the attachment and the detachment events sufficiently sharp.

To integrate the system (4.29) numerically, we used the simplest Euler–Maryama scheme [63] with a constant time step $\Delta t = 0.5 \times 10^{-3}$. The ensemble averaging was performed over $N = 10^4$ stochastic realizations.

Our numerical results are summarized in Fig. 4.45. First of all, we see that the drift is absent ($v = 0$) when the noise is uncorrelated and the external reservoir is in equilibrium ($A = 0$). This is an obvious consequence of the potential nature of this holonomic model. Indeed, the stationary probability flux satisfies $\nabla J = 0$ and $\mathbf{J} = f\mathbf{F} - D\nabla f$ where $f(x, y)$ is the stationary probability distribution and $\mathbf{F}$ is the internal force. Since $\mathbf{F} = -\nabla G$, one can use periodicity in x and growth in $y - x$ (of the potential G) to show that $\mathbf{J} = 0$, see also [73, 93, 130].

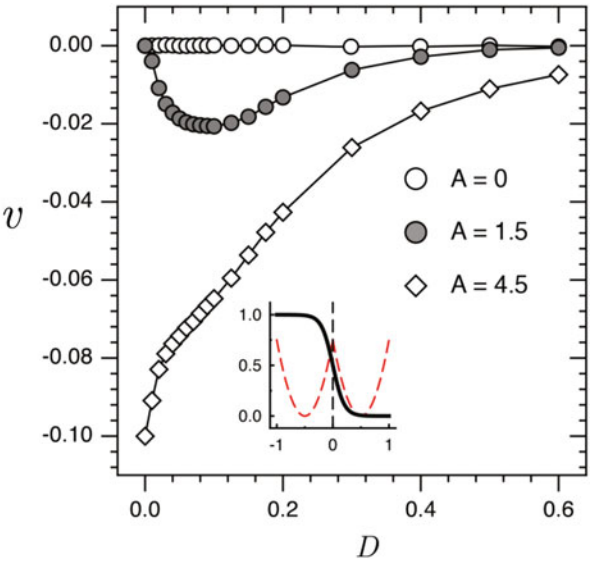

Fig. 4.45 The dependence of the average velocity v on temperature D and the amplitude of the ac signal A in the model with coupling (4.30). The pre- and post-power-stroke states are labeled in such a way that the purely mechanical ratchet would move to the left

It is then clear that the drift in this model is exclusively due to $A \neq 0$. When A is small, the drift velocity shows a maximum at finite temperatures which implies that the system exhibits stochastic resonance [41]. At high amplitudes of the ac driving, the motor works as a purely mechanical ratchet and the increase of temperature always worsens the performance [49, 58, 95].

As we have already seen, the direction of motion in this model is decided by the choice of steric biasing of the otherwise symmetric bi-stable potential. the chosen directionality can be either enhanced or suppressed if we consider polar actin filaments. To illustrate this point, we show in Fig. 4.46 how the drift velocity depends on the parameter characterizing the spatial asymmetry of the actin track. In particular, we see that on a polar filament with sufficient asymmetry our motor can be stopped and even steered in the opposite direction.

The next question concerns the compatibility of the proposed model with the minimal bio-chemical ATPase cycle shown in Fig. 4.1. The traditional identification of chemical and structural states, detailed in this figure, suggests that the motor must pass through the following four mechanical transients: “attached pre-power-stroke”, “attached post-power-stroke”, “detached post-power-stroke” and “detached pre-power-stroke”. It is immediately clear that not all of these states can be reached by the model with coupling (4.30). Indeed, the detachment takes place when the “striking” element is positioned exactly between the two energy wells and therefore the power-stroke cannot be completed in the attached state. As a result, the model reproduces reliably only two structural configurations: the attached pre-power-stroke state and the detached post power-stroke state.

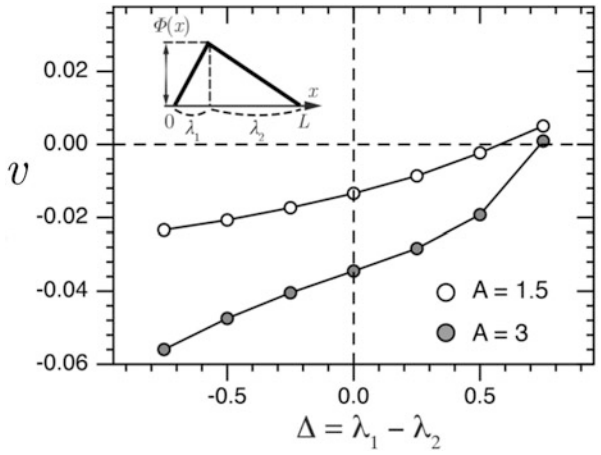

Fig. 4.46 The dependence of the drift velocity v on the filament polarity $\Delta = \lambda_1 - \lambda_2$ in the model with coupling (4.30) at fixed temperature $D = 0.01$

To capture the remaining states shown in Fig. 4.1 we must assume that the detachment, necessarily implying in our model the motion of the center of mass, is delayed till the power-stroke is (almost) completed. Similarly, the attachment must take place only after the power-stroke element has been (almost fully) recharged. The necessary modification of the model, accounting for such two-way delays, is discussed in Sect. 4.7.2.

4.7.2 Hysteretic Coupling

To reproduce the whole Lymn–Taylor cycle, we postulate that the switching of the actin potential from *on* to *off* state takes place at different values of the variable $y-x$, depending on the *direction* of the conformational change (folding or unfolding). To this end, we replace the holonomic coupling (4.27) by a memory operator

$$z\{x, y\} = \widehat{\Psi}\{y(t) - x(t)\} \tag{4.31}$$

whose output depends on whether the system is on the "striking" or on the "recharging" branch of the trajectory, see Fig. 4.47. Such memory structure can be also described by a rate independent differential relation of the form

$$\dot{z} = Q(x, y, z)\dot{x} + R(x, y, z)\dot{y}, \tag{4.32}$$

where the implied non-integrability makes the model non-holonomic. Indeed, if we introduce a vector variable $\mathbf{u} = (x, y, z)$, and neglect the time dependent external

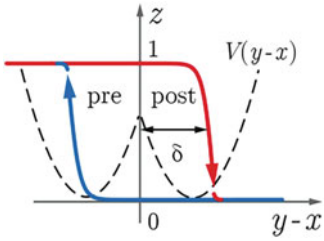

Fig. 4.47 The hysteresis operator $\widehat{\Psi}\{y(t)-x(t)\}$ linking the degree of attachment z with the previous hystory of the power-stroke configuration $y(t)-x(t)$

noise we can rewrite the system of the governing equations in the form $\dot{\mathbf{u}} = \mathbf{F}(\mathbf{u})$, where $\mathbf{F}$ is no longer a gradient. The resulting Brownian motor can potentially advance even in the absence of the correlated noise by extracting energy directly from the non-holonomic control mechanism.

By using (4.31) we can now rewrite the energy of the system as a functional of its history $y(t)$ and $x(t)$

$$G\{x, y\} = \widehat{\Psi}\{y(t) - x(t)\}\Phi(x) + V(y - x). \tag{4.33}$$

In the Langevin setting (4.29), the history dependence may mean that the underlying microscopic stochastic process is non-Markovian (due to, say, configurational pinning [14]), or that there are additional non-thermalized degrees of freedom that are not represented explicitly [50]. In general, it is well known that the realistic feedback implementations always involve delays [36].

To simulate hysteretic response numerically we used two versions of the same coupling function (4.30) shifted by δ with the branches $\Psi(y - x \pm \delta)$ identified sufficiently far away from the hysteresis domain, see Fig. 4.47. Our numerical experiments show that the performance of the model is not sensitive to the shape of the hysteresis loop and depends mostly on its width characterized by the small parameter δ.

In Fig. 4.48 we illustrate the "gait" of the motor with the hysteretic coupling (4.31). The center of mass advances in steps and during each step the power-stroke mechanism gets released and then gets recharged again, which takes place concurrently with attachment-detachment. By coupling the attached state with either pre- or post-power-stroke state, we can vary the directionality of the motion. The average velocity increases with the width of the hysteresis loop which shows that the motor can extract more energy from the coupling mechanism system with longer delays.

The results of the parametric study of the model are summarized in Figs. 4.49 and 4.50. First observe that the motor can move even in the absence of the correlated noise, at $A = 0$, because the non-holonomic coupling (4.33) breaks the detailed balance by itself. At finite A the system can use both sources of energy (hysteretic loop and ac noise) and the resulting behavior is much richer than in the non-hysteretic model.

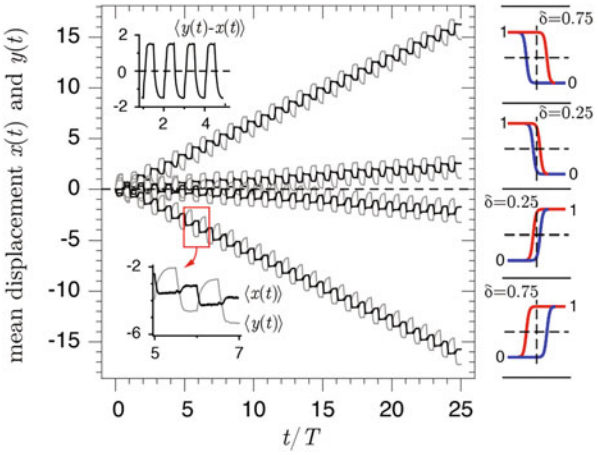

Fig. 4.48 Stationary particle trajectories in the model with the hysteretic coupling (4.31). Different ways of biasing lead to different directions of drift and large hysteresis loops produce faster moving motors. Other parameters are: $D = 0.02$ and $A = 1.5$

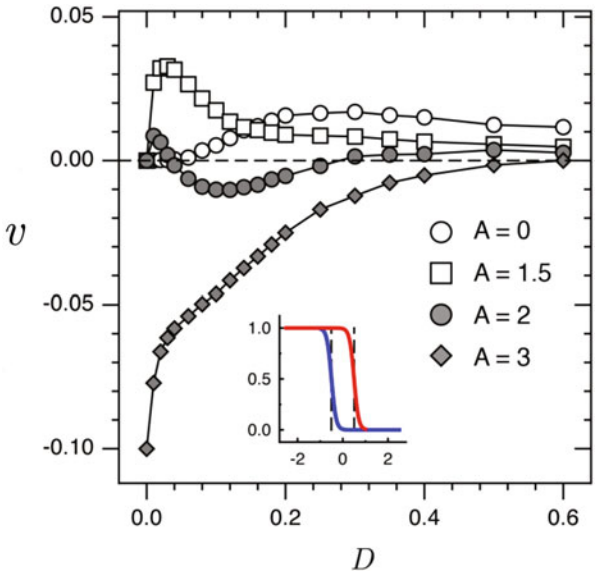

Fig. 4.49 The dependence of the average velocity v on temperature D in the hysteretic model with $\delta = 0.5$

For instance, if the holonomic ratchet with a fixed coupling bias always advances in one direction, the non-holonomic ratchet can self-propell in both directions. At large A the hysteretic motor exhibits the same directionality as the non-hysteretic motor and the average velocity is only mildly affected by the presence of the

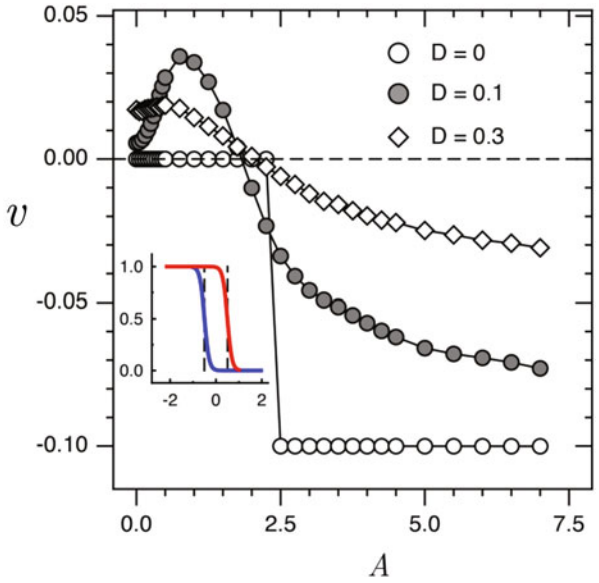

Fig. 4.50 The dependence of the average velocity v on amplitude of the ac driving A in the hysteretic model with $\delta = 0.5$

hysteresis. At small A the situation changes and now the direction of the drift is controlled by the hysteresis and is reversed comparing to the case of a non-hysteretic motor. As we see, in the hysteretic power-stroke-driven ratchet different active mechanisms dominate at different values of A. This opens an interesting possibility for these molecular machines to flip "engines" and in this way reverse the directionality by simply changing the intensity of the external energy supply.

The A dependence of the drift velocity is shown in more detail in Fig. 4.50. At zero temperature the system is pinned and the drift is blocked till the driving amplitude reaches a threshold beyond which the system can work as a mechanical ratchet. At finite temperatures the pinning disappears because of the noise-induced barrier crossing. At small A the motor drifts in the direction opposite to the direction of the mechanical ratchet. The velocity of this drift shows a characteristic peak at finite A revealing stochastic resonance. The current reversal, indicating the change of the mechanism from hysteresis-dominated to correlation-dominated, takes place near the depinning point $A \sim 2.5$.

To illustrate the mechanism of the hysteresis-dominated drift it is sufficient to consider the case when $A = 0$. This disables an alternative ac driven ratchet mechanism. In Fig. 4.51 we compare two realizations of particle trajectories in the 3D space $(x, y - x, z)$: for the model without hysteresis (4.27) and with hysteresis (4.31). The loops obtained by projecting these trajectories on the 2D plane $(y-x, z)$ describe the structure of the corresponding "strokes" in the configurational space. In the holonomic case (4.27) the area of the projected loop is equal to zero and

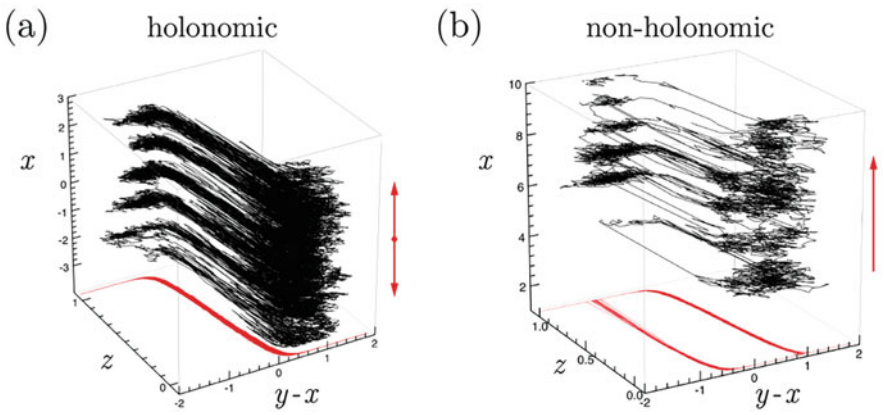

Fig. 4.51 Single particle trajectories in the space $\{y-x, z, x\}$ and their projections on the plane $(y-x, z)$: (**a**) non-hysteretic coupling (**b**) hysteretic coupling. The parameters are: $D = 0.2$, $A = 0$ and $\delta = 0.5$

we observe diffusion without drift (in Fig. 4.51a the average of x is equal to zero). Instead, in the non-holonomic case (4.31) the projected trajectory spans a finite area and the drift velocity is finite (see Fig. 4.51b). Similar dependence of the drift velocity on the area of the "stroke" is known in the theory of Stokes swimmers where non-holonomic control is also the factor responsible for the directional motion (in "violation" of the scallop theorem [4]).

The mechanical "stroke" in the space of internal variables $z, y-x$ can be compared with the minimal biochemical acto-myosin cycle shown in Fig. 4.1. The chemical states constituting this cycle are identified with structural configurations (obtained from crystallographic reconstructions) in the following way [72]: A(attached, pre-power-stroke $\rightarrow$ *AM*ADP*Pi*), B(attached, post-power-stroke $\rightarrow$ *AM*ADP*), C(detached, post-power-stroke $\rightarrow$ *M*ATP*), D(detached, pre-power-stroke $\rightarrow$ *M*ADP*Pi*). In our model the jump events are replaced by continuous transitions and the association of chemical states with particular regimes of stochastic dynamics is not straightforward.

In Fig. 4.52a, we show a fragment of the averaged trajectory of a steadily advancing motor projected on the $(x, y-x)$ plane. In Fig. 4.52b the same trajectory is shown in the $(x, y-x, z)$ space with fast advances in the z direction intentionally schematized as jumps. By using the same letters A, B, C, D as in Fig. 4.1 we establish a basic connection between the chemical/structural states and the transient mechanical configurations of the advancing motor.

Suppose that we start at point A corresponding to the end of the negative cycle of the ac driving $f(t)$. The system is in the attached, pre-power-stroke state and $z = 1$. As the sign of the force $f(t)$ changes, the motor undergoes a power-stroke and reaches point B while remaining in the attached state. When the configurational variable $y - x$ passes the detachment threshold, the myosin head detaches which

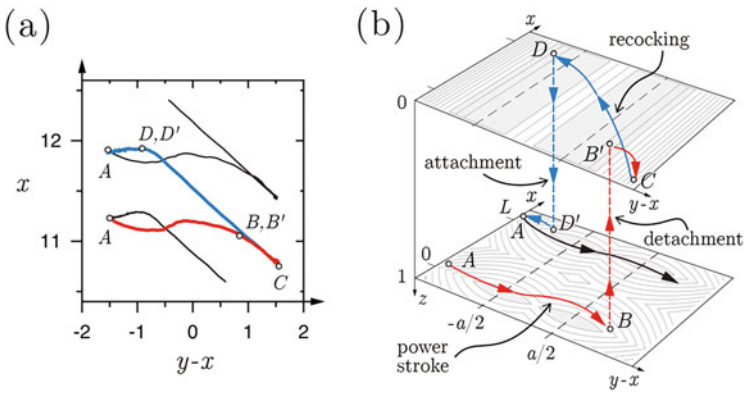

Fig. 4.52 (**a**) A steady-state cycle in the hysteretic model projected on the $x, y - x$ plane; red path if $f(t) > 0$ and blue path if $f(t) < 0$; (**b**) representation of the same cycle in the $z, x, y - x$ space with identification of the four chemical states A, B, C, D constituting the Lymn–Taylor cycle shown in Fig. 4.1. The level sets represent the energy landscape G at $z = 0$ (detached state) and $z = 1$ (attached state). The parameters are: $D = 0.02$, $A = 1.5$, and $\delta = 0.75$

leads to a transition from point B to B' on the plane $z = 0$. Since the positive cycle of the force $f(t)$ continues, the motor completes the power-stroke by moving from B' to point C. At this moment, the rocking force changes sign again which leads to recharging of the power-stroke mechanism in the detached state, described in Fig. 4.1 as a transition from C to D. In point D, the variable $y - x$ reaches the attachment threshold. The myosin head reattaches and the system moves to point D' where $z = 1$ again. The recharging continues in the attached state as the motor evolves from D' to a new state A, shifted by one period.

In this way the chemical states constituting the minimal enzyme cycle can be linked to the mechanical configurations traversed by our stochastic dynamical system. The detailed mechanical picture, however, looks more complicated than in the simplest Lymn–Taylor scheme. It is clear that at least in some regimes one can use the Kramers approximation to perform a controlled transition from our continuous dynamics to a description in terms of a discrete set of chemical reactions. However, it is also clear that more chemical states than in the minimal Lymn–Taylor model will be needed to describe the detailed mechanical "stroke".

So far we have been dealing with motors overcoming viscous friction but not carrying cargoes. The next step is to see how fast the same motor can move against an external force f_{ext}. Two different mechanical configurations of the motor carrying cargo correspond to the cases when $f_{ext} > 0, v < 0$ and $f_{ext} < 0, v > 0$, see Fig. 4.53. Since the non-hysteretic motor is designed to move to the left, the mechanical configuration shown in Fig. 4.53a can be somewhat arbitrarily characterized as "pushing". Given that the motor with the hysteretic coupling can move in both directions, the configuration shown in Fig. 4.53b also corresponds to a steady regime which can be then interpreted as "pulling". Since our motor does not have explicit leading and trailing edges, we assume that the force f_{ext} acts in both

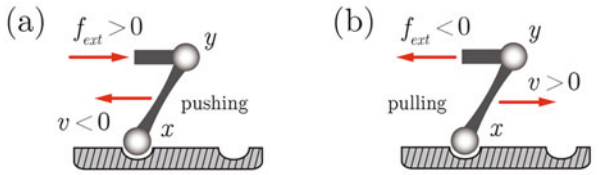

Fig. 4.53 Schematic representation of the power stroke driven motor carrying cargo: (**a**) pushing regime, (**b**) pulling regime

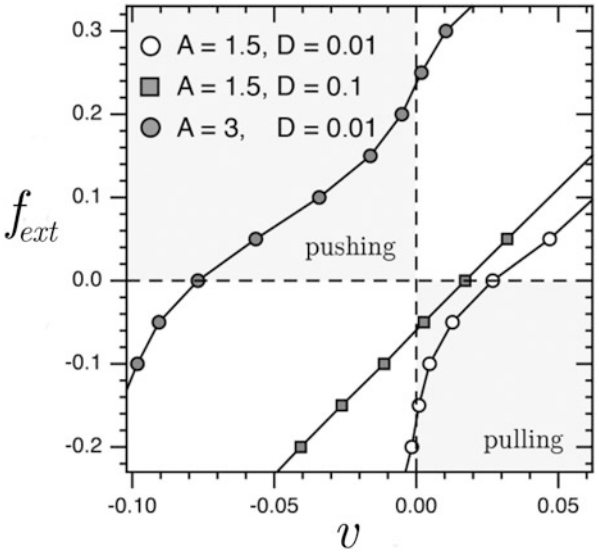

Fig. 4.54 The force-velocity relation in the model with hysteretic coupling at different amplitudes of the ac driving A and different temperatures D. The hysteresis width is $\delta = 0.5$

cases on the variable y which amounts to tilting of the potential (4.33) along the y direction

$$G\{x, y\} = \widehat{\Psi}\{y(t) - x(t)\}\Phi(x) + V(y - x) - yf_{ext}. \tag{4.34}$$

However, the actual architecture of a half sarcomere is asymmetric and the forces are transmitted through passive cross-linkers imposing a particular polarity on the loading. Therefore, despite the ambiguity, we find the association of the two mechanical regimes shown in Fig. 4.53 with pushing and pulling appropriate.

A stochastic system with energy (4.34) was studied numerically and in Fig. 4.54 we show the computed force-velocity relations. The light quadrants in the (f_{ext}, v) plane correspond to two domains of dissipative behavior where $R = f_{ext}v > 0$. Here the direction of the force agrees with the direction of motion and the motor is being dragged by the applied load (while exhibiting both passive and active friction).

The shaded quadrants indicate the two domains where the system is anti-dissipative and $R = f_{ext} v < 0$. In these regimes the motor produces work and the motion can be of two types: when the motor overcomes the opposing pushing force and drives the cargo ahead of itself ($f_{ext} > 0$, $v < 0$) and when it carries the cargo attached from behind acting against a pulling force ($f_{ext} < 0$, $v > 0$). Since in the hysteretic model the current can be reversed by changing the amplitude of the ac noise A, our motor can perform two types of useful work.

Observe that at low temperatures the convexity properties of the force-velocity relations in active pushing and active pulling regimes are different. In the case of pulling the typical force-velocity relation is reminiscent of the Hill's curve describing isotonic contractions [51]. In the case of pushing, the force-velocity relation can be characterized as convex-concave and such behavior has been also observed in muscles [30, 31, 71]. The difference is due to the dominance of physically non-equivalent mechanisms in the corresponding parameter domains.

For instance, in the pushing regimes, the motor activity fully depends on ac driving and at large amplitudes of this driving it performs as a mechanical ratchet. Instead, in the pulling regimes, associated with small amplitudes of external driving, the motor advances because of the delayed feedback exemplified by the hysteretic mechanism. We may speculate that both mechanisms can be operative in acto-myosin systems which would then provide an explanation for occasionally counterintuitive drift directions.

We also mention that dissimilarity of convexity properties of the force-velocity relations in pushing and pulling regimes has been recently discussed in the context of cell motility where acto-myosin contractility is known to be one of the main driving forces [94]. The direct quantitative comparison is, however, premature since in our minimal setting the model deals with a single cross bridge and still neglects important collective effects [19].

4.7.3 Non-potential Models

The performance of the power-stroke driven ratchet can be considerably enhanced if the feedback between the power-stroke and the attachment-detachment mechanisms is made non-conservative even in the absence of hysteresis. This would happen, for instance, if the configurational state of the power-stroke element affected the position of a myosin head with respect to actin filament, while the reverse influence remained insignificant, in other words, if the coupling between the power-stroke element and the actin potential was one-sided. In this case instead of a passive control we are dealing with an *active control* represented by a Maxwell demon-type mechanism [18, 35].

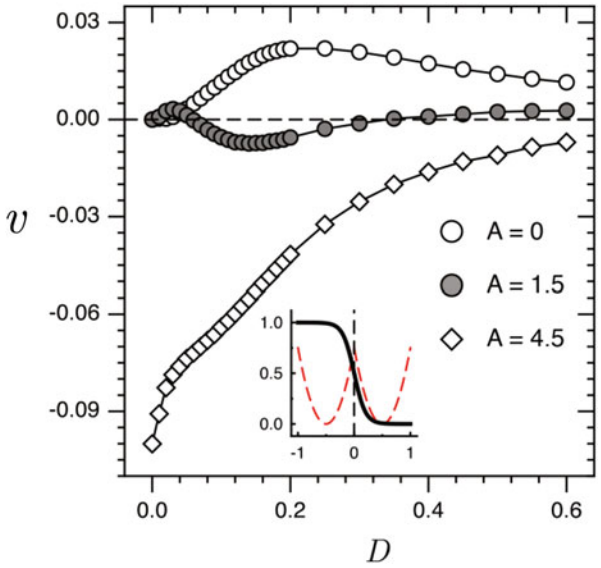

Fig. 4.55 Temperature dependence of the drift velocity v in the non-potential model (4.35) without hysteresis

The governing equations describing such ratchet can be written in the form

$$\begin{cases} dx/dt = -z\partial_x \Phi(x) - \partial_x V(y-x) - f(t) + \sqrt{2D}\xi_x(t) \\ dy/dt = -\partial_y V(y-x) + f(t) + \sqrt{2D}\xi_y(t), \end{cases} \tag{4.35}$$

where the notations are the same as in (4.29). The results of the numerical study of the system (4.35) are summarized in Fig. 4.55.

The overall behavior of the non-potential system (4.35) is similar to the behavior of the potential system with hysteretic coupling (4.33). Since the ratchet can now receive energy from the active controlling device [73, 93], a nonzero drift takes place already at $A = 0$. The direction of the current can be again reversed by varying the amplitude of the driving. At large values of A, we obtain our usual mechanical ratchet which does not see the non-potentiality of the model. At small A the ratchet exploits the non-potentiality of the model in the essential way. As in the case of hysteretic system, the direction of the drift is now opposite to the one picked up by the mechanical ratchet. Notice also that at moderate values of A the directionality of the drift can be reversed by the variation of temperature.

The non-potential ratchet shows the highest performance in combination with the hysteretic feedback (4.33), see Fig. 4.56. The behavior of such hybrid system at $A = 0$ is similar to what we have seen in the case of the system with energy (4.33) which means that in this regime the response is dominated by hysteresis. As A increases we observe a new effect: around $A \sim 1.5$ the system appear to be in

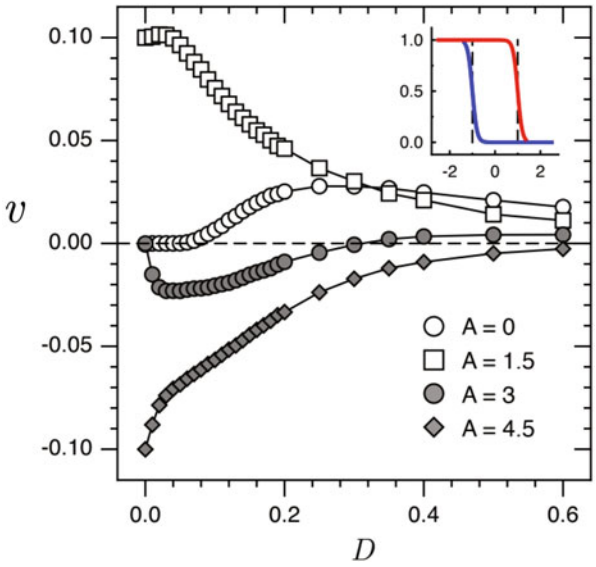

Fig. 4.56 Temperature dependence of the drift velocity v in the non-potential model (4.35) with hysteresis, $\delta = 1$

a resonant state and works as a quasi-mechanical ratchet, however now, the non-potentiality is the principle driving factor, see Fig. 4.56. With further increase of A we observe a reversal of the current and the system enters the regime where the main driving force is again the ac noise. At large A the mechanical ratchet behavior prevails again, however, it is fundamentally different from the quasi-mechanical ratchet behavior observed around $A \sim 1.5$.

In Fig. 4.57 we illustrate the effect of the amplitude A on the drift velocity in more detail. In contrast to the potential case, the ratchet can now move at zero temperatures in both directions equally fast if the amplitude of the ac signal is chosen appropriately. The current reversal takes place in the narrow range of amplitudes A where the transition from a mechanical to a quasi-mechanical ratchet mechanism takes place.

At finite temperatures we see a complex interplay of all three active mechanisms. The detailed study of the underlying stochastic system, allowing one to precisely map the parametric domains where particular mechanisms dominate, will be presented elsewhere.

To better understand the effects of non-potentiality we also compute the Péclet number $Pe = Lv/D_e$, characterizing the relative strength of the drift (over diffusion). The effective diffusion coefficient is defined by Reimann et al. [97], Lindner et al. [70], and Khoury et al. [61]

$$D_e = \frac{1}{2} \lim_{t \to \infty} \frac{\langle [x(t) - \langle x(t) \rangle]^2 \rangle}{t}, \tag{4.36}$$

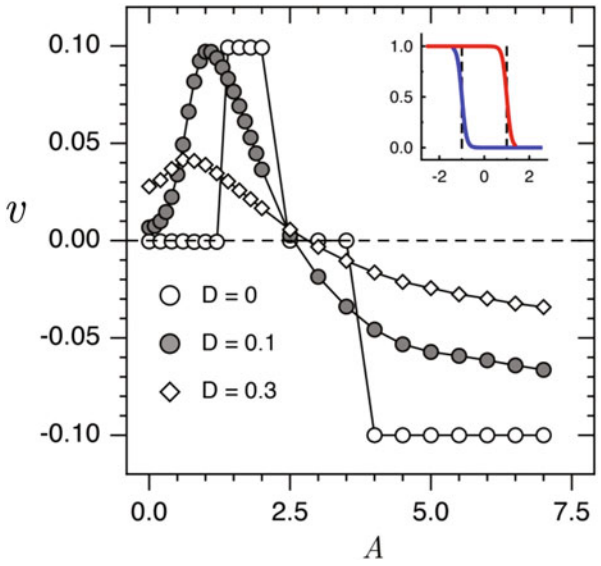

Fig. 4.57 The dependence of the average velocity v on the amplitude A of the ac signal in the non-potential model with hysteresis, $\delta = 1$

so the stochastic transport is most coherent when the absolute value of the Péclet number is larger than one. From Fig. 4.58 we see that only in the non-potential model the motion at small values of the driving amplitude A can be viewed as truly directional.

Suppose now that a load is attached to the motor with non-potential hysteretic coupling. The typical force-velocity relations are shown in Fig. 4.59. As in the potential case, the motor can operate in two anti-dissipative regimes either by working against a pushing force or by pulling a cargo. At both small and large values of A the behavior of the potential and the non potential motors is similar. Expectedly, an anomaly takes place in the pulling regime ($f_{ext} < 0, v > 0$) at $A \sim 1.5$ where the motor behaves as a quasi-mechanical ratchet. Here the non-potentiality dominates and the force-velocity relation shows an unusually sharp convexity change. It is interesting that in this regime the behavior near the stall force is reminiscent of the one observed in skeletal muscles [53].

4.8 Active Rigidity

In this section we show that effective rigidity or, more generally, effective susceptibility in a bundle of elastically coupled cross-bridges, can emerge from the activity localized at the level of the power stroke machinery. Consider again a skeletal muscle cell [53] where we neglect detachment of active cross-linkers (cross-

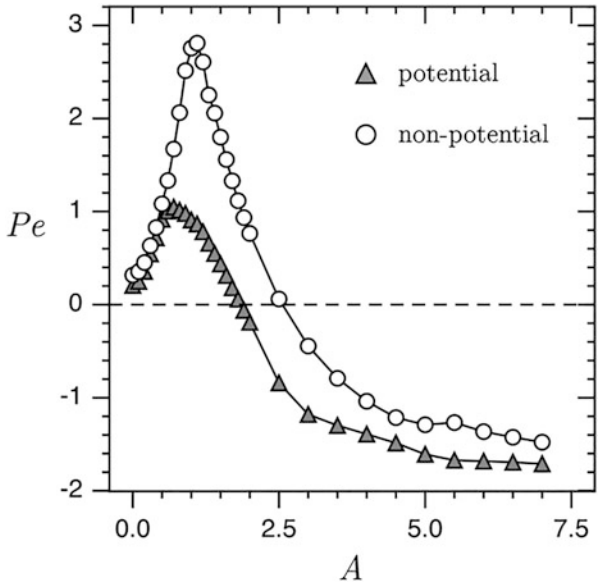

Fig. 4.58 The Péclet number in the potential model with hysteresis ($\delta = 0.5$ as in Fig. 4.50) and in the non-potential model with hysteresis ($\delta = 1$ as in Fig. 4.57); $D = 0.1$

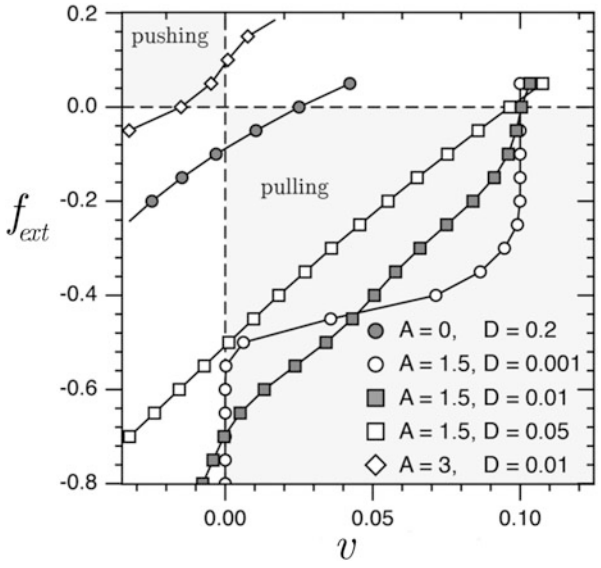

Fig. 4.59 The force-velocity relation in the non-potential model with hysteresis at different temperatures D and different driving amplitudes A; $\delta = 1$

bridges) and model an elementary series element (half-sarcomere) as a parallel array of molecular motors operating in stall conditions. As in other sections, we model attached myosin motors as bi-stable springs, with two energy wells corresponding to pre and post power stroke configurations. Each 'snap-spring' of this kind acts against a linear spring, representing a structural filament. The system is exposed to both uncorrelated agitation (scaled with temperature-type parameter D) and a correlated noise representing ATP hydrolysis (scaled with affinity-type parameter A).

4.8.1 Macroscopic Problem

We start with an assumption that a muscle myofbril can be viewed as a chain of half-sarcomeres arranged in series with each half-sarcomere represented by a parallel array of N cross-bridges interacting with a single actin filament [54, 120], see Fig. 4.60. We assume again that the nontrivial dynamics of attached cross-bridges is due exclusively to the conformational change in myosin heads (power stroke) and model cross-bridges as bi-stable elements in series with linear springs, see Fig. 4.61. We therefore stay with our original paradigm that the nonequilibrium driving is provided through the rocking of the bi-stable elements [108].

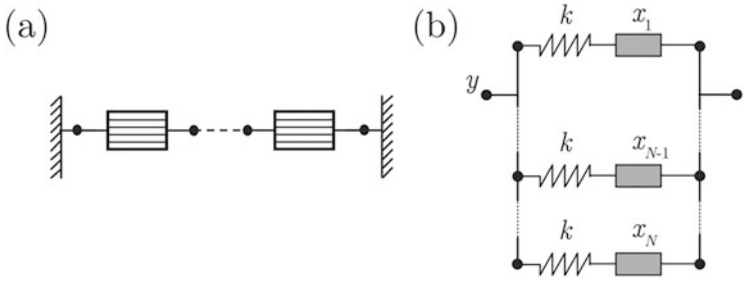

Fig. 4.60 (**a**) Schematic representation of a muscle myofibril as a series connection of half sarcomeres; (**b**) Model of a single half-sarcomere with attached cross-bridges arranged in parallel. Shaded boxes in (**b**) represent bi-stable snap-springs shown in Fig. 4.61

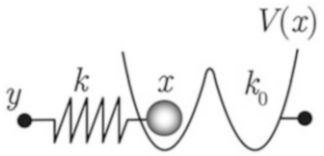

Fig. 4.61 Schematic representation of a bi-stable snap-spring in series with a linear spring

A half-sarcomere in this model, see Fig. 4.60b, can be described by the system of non-dimensional Langevin equations

$$\begin{cases} dx_i/dt = -\nabla_{x_i}\Phi + \sqrt{2D}\xi(t), \\ \nu dy/dt = -\nabla_y \Phi, \end{cases} \tag{4.37}$$

where y is a macro-scopic variable characterizing the strain at the level of the half-sarcomere whose dynamics is slow due to the large value of the relative viscosity ν. The variable y is coupled with N fast soft-spin type variables x_i through identical springs with stiffness k. The potential energy is $\Phi = \sum_{i=1}^{N} E(x_i, y, t) - f_{\text{ext}} y$, where $f_{\text{ext}}(t)$ is a slowly varying macro-scopic force. The ensuing problem is a soft spin generalization [76] of the Huxley-Simmons model [54] and we recall that its applications extend far beyond muscles mechanics, from hair cell gating [77] and binding of cell-adhesion patches [33] to mechanical denaturation of RNA and DNA hairpins [128] and unzipping of biological macromolecules [47].

The equation for y in (4.37) can be re-written as

$$\frac{\nu}{N}\frac{dy}{dt} = k\left(\frac{1}{N}\sum_{i=1}^{N} x_i - y\right) + \frac{f_{\text{ext}}}{N}, \tag{4.38}$$

which makes the mean field nature of the interaction between y and x_i explicit. If N is large, we can replace $\frac{1}{N}\sum_{i=1}^{N} x_i$ by $\langle x\rangle$ using the fact that the variables x_i are identically distributed and exchangeable [34]. If $\nu_0 = \nu/N$ and $g_{\text{ext}} = f_{\text{ext}}/(kN)$ remain finite in the limit $N \to \infty$, we can write

$$\nu_0 dy/dt = k[(\langle x\rangle - y) + g_{\text{ext}}(t)].$$

Assume for determinacy that the function $f(t)$ is periodic and choose its period τ in such a way that $\Gamma = \nu_0/k \gg \tau$. Since $g_{\text{ext}}(t)$ is a slowly varying function at the time scale τ, we can split the force $k(\langle x\rangle - y)$ acting on y into a slow component $k\psi(y) = k(\overline{\langle x\rangle} - y)$ which originates from our effective potential and a slow-fast component $k\phi(y,t) = k(\langle x\rangle - \overline{\langle x\rangle})$ which in the steady regime becomes a τ periodic function of time with zero average. We can then write

$$\Gamma\frac{dy}{dt} = \psi(y) + \phi(y,t) + g_{\text{ext}}. \tag{4.39}$$

The next step is to average (4.39) over the time scale τ. To this end we introduce a decomposition $y(t) = z(t) + \zeta(t)$, where z is the averaged (slow) part of the motion and ζ is a fast varying perturbation (with time scale τ) that is small compared to z. Then, expanding 4.39 up to first order in ζ, we obtain,

$$\begin{aligned} \Gamma\left(\frac{dz}{dt} + \frac{d\zeta}{dt}\right) = \psi(z) + \partial_z\psi(z)\zeta + \\ \phi(z,t) + \partial_z\phi(z,t)\zeta + g_{\text{ext}}. \end{aligned} \tag{4.40}$$

Since $g_{\text{ext}}(t) \simeq \tau^{-1} \int_t^{t+\tau} g_{\text{ext}}(u)du$, we obtain at fast time scale [13]

$$\Gamma \frac{d\zeta}{dt} = \phi(z, t).$$

Integrating this equation between t_0 and $t \leq t_0 + \tau$ we can assume that z is fixed and therefore $\zeta(t) - \zeta(t_0) = \Gamma^{-1} \int_{t_0}^{t} \phi(z(t_0), u)du$. Given that ϕ is τ periodic with zero average, we conclude that $\zeta(t)$ is also τ periodic with zero average.

If we now average (4.40) over the fast time scale τ, we obtain

$$\Gamma dz/dt = \psi(z) + r + g_{\text{ext}},$$

where

$$r = (\Gamma\tau)^{-1} \int_0^{\tau} \int_0^{t} \partial_z \phi(z, t)\phi(z, u)dudt.$$

Since both $\phi(z, t)$ and $\partial_z \phi(z, t)$ are bounded, we can write $|r| \leq (\tau/\Gamma)c \ll 1$, where the 'constant' c depends on z but not on τ and Γ. Therefore, if $N \gg 1$ and $\nu/(kN) \gg \tau$, the equation for

$$z(t) = \tau^{-1} \int_t^{t+\tau} y(u)du$$

can be written directly in terms of the effective potential

$$(\nu/N)dz/dt = -\partial_z F + f_{\text{ext}}/N.$$

To find the potential $F(z)$ we need to average the ensuing mean field model over the fast and slow-fast dynamics in (4.41) while keeping the variable y fixed.

4.8.2 Mean Field Model

The implied mean field model can be viewed as a description of a probe characterized by a (microscopic) coordinate x which is placed in an active environment. The probe is attached through an elastic spring to a measuring device associated with a (meso-scopic) variable y. We assume that the variable y is slow and treat it as a control parameter. Instead, the variable $x(t)$ will undergo fast stochastic motion which will have to be averaged out.

In the absence of noise, the environment will be introduced through the potential $V(x)$ and we assume that the probe is placed in an unstable configuration. One way to satisfy this condition is to assume that $V(x)$ has a double well structure with the reference position of a probe in a spinodal state. We further assume

that the probe is exposed to a fluctuating surrounding medium with a quickly relaxing component represented by an equilibrium thermostat and a relatively slower relaxing component describing non-equilibrium environment. We study the meso-scopic force exerted by the probe on the measuring device which implies the transition from the environment potential $V(x)$ to the effective potential for the measuring device $F(y)$.

To be more specific, consider the stochastic dynamics of a variable $x(t)$ described by a dimensionless Langevin equation

$$dx/dt = -\partial_x E(x, y, t) + \sqrt{2D}\xi(t), \tag{4.41}$$

where $\xi(t)$ is a standard white noise and D is a temperature-like characteristic of the equilibrium thermostat. The potential $E(x, y, t) = E_{\rm p}(x, t) + E_{\rm m}(x, y)$ is sum of two components: $E_{\rm p}(x, t) = V(x) - xf(t)$, describing the probe in an out of equilibrium environment and $E_{\rm m}(x, y) = k(x - y)^2/2$, describing the linear elastic coupling with a measuring device characterized by stiffness k. We assume that the energy is supplied to the system through the rocking force $f(t)$ with zero average which is characterized by an amplitude A and a time scale τ. To have analytical results, we need to further assume that the potential $V(x)$ is bi-quadratic

$$V(x) = (|x| - 1/2)^2/2. \tag{4.42}$$

Similar framework has been used before in the studies of directional motion of molecular motors [25].

To compute the effective potential $F(y)$ we use an observation that if the 'measurements' are performed at a time scale larger that τ, the resulting force is $T(y) = k[y - \overline{\langle x \rangle}]$, where the averaging is over ensemble and time

$$\overline{\langle x \rangle} = \lim_{t\to\infty} (1/t) \int_0^t \int_{-\infty}^{\infty} xp(x, t)dxdt.$$

Here $p(x, t)$ is the probability distribution for the variable x which solves the associated Fokker–Plank equation. The primitive of the averaged tension

$$F(y) = \int^y T(s)ds, \tag{4.43}$$

can be then viewed as a non-equilibrium analog of the free energy [6, 66, 100, 129]. While in our case, the mean-field nature of the model ensures potentiality of the averaged tension, in a more general setting, the averaged stochastic forces will lose their gradient structure and even the effective "equations of states" relating averaged forces with the corresponding generalized coordinates may not be well defined [9, 12, 44, 56, 110, 114].

It is clear that the effective potential $F(y)$ will depend not only on $V(x)$ but also on the stochastic properties of the driving $f(t)$. The question we pose is

whether there exists a non-biased stochastic driving which ensures stabilization of spinodal configurations that would be unstable in the absence of the noise. In the equilibrium case, when $f(t) = 0$, such stabilization is possible because of entropic effects but only at sufficiently large temperature D. The challenge is to find a correlated (colored) noise $f(t)$ which ensures stabilization at arbitrary small D. The possibility of bi-modality of the marginal probability distribution $p(x,t)$ in single-well potentials is known for DC and Levi type noises [28, 29], however, this effects disappears after ensemble averaging involved in the computation of the effective potential $F(y)$.

4.8.3 Non-dimensionalization

Equation (4.41), which constitutes the basis of our prototypical model, is dimensionless. To translate the results back into muscles context we need to use the time scale $\tau^\star = \eta/k_0 \sim 0.1$ ms where $\eta \sim 0.38$ ms. pN/nm is the micro-scale viscosity [19] and $k_0 \sim 3$ pN/nm is the passive stiffness of the equivalent energy wells. The spatial scale is then $l^\star = a$ where $a \sim 10$ nm is the distance between two minima of the pre and post power stroke wells [69] and the energy scale is $\epsilon^\star = k_0 a^2 \sim 300\,\text{pN} \cdot \text{nm}$.

Following [19] we also assume that $k = k_m/k_0 \sim 0.6$, where $k_m \sim 2\,\text{pN/nm}$ is the stiffness of the elastic part of the myosin motor [7, 67]. Hence $D = k_B\Theta/(k_0 a^2) \sim 0.01$ where $k_B = 4.10\,\text{pN} \cdot \text{nm}$ is the Boltzmann constant, $\Theta \sim 300\,\text{K}$ is the ambient temperature, and $a = 10nm$ is the characteristic size of a motor power-stroke [69]. For the active driving we obtain $\tau = \tau_a/(\eta/k_0) \sim 100$ where $\tau_a = 40$ ms is the characteristic time of ATP hydrolysis [53]. We can now write that $A = \sqrt{\Delta\mu/(k_0 a^2)} \approx 0.5$ where $\Delta\mu = 20 k_B\Theta$ is the typical value of degree of non-equilibrium in terms of the affinity of ATP hydrolysis reaction [53].

The knowledge of the set of dimensionless parameters A, D and τ will be sufficient to locate the muscle system on the phase (regime) diagram. Such diagrams will be constructed in Sect. 4.8.4 for three different types of active driving.

4.8.4 Phase Diagrams

In this Section we consider the general problem (4.41) at finite temperature ($D > 0$) when both equilibrium and nonequilibrium reservoirs are contributing to the microscopic dynamics simultaneously. The limiting case of zero temperatures ($D = 0$) will be analyzed separately in Sec. 4.8.5.

Periodic (P) Driving Suppose first that the non-equilibrium driving is represented by a periodic (P), square shaped external force $f(t) = A(-1)^{n(t)}$ with $n(t) = \lfloor 2t/\tau \rfloor$, where brackets denote the integer part. While this choice of periodic driving ensures certain analytical simplicity, the obtained results will be generic.

It will be convenient to rewrite the dynamic equation (4.41) in the form

$$dx/dt = -\partial_x \tilde{V}(x,z) + f(t) + \sqrt{2D}\xi(t), \tag{4.44}$$

where

$$\tilde{V}(x,z) = \frac{1}{2}\left(|x| - 1/2\right)^2 + \frac{1}{2}k(x-z)^2.$$

The associated Fokker–Planck equation for the time dependent probability distribution $p(x,t)$ reads

$$\partial_t p = \partial_x \left[p\partial_x E(x,t) + D\partial_x p\right]. \tag{4.45}$$

First of all we note that explicit solution of (4.45) can be found in the adiabatic case when the correlation time τ is much larger than the escape time for the bistable potential V [48, 74]. The idea of this approximation is that the time average of the steady state probability can be computed from the mean of the stationary probabilities with constant driving force (either $f(t) = A$ or $f(t) = -A$).

It is obvious, that the adiabatic approximation becomes exact in the special case of an equilibrium system with $A = 0$ when the stationary probability distribution is known explicitly:

$$p_0(x) = Z^{-1} e^{-\tilde{V}(x)/D},$$

where $Z = \int_{-\infty}^{\infty} \exp(-\tilde{V}(x)/D)dx$. The tension elongation curve can then be computed analytically, since we know

$$\overline{\langle x \rangle} = \langle x \rangle = \int_{-\infty}^{\infty} x p_0(x) dx. \tag{4.46}$$

The resulting curve $T(z)$ and the corresponding potential $F(z)$ are shown in Fig. 4.62a. At zero temperature the equilibrium system with $A = 0$ exhibits negative stiffness at $z = 0$ where the effective potential $F(z)$ has a maximum (spinodal state). As temperature increases we observe a standard entropic stabilization of the configuration $z = 0$, see Fig. 4.62a.

Computing solution of the equation $\partial_z T|_{z=0} = 0$, we find an explicit expression for the critical temperature $D_e = r/[8(1+k)]$ where r is a root of a transcendental equation $1 + \sqrt{r/\pi}\mathrm{e}^{-1/r}/[1 + \mathrm{erf}(1/\sqrt{r})] = r/(2k)$. The behavior of the roots of the equation $T(z) = -k(\overline{\langle x \rangle} - z) = 0$ at $A = 0$ is shown in Fig. 4.63b. It illustrates a second order phase transitions taking place at $D = D_e$.

In the case of constant force $f \equiv A$ the stationary probability distribution is also known [98]

$$p_A(x) = Z^{-1} e^{-\left(\tilde{V}(x) - Ax\right)/D},$$

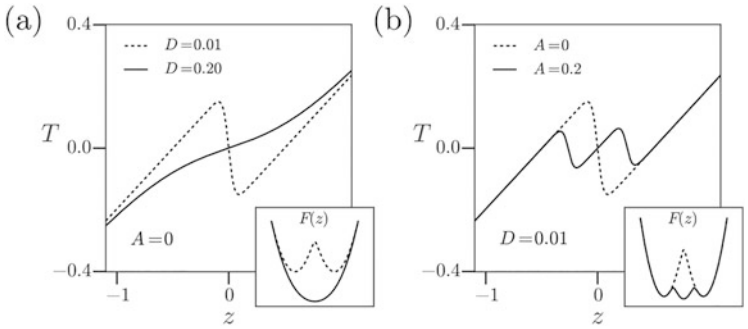

Fig. 4.62 Tension elongation curves $T(z)$ in the case of periodic driving (adiabatic limit). The equilibrium system ($A = 0$) is shown in (**a**) and out-of-equilibrium system ($A \neq 0$)—in (**b**). The insets show the effective potential $F(z)$. Here $k = 0.6$

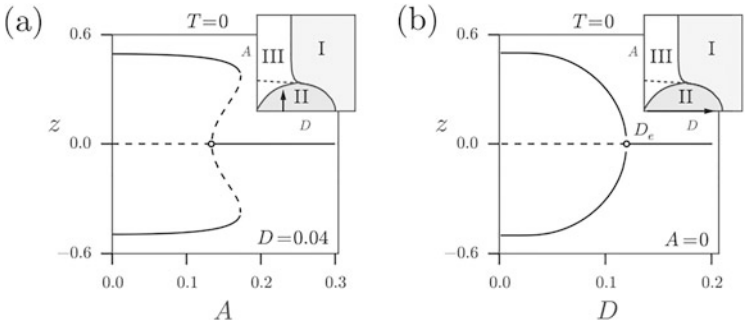

Fig. 4.63 The parameter dependence of the roots of the equation $T(z) = 0$ in the adiabatic limit: (**a**) fixed $D = 0.04$ and varying A, first order phase transition (line $C_A - M_A$ in Fig. 4.64a); (**b**) fixed $A = 0$ and varying D, second order phase transition (line $D_e - C_A$ in Fig. 4.64a). The dashed lines correspond to unstable branches. Here $k = 0.6$

where again $Z = \int_{-\infty}^{\infty} \exp(-\tilde{V}(x)/D)dx$. In adiabatic approximation we can write the time averaged stationary distribution in the form, $p_{\mathrm{Ad}}(x) = \frac{1}{2}[p_A(x) + p_{-A}(x)]$, which gives

$$\overline{\langle x \rangle} = \frac{1}{2}\left[\langle x \rangle(A) + \langle x \rangle(-A)\right]. \tag{4.47}$$

In this equation the expression for $\langle x \rangle(A)$ can be written explicitly

$$\langle x \rangle(A) = Z^{-1} \sum_{i=1,2} P(u_i)[\sqrt{\pi} u_i \mathrm{erfc}(u_i) - (-1)^i e^{-u_i^2}],$$

where

$$P(u) = (D/(1+k))\mathrm{e}^{-\frac{1}{2D}\left(\frac{1}{4}+kz^2-2Du^2\right)},$$

$$u_{1,2} = (A \pm 1/2 + kz)/\sqrt{2D(1+k)},$$

$$Z = \sqrt{(1+k)\pi/(2D)} \sum_{i=1,2} P(u_i)\mathrm{erfc}((-1)^i u_i),$$

and erfc is the complementary error function.

The force-elongation curves $T(z)$ and the corresponding potentials $F(z)$ obtained for $A \neq 0$ are shown in Fig. 4.62b. It demonstrates the main effect: as the degree of non-equilibrium, characterized by A, increases, not only the stiffness in the state $z = 0$ where the original double well potential V had a maximum changes from negative to positive but also the effective potential $F(z)$ develops around this point the third well. We interpret this phenomenon as the emergence of active rigidity because the new equilibrium state becomes possible only at a finite value of the driving parameter A while the temperature parameter D can be arbitrarily small. The behavior of the roots of the equation $T(z) = -k(\overline{\langle x \rangle} - z) = 0$ at $A \neq 0$ is shown in Fig. 4.63a. It illustrates the first order phase transitions taking place at increasing A (and small fixed D).

The full steady state regime map (dynamic phase diagram) summarizing the results obtained in adiabatic approximation is presented in Fig. 4.64a. There, the 'paramagnetic' phase I describes the regimes where the effective potential $F(z)$ is convex, the 'ferromagnetic' phase II is a bi-stability domain where the potential $F(z)$ has a double well structure and, finally, the 'Kapitza' phase III is where the function $F(z)$ has three convex sections separated by two concave (spinodal) regions. Note that the boundaries of the domain occupied by phase III in this diagram are not defined by the number of the roots of $T(z) = 0$, as it is usually done

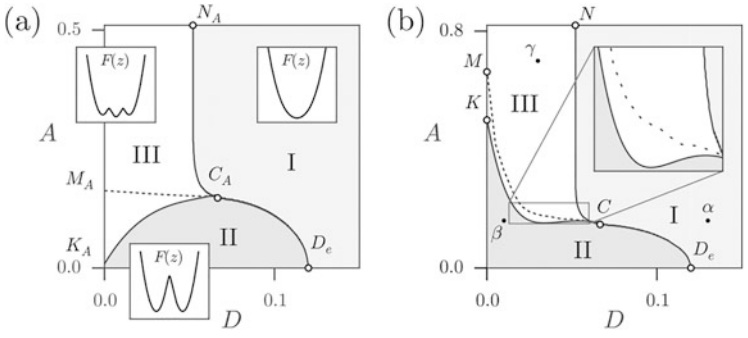

Fig. 4.64 Phase diagram in (A, D) plane showing phases I,II and III: (**a**) adiabatic limit, (**b**) numerical solution at $\tau = 100$ (**b**). C_A is the tri-critical point, D_e is the point of a second order phase transition in the passive system. The "Maxwell line" for a first order phase transition in the active system is shown by dots. Here $k = 0.6$

in the study of magnetic systems, but by the counting of the number of the effective "energy wells" linked to convexity properties of the whole effective potential $F(z)$.

In view of the structure of the bifurcation diagrams shown in Fig. 4.63, we can interpret the boundary $C_A - D_e$ separating phases I and II as a line of (zero force) second order phase transitions and the dashed line $C_A - M_A$ as a Maxwell line for the (zero force) first order phase transition, see Fig. 4.63. Then C_A can be interpreted as a tri-critical point near which the system can be described by an non-equilibrium (active) Landau potential of the form

$$F(z) = F_0 + rz^2 + qz^4 + pz^6,$$

where r, q, p are pseudo-thermodynamic parameters. Indeed, while r represents the usual measure of temperature D and $p > 0$ is a constant, the A dependent parameter q is an uncoventional measure of the intensity of active driving. Similar tri-critical point appears in the periodically driven mean field Suzuki-Kubo model of magnetism which can be interpreted in our terms as a description of the zero tension behavior [115].

The adiabatic approximation fails at low temperatures (small D) where the escape time diverges and in this range the phase diagram has to be corrected numerically, see Fig. 4.64b. By simulating directly Eq. (4.41) we obtain that even the moderate temperature features of the diagram (tri-critical point, point D_e and the vertical asymptote of the boundary separating phases I and III at large values of A) are captured adequately by the adiabatic approximation. For instance, the value of temperature corresponding to point N (at infinite A) obtained from the adiabatic approximation is $D_N = q/[8(1 + k)]$ where q is a solution of a transcendental equation $q - k = q^{3/2}/[\sqrt{q} + \mathrm{e}^{1/q}\sqrt{\pi}(1 + \mathrm{erf}(1/q))]$ which agrees with our numerics.

The new feature of the non-adiabatic phase diagram is a dip of the boundary separating Phases II and III at some $D < D_e$ leading to an interesting re-entrant behavior (cf. [89, 118]). This is an effect of stochastic resonance which is not captured by adiabatic approximation.

To verify our numerical results in the low temperature domain $D \to 0$ we used Kramers approximation, valid when the rocking period τ is much smaller than the typical escape time of the bi-stable potential V.

It allows one to compute explicitly the location of point K ($A = 1/2$) and point M ($A = 1/2 + k/4$), which we found to be in full agreement with our numerical simulations, see Fig. 4.64b. Because of incompatibility of the limits $D \to 0$ and $\tau \to \infty$ these points are rather far from the corresponding adiabatic predictions K_A and M_A shown in Fig. 4.64a.

Force-elongation relations characterizing the mechanical response of the system at different points on the (A, D) plane (Fig. 4.64b) are shown in Fig. 4.65 where the upper insets illustrate the typical stochastic trajectories and the associated cycles in $\{\langle x(t)\rangle, f(t)\}$ coordinates. We observe that while in phase I thermal fluctuations dominate periodic driving and undermine the two wells structure of the potential, in phase III the jumps between the two energy wells are fully synchronized with the

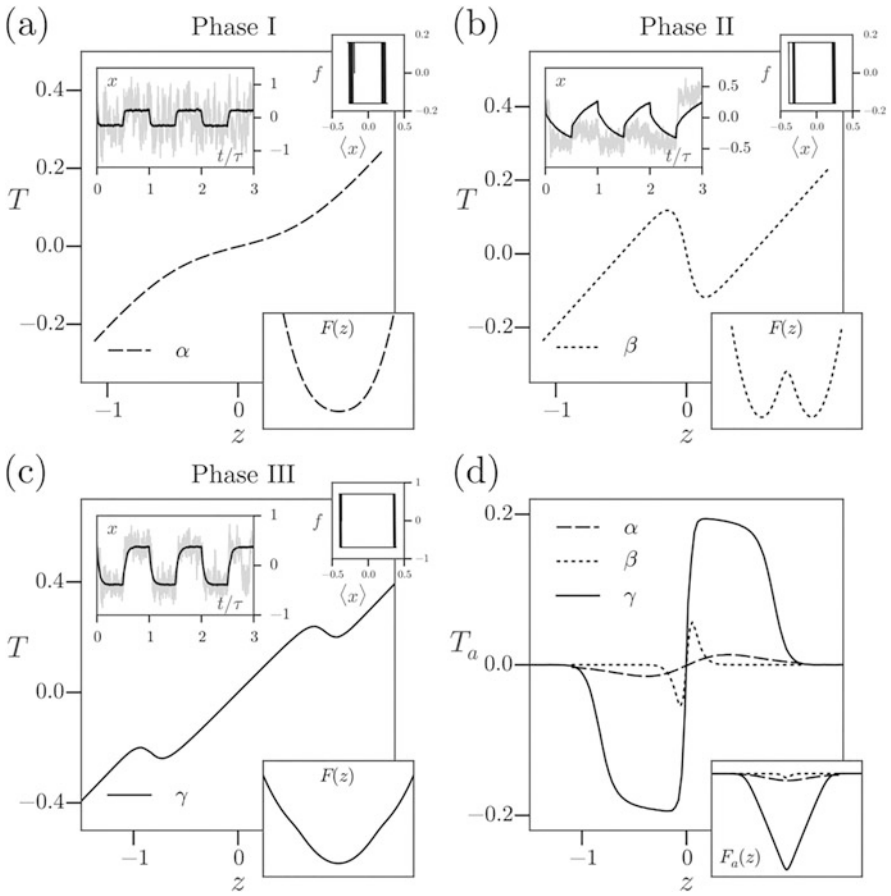

Fig. 4.65 (**a–c**) Typical tension-length relations in phases I, II and III. Points α, β and γ are the same as in Fig. 4.64b; (**d**) shows the active component of the force. Inserts show the behavior of stochastic trajectories in each of the phases at $z \simeq 0$ (gray lines) superimposed on their ensemble averages (black lines); the stationary hysteretic cycles, the structure of the effective potentials $F(z)$ and the active potential $F_a(z)$ defined as a primitive of the active force $T_a(z)$. The parameters: $k = 0.6$, $\tau = 100$

rocking force. In phase II the system shows intermediate behavior with uncorrelated jumps between the wells.

In Fig. 4.65d we illustrate the active component of the force $T_a(z) = T(z; A) - T(z; 0)$ in phases I, II and III. A salient feature of Fig. 4.65d is that active force generation is significant only in the resonant (Kapitza) phase III. A biologically beneficial plateau (tetanus) is a manifestation of the triangular nature of a pseudo-well in the active landscape $F_a(z) = \int^z T_a(s)ds$; note also that only slightly bigger $(f, < x >)$ hysteresis cycle in phase III, reflecting a moderate increase of the extracted work, results in considerably larger active force. It is also of interest that

the largest active rigidity is generated in the state $z = 0$ where the active force is equal to zero.

If we now estimate the non-dimensional parameters of the model by using the data on skeletal muscles, see Sect. 4.8.3, we obtain $A = 0.5$, $D = 0.01$, $\tau = 100$. This means that muscle myosins in stall conditions (isometric contractions), may be functioning in resonant phase III. Our simple model can therefore contribute to the explanation of the observed stability of skeletal muscles in the negative stiffness regime [19]; similar mechanism may be also behind the titin-based force generation at long sarcomere lengths [103].

Dichotomous (DC) Driving The P driving is only one among correlated signals that can serve as a mechanical representation of an out of equilibrium chemical reservoir. To ascertain the robustness of the results obtained in the case of P driving we now consider another type of correlated forcing which is also characterized by two parameters, the amplitude A and the characteristic time τ. It is given by the explicit formula $f(t) = A(-1)^{n(t)}$, where $n(t)$ is a Poisson process with $P(n) = e^{-\lambda}\lambda^n/n!$ with $\lambda = 1/(2\tau)$ and is known as symmetric dichotomous (DC) noise or random telegraph signal [55, 86]. For this Markov process we have $\langle f(t)\rangle = A\exp(-t/\tau)$ and $\langle f(t), f(s)\rangle = A^2\exp(-|t-s|/\tau)$.

The probability distribution can be written in the form $p(x,t) = p_-(x,t) + p_+(x,t)$ where $p_\pm(x,t)$ are the probability densities to be in a state x at time t given that $f = \pm A$. The DC driven system (4.41) is described by the two coupled Fokker–Planck equations [10],

$$\partial_t p_\pm = \partial_x(\partial_x E_\pm p_\pm + D\partial_x p_\pm) + \lambda(\mp p_\pm \pm p_\mp) \tag{4.48}$$

where $E_\pm(x) = \tilde{V}(x) \mp Ax$. Note that in this interpretation the DC noise appears as a chemical reaction violating the detailed balance [91]. The stationary version of the system (4.48) can be written in a transparent form if in addition to $p(x) = p_-(x) + p_+(x)$ we introduce a complimentary variable $d(x) = p_+(x) - p_-(x)$. Then we obtain

$$\begin{aligned} \partial_x \tilde{V} p - D\partial_x p - Ad = 0, \\ \tau\partial_x(\partial_x \tilde{V} d - D\partial_x d - Ap) = d. \end{aligned} \tag{4.49}$$

The numerical study of (4.41) with DC noise shows that the qualitative structure of the phase diagram in the (A, D) plane remains the same as in the case of P driving, see Fig. 4.66. We again observe phases I, II and III and the tri-critical point at about the same location as in the case of P noise.

To interpret the numerical results, it is instructive to consider analytically tractable special cases. First of all, Eq. (4.49) can be used to obtain the adiabatic ($\tau \to \infty$) limit when the two equations decouple and the steady state probability distributions take the form $p_\pm(x) \sim \exp(-E_\pm(x)/D)$ as in the case of P driving. The resulting phase diagrams are therefore identical, see section "Periodic (P) Driving".

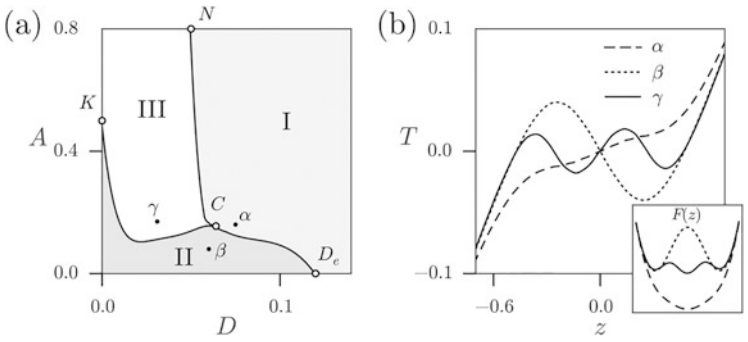

Fig. 4.66 (**a**) Phase diagram in the case of DC driving. The identification of phases I, II, and III is the same as in Fig. 4.64a, b. (**b**) Typical tension-length relations in different phases (**b**). Here $\tau = 100$ and $k = 0.6$

The second case, when the analytic results are available, is the zero temperature limit $D \to 0$ considered in detail in Sect. 4.8.5.

Finally, the third analytically tractable case is $\tau \to 0$, $A \to \infty$, with $\tilde{D} = A^2\tau$ remaining finite. In this limit we obtain that the non-equilibrium component of the noise is represented by a Gaussian white noise $f(t) = \sqrt{2\tilde{D}}\xi_a(t)$ with the temperature $\tilde{D}$ that is different from the temperature of the equilibrium reservoir D, for instance, one can think about a system exposed to a thermostat with temperature D and a chemostat with temperature $\tilde{D}$. The combined excitations are again represented by a white noise $\sqrt{2D^*}\xi_n(t)$ with effective temperature $D^* = \sqrt{D^2 + \tilde{D}^2}$.

In contrast to the zero temperature case, now the Kapitza phase III, describing active stabilization, is absent. We obtain only phases I and II separated by a second order phase transition line $\sqrt{D^2 + \tilde{D}^2} = D_e$ with the universal asymptotic behavior $\tilde{D} \sim (D_e - D)^{1/2}$ near equilibrium, see Fig. 4.67. The system in this limit can

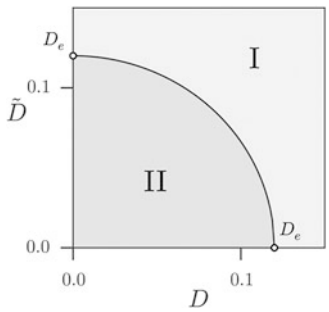

Fig. 4.67 Phase diagram for the case when the chemical reaction is modeled by an effective temperature $\tilde{D}$. Here $k = 0.6$

undergo entropic stabilization only which means that the two temperature model does not capture the same range of phenomena as the $D = 0$ model. Note that other two temperature models can exhibit destabilization of a single well system[44].

Ornstein–Uhlenbeck (OU) Driving We have seen that the overall effect of the two bounded noises on a mechanical system may be similar even though one of them is highly correlated and non-Markovian and another one is weakly correlated and Markovian. To show that not all noises are 'mechanically equivalent' we now consider an Ornstein–Uhlenbeck (OU) process which is also characterized by two parameters A and τ [8, 86].

In the case of OU driving, the function $f(t)$ is a solution of the stochastic equation

$$df(t)/dt = -\frac{1}{\tau} f(t) + A\sqrt{\frac{2}{\tau}}\xi_f(t). \tag{4.50}$$

Exactly as in the case of the DC noise we have for the first two moments $\bar{f}(t) = \langle f(t)\rangle = A\exp(-t/\tau)$, and $\langle f(s)f(t)\rangle = A^2\exp(-|t-s|/\tau)$, where we assumed for determinacy that $f(0) = A$. The resulting process is also Markovian, however now it is unbounded and is defined on a continuous state space.

The Fokker–Planck equation for the probability density $p(x, f, t)$ takes the form

$$\partial_t p = \partial_x(p\partial_x E + D\partial_x p) + \tau^{-1}\partial_f(fp + A^2\partial_f p). \tag{4.51}$$

Our numerical results for the system driven by OU noise are summarized in Fig. 4.68a. At small intensity of driving A we observe the conventional picture of entropic stabilization. A striking feature of this diagram is the absence of phase III, which means that in contrast to the cases of P and DC driving, the OU driven system does not support the phenomenon of active stabilization. To understand these

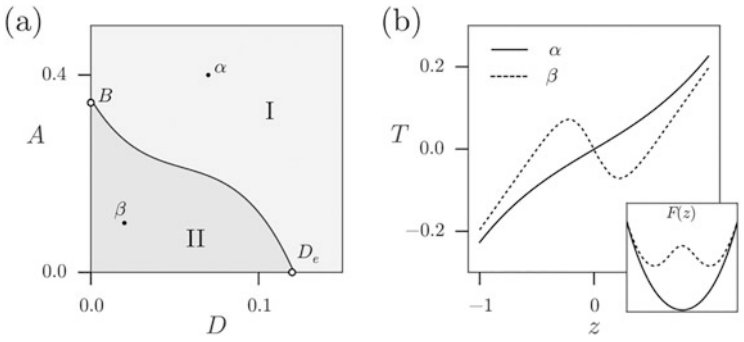

Fig. 4.68 (**a**) Phase diagram in the case of OU driving. The identification of phases I, II is the same as in Fig. 4.64a, b. (**b**) The typical tension-length relations in different phases. Here $\tau = 100$ and $k = 0.6$

numerical results it is instructive to consider the already mentioned three limiting cases that can be treated analytically.

In the adiabatic limit ($\tau \to \infty$), Eq. (4.51) simplifies and can be integrated. Then we obtain that $p(x) \sim \exp(-E(x)/D)$ which shows that in this limit only entropic stabilization remains possible.

Another analytically tractable limit is $D \to 0$, which shows again that in contrast to the cases of P and DC driving, only phases I and II are present at zero temperature phase diagram.

Finally, we can consider the double limit $\tau \to 0$, $A \to \infty$, with $\tilde{D} = A^2\tau$ fixed. As in the case of DC noise, we recover in this limit a system subjected to an effective temperature and showing phases I and II only, see Fig. 4.67.

The analysis of these special cases supports our numerical results suggesting that in the OU driven system the tri-critical point is absent. We can link the failure to generate active rigidity in such system with the unbounded nature of the OU noise allowing the eventual escape from a neighborhood of any resonant state.

4.8.5 *Zero Temperature Limit*

To understand better the differences between our three representations of non-equilibrium driving, we now compare the behavior of the system in the analytically tractable limit when the temperature of an equilibrium thermostat is equal to zero, $D = 0$. In this limit the role of passive stabilization is minimized, which allows one to make the effect of active terms more transparent. When $D = 0$ we are left with two non-dimensional parameters: the correlation time τ and the amplitude of the active signal A. We found, however, that using another pair $(\tau, \tilde{D})$, with $\tilde{D} = A^2\tau$, is more convenient.

Dichotomous (DC) Driving In the case of DC driving with $D = 0$ the stationary solution of the Fokker–Plank equation (4.49) can be written in the form [64]

$$p(x)\partial_x \tilde{V}(x) + A^2 \left[\frac{1}{\tau} - \partial_x \left(\partial_x \tilde{V}(x)\cdot\right)\right]^{-1} \partial_x p(x) = 0, \tag{4.52}$$

where the notation $\partial_x \left(\partial_x \tilde{V}\cdot\right)$ should be understood in the sense of differential operators. The formal solution of ((4.52)) satisfying zero boundary conditions at infinity can be written in quadratures [48, 64]

$$p(x) = \frac{Z^{-1}}{A^2 - (\partial_x \tilde{V}(x))^2} \exp\left(-\frac{1}{\tau}\int^x \frac{\partial_y \tilde{V}(y)}{A^2 - (\partial_y \tilde{V}(y))^2} dy\right),$$

where we still need to find the normalizing constant Z. For this solution to be valid we must also satisfy the inequality

$$|\partial_x \tilde{V}(x)| < A. \tag{4.53}$$

When $A = 0$, we recover the deterministic case where condition (4.53) selects between the points $x_{0,1}(0)$ where the force vanishes.

In principle, the choice depends on the initial condition but in the limit of vanishing D and large time t, the trajectory $x(t)$ converges to the point minimizing the potential $\tilde{V}$. The resulting tension elongation relation can be then obtained by setting

$$\overline{\langle x \rangle} = \frac{x_0(0) + x_1(0)}{2} + \text{sign}(z)\frac{x_1(0) - x_0(0)}{2}.$$

The effective energy $F(z)$ emerges as a symmetric two parabolic bi-stable potential where $z = 0$ is a singular spinodal point separating the energy wells at $z = \pm 1/2$.

Another simple case is when $\tau \to 0$ with $A^2\tau = \tilde{D}$ remaining finite. In this limit activity disappears and driving becomes equilibrium with temperature $\tilde{D}$. The steady state probability distribution is given by $p(x) \sim \exp(-\tilde{V}(x)/\tilde{D})$ and the effective energy exhibits a transition from phase II to phase I at the critical temperature D_e.

To compute $p(x)$ in the general case, we identify the admissible set, where ((4.53)) holds, as $]x_0(-A), x_0(A)[\sqcup]x_1(-A), x_1(A)[$ where

$$\begin{aligned}
x_0(-A) &= \min(0, \tfrac{-1/2+kz-A}{1+k}) \le x_0(A)\\
x_0(A) &= \min(0, \tfrac{-1/2+kz+A}{1+k}) \le 0\\
x_1(-A) &= \max(0, \tfrac{1/2+kz-A}{1+k}) \ge 0\\
x_1(A) &= \max(0, \tfrac{1/2+kz+A}{1+k}) \ge x_1(-A)
\end{aligned}$$

We can now integrate $p(x)$ on each of the segments $]x_0(-A), x_0(A)[$ and $]x_1(-A), x_1(A)[$. The result can be written in the form

$$\begin{aligned}
p(x) &= C_0\Psi_0(x)^{(2\tau(1+k))^{-1}-1}\mathbf{1}_{]x_0(-A),x_0(A)[}(x)\\
&+ C_1\Psi_1(x)^{(2\tau(1+k))^{-1}-1}\mathbf{1}_{]x_1(-A),x_1(A)[}(x),
\end{aligned} \tag{4.54}$$

where $\Psi_0(x) = A^2 - [(1+k)x - kz + 1/2]^2$ and $\Psi_1(x) = A^2 - [(1+k)x - kz - 1/2]^2$.

If the domain of definition is connected as in, say, *Case 2*, when $x_0(A) = x_1(-A) = 0$, a continuity condition relates C_0 and C_1:

$$\begin{aligned}
C_0 &= Z^{-1}\Psi_1(0)^{(2\tau(1+k))^{-1}},\\
C_1 &= Z^{-1}\Psi_0(0)^{(2\tau(1+k))^{-1}}.
\end{aligned} \tag{4.55}$$

If instead either $x_0(A)$ or $x_1(-A)$ is different from zero, the two sets $]x_0(-A), x_0(A)[$ and $]x_1(-A), x_1(A)[$ are separated by a segment where the probability is equal to zero. This means that the passage from one region to the other is impossible. In this case the coefficients C_0 and C_1 depend on the initial probability distribution as in the periodic case (at $D = 0$).

If we regularize the problem by adding a weak white noise (small $D \neq 0$), the choice of constants becomes again unambiguous as we can associate the support of the distribution with the side (0 or 1) opposite to the smallest potential barrier. We can then write explicitly $C_1 = Z^{-1}\max(0, \text{sign}(z))$ and $C_0 = Z^{-1} - C_1$. In all cases the constant Z is found from normalization.

We illustrate the stationary probability distributions $p(x)$ in Fig. 4.69a for several choices of parameters. The analytical expression for the tension elongation curves $T(z)$ involve hypergeometric functions and is too complex to be presented here. The resulting curves are illustrated in Fig. 4.69 for small and large values of the correlation time. The phase diagram, shown in Fig. 4.70a, exhibits all three phases I, II and III with a tri-critical point C' located at $\tau_{C'} = [2(k+1)]^{-1}$ and $\tilde{D}_{C'} = D_e + [2(k+1)]^{-1}/4$. The behavior of the force-elongation relations in different phases is illustrated in Fig. 4.70b. As we see, the DC driven dynamics is sufficiently rich to capture both active and entropic stabilization phenomena even in the absence of the equilibrium reservoir (at $D = 0$).

Periodic (P) Driving The numerical simulations for the problem with P driving and $D \to 0$ show only phases II and III even for rapidly oscillating external fields, see Fig. 4.70c.

To understand this result we can use Kramers approximation which can be developed under the assumption that the rocking period is short comparing to at least one of the escape times $\tau_{0,1}(\pm A)$. The use of such anti-adiabatic limit is consistent with the observation that in the limit $D \to 0$ the escape times from the energy wells diverge.

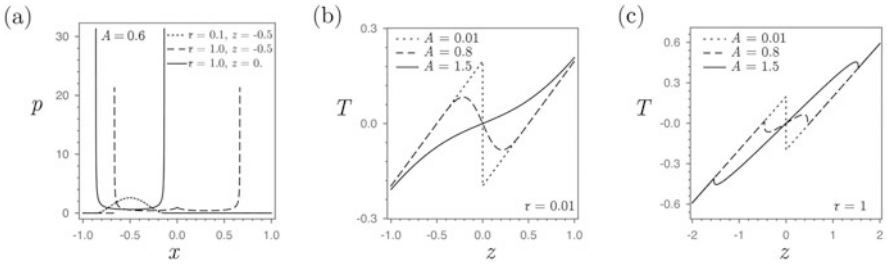

Fig. 4.69 (**a**) Examples of stationary probability distributions in the case of DC driving with $A = 0.6$. Dotted line: $\tau = 0.1$, $z = -0.5$. Dashed line: $\tau = 1$, $z = -0.5$. Solid line: $\tau = 1$, $z = 0$. (**b–c**) Tension elongation relations for different values of τ

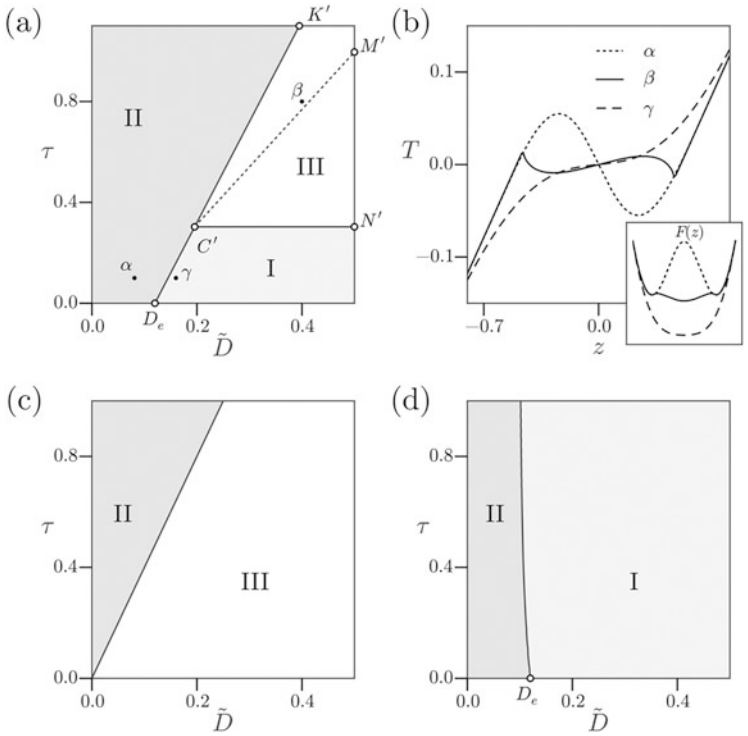

Fig. 4.70 (**a**) Zero temperature phase diagram in the case of DC driving. The identification of phases I, II and III is the same as in Fig. 4.64a, b. Tension-elongation relations in the case of DC driving in different phases (**b**). Zero temperature phase diagram in the case of P driving (**c**) and OU driving (**d**). Parameters $k = 0.6$, $D = 0$

A study of the purely mechanical problem with P driving reveals that, since the potential E can have up to four local minima, the dynamical system 4.44 can have up to four stationary solutions. We have four main cases:

- *Case 1*: $\overline{\langle x \rangle} = [x_0(-A) + x_0(A)]/2$
- *Case 2*: $\overline{\langle x \rangle} = [x_0(-A) + x_1(A)]/2$
- *Case 3*: $\overline{\langle x \rangle} = [x_1(-A) + x_1(A)]/2$
- *Case 4*:

$$\overline{\langle x \rangle} = \begin{cases} \frac{1}{2}\left[x_0(-A) + x_0(A)\right], & \text{if } z < 0 \\ \\ \frac{1}{2}\left[x_1(-A) + x_1(A)\right], & \text{if } z > 0. \end{cases}$$

To justify, for instance, the last expression (*Case 4*) we can apply the rate theory for rocked bi-stable system. Then we obtain for $n_0(t)$ (the number of particle in the well 0 at the moment t) the expression

$$\langle n_0 \rangle \sim \mathrm{e}^{\left(-\min\limits_{\pm A}[\Delta E_1(\pm A)]+\min\limits_{\pm A,1,0}[\Delta E_{0,1}(\pm A)]\right)/D}.$$

Here either $\min\limits_{\pm A} \Delta E_1(\pm A) = \min\limits_{\pm A,1,0} \Delta E_{0,1}(\pm A)$ and $\langle n_0 \rangle = 1$, or $\min\limits_{\pm A} \Delta E_1(\pm A) > \min\limits_{\pm A,1,0} \Delta E_{0,1}(\pm A)$ and $\langle n_0 \rangle = 0$. The condition $\min\limits_{\pm} \Delta E_1(\pm A) > \min\limits_{\pm,1,0} \Delta E_{0,1}(\pm A)$ introduces the dependence of the stationary distribution on z. After time averaging, the steady state probability distribution takes the form:

$$\begin{aligned} p(x) = &\frac{\langle n_0 \rangle}{2}\left[p_0(x;-A)+p_0(x;A)\right] \\ &+\frac{1-\langle n_0 \rangle}{2}\left[p_1(x;-A)+p_1(x;A)\right], \end{aligned} \tag{4.56}$$

where

$$p_0(x;\pm A) = \frac{\exp\left(-E_0(x;\pm A)/D\right)}{\int\limits_{-\infty}^{0} \exp\left(-E_0(x;\pm A)/D\right) dx}$$

$$p_1(x;\pm A) = \frac{\exp\left(-E_1(x;\pm A)/D\right)}{\int\limits_{0}^{\infty} \exp\left(-E_1(x;\pm A)/D\right) dx}.$$

In the limit $D \to 0$ the distributions $p_{0,1}(x;\pm A)$ become delta functions concentrated at the points $x_{0,1}(\pm A)$ which gives our formula for $\overline{\langle x \rangle}$.

If we now use the computed values for $x_{0,1}(\pm A)$, we can obtain the analytic expressions for the tension $T(z)$. Then, by solving the equation $T(z) = 0$ we can locate the line of the first order phase transition separating phases II and III and show that $A = \frac{1}{2}$ at point K and that $A = \frac{1}{2}\left(1+\frac{k}{2}\right)$ at point M, both in agreement with the numerical phase diagram presented in Fig. 4.71c. The qualitative difference between the predictions of the adiabatic approximation implying that D is large and the Kramers approximations corresponding to small D is illustrated in Fig. 4.71.

In coordinates $(\tau, \tilde{D})$ the phase diagram for the P driven system with zero temperature shows a single phase boundary separating phases II and III, see Fig. 4.70c. The entropically stabilized phase II is absent because, despite the presence of the noise, it is bounded and there is no stochastic contribution allowing the system to cross arbitrary barriers. Because of the same reason the phase boundary between phases II and III in the P driven system is shifted comparing to the case of DC driving as the point D_e does not exist any more. This is in contrast to the fact that at finite D the two systems (with P and DC driving) behave quite similarly, in particular, they are indistinguishable in the adiabatic limit $\tau \to \infty$.

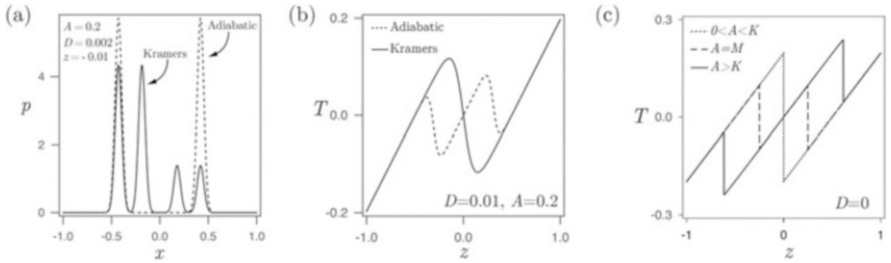

Fig. 4.71 (**a**) Examples of the stationary probability distributions in the case of P driving in adiabatic (dotted line) and Kramers (solid line) approximations at $A = 0.2$, $z = -0.01$, $D = 0.002$. (**b**) Tension elongation relations for $D = 0.01$ and $A = 0.2$ expressed by Kramers solution (solid line) and adiabatic solution (dotted line). (**c**) Tension elongation relations in the limit $D \to 0$ for several value of A. For $0 < A < K$, all curves collapse (dotted line) since the energy injected by the rocking is not sufficient to overcome the potential barriers

Ornstein–Uhlenbeck (OU) Driving In the case of OU driving with $D = 0$ an analytical approximation of the stationary probability distribution is available when $\tau << 1$ [48]. The main idea is to combine Eq. (4.44) and Eq. (4.50) to obtain a new equation for a noisy inertial oscillator

$$\frac{d^2x}{dt^2} + \frac{dx}{dt}(1 + \tau\partial_{xx}\tilde{V}(x)) + \partial_x\tilde{V}(x) = A\sqrt{2\tau}\xi_f(t), \tag{4.57}$$

where ξ_f is a standard white noise. At large times the inertial dynamics with additive noise (4.57) can be approximated by the overdamped dynamics with multiplicative noise

$$\frac{dx}{dt} = (1 + \tau\partial_{xx}\tilde{V}(x))^{-1}\left(-\partial_x\tilde{V}(x) + A\sqrt{2\tau}\xi_f(t)\right)$$

which must be interpreted in the Stratanovitch sense [48]. The corresponding Fokker Planck equation

$$\begin{aligned}\partial_t p &= \partial_x\left(\frac{\partial_x\tilde{V}}{1 + \tau\partial_{xx}\tilde{V}}p\right) \\ &+ \partial_x\left(\frac{1}{1 + \tau\partial_{xx}\tilde{V}}\partial_x\left(\frac{A^2\tau}{1 + \tau\partial_{xx}\tilde{V}}p\right)\right),\end{aligned} \tag{4.58}$$

has an explicit stationary solution [48]:

$$p(x) = Z^{-1}|1 + \tau\partial_{xx}\tilde{V}(x)|\exp\left(-\frac{\tilde{V}(x) + \tau(\partial_x\tilde{V}(x))^2/2}{A^2\tau}\right).$$

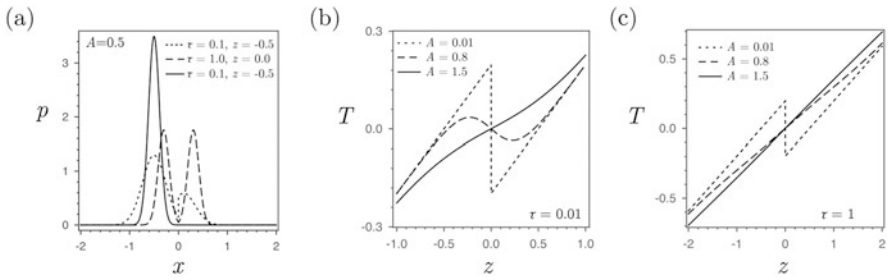

Fig. 4.72 (**a**) Examples of stationary probability distributions in the case of OU driving at $A = 0.5$; dotted line: $\tau = 1$, $z = -0.5$; dashed line: $\tau = 1$, $z = 0$; solid line: $\tau = 0.1$, $z = -0.5$. (**b–c**) Tension elongation relations in the OU cases for small (**b**) and large (**c**) correlation times. Large correlation times are formally outside of the domain of validity of the approximation

Notice again that when $\tau \to 0$ with $\tilde{D} = \tau A^2$ fixed, $f(t)$ becomes a white noise and the distribution $p(x)$ takes the classical Boltzmann form.

In Fig. 4.72a we show examples of the stationary distributions for specific values of parameters. The corresponding tension curves $T(z)$ are illustrated in Fig. 4.72b, c for large and small correlation times.

Our Fig. 4.70d shows the resulting phase diagram which, as expected, exhibits only phases I and II. This is again a confirmation of the fact that in the case of OU driving the crucial phase III, describing the phenomenon of active regidity, is absent. When τ is small (at a fixed $\tilde{D}$), the OU noise becomes a white noise and, as in the case of the DC driving, the phase boundary separating phases I and II passes through the point D_e.

The comparison of all three phase diagrams, shown in Fig. 4.70a, c, d suggests, that at zero temperature the system with DC driving is an intricate *amalgam* of the systems with OU and P drivings.

4.9 Conclusions

In these lecture notes we discussed the possibility that acto-myosin contraction is driven exclusively by the power-stroke. We developed several mechanistic models built on the assumption that the microscopic stochastic dynamics can be described by a set of continuous equations of mechanics with the equilibrium thermal environment modeled by a uncorrelated noise and internal activity modeled in different ways, in particular, by a correlated noise. The correlations associated with nonthermal such noise would then reflect the nonequilibrium nature of the external reservoir.

To model the full cross-bridge mediated actin-myosin interaction we developed three-dimensional phase space framework coupling a periodic potential with a bi-stable potential. In this perspective, the periodic potential represents myosin/actin

interaction; the conformational change responsible for the power stroke is described by a double-well potential. The mechanical approach allowed us to reveal the important difference between the soft and hard device loading conditions. We mention that this asymmetry remained under-appreciated in the conventional chemo-mechanical models.

Our starting point was the observation that in the currently accepted mechanistic representations of acto-myosin systems, the power-stroke is undermined as a passive folding-unfolding mechanism while the attachment-detachment is given a primary role as the main driver of contraction. Since active sites are located inside motor domains, the external forces, representing the ATP activity, are typically introduced as conjugates to macroscopic positions of these domains and such ratchets are essentially attachment-detachment-driven. The implied mechanisms may be indeed operative during muscle contractions but then they would be complimentary to the ones studied here. In our approach the thrust of the ATP activity was shifted towards the internal variable characterizing the state of the power-stroke element.

Depending on the particular sub-unit where the external correlated force is applied, we introduced three basic designs of the force generating ratchet machinery. By localizing the effect of the correlated rocking on a single internal degree of freedom, we defined three basic models: X-tilted, Y-tilted and XY-tilted ratchets.

The X-tilted ratchet is the conventional mechanism where the external activity is concentrated in the actin filament. We have shown that with X-tilted ratchet design one cannot simulate the full four-state Lymn–Taylor cycle because the detachment of the cross-bridge head and the recharge of the power stroke are always combined. Another shortcoming of this model is that it does not treat adequately the detached configuration of the acto-myosin system.

In the Y-tilted ratchet model the correlated noise acts on the internal variable located inside the power stroke mechanism making both the power stroke and the actin filament active. The resulting ratchet performs four-state cycle in the soft device and either two-state or four-state cycle in the hard device. This suggests that the Y-tilted ratchet framework is capable in principle of mimicking the complete Lymn–Taylor cycle, however the mechanistic interpretation of such internal drive in term of the molecular structure of the cross-bridge remains ambiguous.

Finally, the XY-tilted ratchet model can be viewed as a mechanistic system which is driven entirely through the activity concentrated in the power stroke element while the actin filament is interpreted as passive. By treating the power stroke as the primary mechanism we delegated to the attachment/detachment process the secondary role of a machinery securing translational character of the motion. However, since the XY-tilted ratchet was shown to generate only three-state cycle it remains fundamentally incompatible with the existing biochemical models.

The main limitation of all these models is that the detached state is represented as a maximum of the periodic and therefore the detachment takes place very quickly. To overcome this problem we developed a synthetic model where the XY tilted ratchet mechanism was augmented by taking into consideration the explicit steric separation of thick and thin filaments. To make a clear distinction between our model and the conventional models of Brownian ratchets we assumed that the actin

track is non-polar and that the bi-stable element is unbiased. The symmetry breaking was then achieved exclusively through the coupling of these two sub-systems.

Our synthetic model accounting for steric effects was based on the assumption that the multiplicative feedback is acting on the space-periodic potential $\Phi(x)$. In this model the conformational state of the power stroke mechanism regulates the distance of the myosin head form actin filament. We associated the pre-power stroke with a detached state (no interaction with the spatial periodic potential $\Phi(x)$) and the post power stroke—with the attached state (the system interacts strongly with the space periodic potential $\Phi(x)$). In this way the detached state was fully integrated into the mechanical cycle. The resulting model reproduced all four states of the Lymn–Taylor cycle where the individual states were interpreted as transient mechanical configurations.

By considering three classes of models of this type we exposed three different ways of how a power-stroke-driven ratchet can receive energy of the ATP hydrolysis and presented mechanical representations of the associated non equilibrium chemical reservoirs. In the first, traditional, representation, a mechanical action of the chemical reaction was modeled by a correlated component of the noise. The second representation was based on the idea that the coupling between internal and external degrees of freedom is hysteretic. Here in contrast to what is usually observed in macroscopic systems, hysteresis was used as a source rather than a sink of energy. The third representation implied that the internal degrees of freedom have an inherently chemical origin and therefore the source of non-equilibrium is in the lack of potentiality of these forces. We have shown that only the hysteretic design allows one to reproduce fully adequately the complete four state Lymn–Taylor cycle.

In the last section of these lecture notes we assumed that attachment detachment machinery is disabled and addressed the question whether a power stroke driven molecular device can generate effective rigidity. Instead of a single stall state, the proposed model was shown to exhibit a family of stall states and we quantified the energetic cost of moving from one member of the family to another. Since in our case the implied parameter had the meaning of meso-scopic strain, the derivative of the (time averaged) energy with respect to this parameter could be interpreted as the effective rigidity.

Our prototypical mean field model of active rigidity supports the idea that by controlling the degree of non-equilibrium in the system, one can stabilize apparently unstable or marginally stable mechanical configurations and in this way modify the structure of the effective energy landscape (when it can be defined). Our analysis, however, reveals that apparently similar noises can generate qualitatively different mechanical effects and that the very possibility of the power-stroke driven stabilization of an unstable state may be ultra-sensitive to the higher moments of the stochastic forces.

To summarize, we provided compelling evidence that a relatively simple mechanical system is able to generate complex stochastic dynamics imitating muscle contractions. In particular, we showed that such system can mechanistically reproduce the complete Lymn–Taylor cycle. This opens a way towards structural interpretation of the chemical states, known from the studies of the catalytic cycle

in solution, and determining functionality of the particular transient mechanical configurations of the acto-myosin complex. The implied identification is a precondition for the bio-engineering reproduction of a wide range of cellular processes, where myosin cross-bridges play the dominant role, from movement of cells to cytokinesis. Given that the mechanisms involved in our model can be mimicked artificially at a super-cellular scale, the proposed schematization of the contraction phenomenon can be viewed as a step towards building engineering devices imitating acto-myosin enzymatic activity.

It is also important to mention that starting from the existing approach of rocking ratchets and reinventing it in the framework of the power stroke activity, we were able to unify the description of a single processive molecular motor such as Kinesin, with the description of the collectively operating non-processive molecular motors such as myosin. In this way we built a bridge between theoretical description myosin and Kinesin motors that have so far been treated as fundamentally different. In support of the idea that both processive and non-processive motors can be driven through a conformational change, we mention that the general shape of the force-velocity relations obtained in this paper is compatible with the available measurements not only for non-processive motors but also for processive motors [27, 60, 80, 123].

We showed, in particular, that while the most realistic XY tilted ratchet can perform a positive mechanical work, it is less efficient than X and Y ratchets. To understand why such seemingly inefficient device may be selected by evolution, it is important to remember that alternative, more efficient strategies include mechanical activity of actin filaments which is mechanically rather ambiguous.

The main limitation of the discussed picture of contraction is that it was developed for a single cross-bridge while important collective effects were neglected, see Fig. 4.73. A theory accounting for the implied collective effects has been so far developed only for passive response of skeletal muscles involving mechanically induced power stroke but not the attachment-detachment [19] and in active regimes one can expect a variety of interesting phenomena from coherent fluctuations [26, 45, 59, 121] to self-tuning towards criticality [5, 106]. Yet another reason for

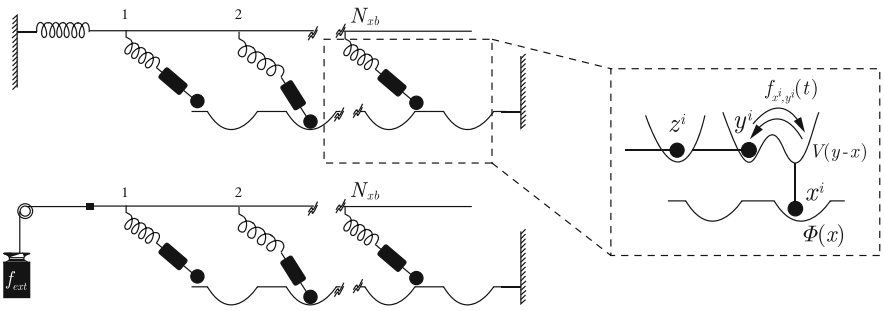

Fig. 4.73 Schematic representation of collectively interacting myosin motors: (**a**) hard device configuration. (**b**) soft device configuration

the observed inefficiency of the XY ratchet may be the neglect of quenched disorder whose account allows one to build a link between muscle architecture and the theory of spin glasses and reveal a tight relation between actomyosin disregistry and the optimal mechanical performance of the force generating machinery [21].

The schematic nature of the proposed models, allowing one to identify only the main mechanisms, is the main reason why we did not attempt to perform a systematic quantitative comparison of our predictions with experiment. Extending the proposed framework towards the account of collectively interacting cross-bridges will open the possibility to calibrate the model using experimental data. Given the purely mechanical nature of our modeling, one can then consider building the actual artificial molecular size devices based on the principles developed in these lecture notes.

The proposed framework also raises some specific issues which need to be addressed in future work. One challenge is to understand the microscopic nature of the hysteretic element and of the active mechanism ensuring the non-potential force structure. Another challenge is to find the optimal interaction of our three active mechanisms ensuring the highest performance of the power-stroke driven motor. The third challenge is to study the effects of short range interaction of elastically coupled power-stroke-driven motors.

The experimental verification of the proposed model of active rigidity requires quantitative monitoring of the mechanical properties of a biological system (say, cytoskeleton) combined with the control of activity elements (say, molecular motors) and the corresponding experimental techniques are already available [1, 37]. The mastery of actively tunable rigidity will open interesting prospects not only in biomechanics [92] but also in engineering design incorporating negative stiffness [39] or aiming at synthetic materials involving dynamic stabilization [16, 101].

References

1. W.W. Ahmed, É. Fodor, T. Betz, Active cell mechanics: measurement and theory. Biochim. Biophys. Acta, Mol. Cell Res. **1853**(11), 3083–3094 (2015)
2. R. Ait-Haddou, W. Herzog, Brownian ratchet models of molecular motors. Cell Biochem. Biophys. **38**(2), 191–213 (2003)
3. B. Alberts, *Molecular Biology of the Cell*, 5th edn. (Garland Science, New York, 2007)
4. F. Alouges, A. DeSimone, A. Lefebvre, Optimal strokes for low Reynolds number swimmers: an example. J. Nonlinear Sci. **18**(3), 277–302 (2008)
5. J. Alvarado, M. Sheinman, A. Sharma, F.C. MacKintosh, G.H. Koenderink, Molecular motors robustly drive active gels to a critically connected state. Nat. Phys. **9**, 591—597 (2013)
6. J.P. Baltanás, L. Lopez, I.I. Blechman, P.S. Landa, A. Zaikin, J. Kurths, M.A.F. Sanjuán, Experimental evidence, numerics, and theory of vibrational resonance in bistable systems. Phys. Rev. E **67**(6), 066119 (2003)
7. C. Barclay, R. Woledge, N. Curtin, Inferring crossbridge properties from skeletal muscle energetics. Prog. Biophys. Mol. Bio. **102**(1), 53–71 (2010)
8. R. Bartussek, Ratchets driven by colored gaussian noise, in *Stochastic Dynamics*, ed. by L. Schimansky-Geier, T. Pöschel. Lecture Notes in Physics, vol. 484 (Springer, Berlin, 1997), pp. 68–80

9. U. Basu, C. Maes, K. Netočnỳ, How statistical forces depend on the thermodynamics and kinetics of driven media. Phys. Rev. Lett. **114**(25), 250601 (2015)
10. I. Bena, C. Van den Broeck, R. Kawai, K. Lindenberg, Drift by dichotomous Markov noise. Phys. Rev. E **68**(4), 041111 (2003)
11. L. Berthier, J. Kurchan, Non-equilibrium glass transitions in driven and active matter. Nat. Phys. **9**(5), 310–314 (2013)
12. J. Bialké, J.T. Siebert, H. Löwen, T. Speck, Negative interfacial tension in phase-separated active Brownian particles. Phys. Rev. Lett. **115**(9), 098301 (2015)
13. I.I. Blekhman, *Vibrational Mechanics: Nonlinear Dynamic Effects, General Approach, Applications* (World Scientific, Singapore, 2000)
14. J.-P. Bouchaud, A. Georges, Anomalous diffusion in disordered media: statistical mechanisms, models and physical applications. Phys. Rep. **195**(4), 127–293 (1990)
15. Z. Bryant, D. Altman, J. Spudich, The power stroke of myosin vi and the basis of reverse directionality. Proc. Nat. Acad. Sci. U.S.A. **104**(3), 772–777 (2007)
16. M. Bukov, L. D'Alessio, A. Polkovnikov, Universal high-frequency behavior of periodically driven systems: from dynamical stabilization to Floquet engineering. Adv. Phys. **64**(2), 139–226 (2015)
17. E.I. Butikov, An improved criterion for Kapitza's pendulum stability. J. Phys. A Math. Theor. **44**(29), 295202 (2011)
18. F.J. Cao, L. Dinis, J.M.R. Parrondo, Feedback control in a collective flashing ratchet. Phys. Rev. Lett. **93**(4), 040603 (2004)
19. M. Caruel, J.-M. Allain, L. Truskinovsky, Muscle is a meta-material operating at a critical point. Phys. Rev. Lett. **110**(24), 248103 (2013)
20. L.F. Cugliandolo, D.R. Grempel, C.A. da Silva Santos, From second to first order transitions in a disordered quantum magnet. Phys. Rev. Lett. **85**(12), 2589–2592 (2000)
21. H.B. da Rocha, L. Truskinovsky, Functionality of disorder in muscle mechanics. Phys. Rev. Lett. **122**(8), 088103 (2019)
22. E. De La Cruz, E. Ostap, Relating biochemistry and function in the myosin superfamily. Curr. Opin. Cell Biol. **16**(1):61–67 (2004)
23. S. Denisov, Particle with internal dynamical asymmetry: chaotic self-propulsion and turning. Phys. Lett. A **29**6(4), 197–203 (2002)
24. I. Derényi, T. Vicsek, The Kinesin walk: A dynamic model with elastically coupled heads. Proc. Nat. Acad. Sci. U.S.A. **93**(13), 6775–6779 (1996)
25. C.R. Doering, W. Horsthemke, J. Riordan, Nonequilibrium fluctuation-induced transport. Phys. Rev. Lett. **72**(19), 2984 (1994)
26. T. Duke, Molecular model of muscle contraction. Proc. Nat. Acad. Sci. U.S.A. **96**(6), 2770–2775 (1999)
27. T. Duke, S. Leibler, Motor protein mechanics: a stochastic model with minimal mechanochemical coupling. Biophys. J. **71**(3), 1235–1247 (1996)
28. B. Dybiec, E. Gudowska-Nowak, I.M. Sokolov, Stationary states in Langevin dynamics under asymmetric Lévy noises. Phys. Rev. E **76**(4), 041122 (2007)
29. B. Dybiec, L. Schimansky-Geier, Emergence of bimodality in noisy systems with single-well potential. Eur. Phys. J. B **57**(3), 313–320 (2007)
30. K.A.P. Edman, Double-hyperbolic force velocity relation in frog-muscle fibers. J. Physiol. Lond. **404**, 301–321 (1988)
31. K.A.P. Edman, A. Månsson, C. Caputo, The biphasic force-velocity relationship in frog muscle fibres and its evaluation in terms of cross-bridge function. J. Physiol. **503**(1), 141–156 (1997)
32. T. Elston, C. Peskin, The role of protein flexibility in molecular motor function: coupled diffusion in a tilted periodic potential. SIAM J. Appl. Math. **60**(3), 842–867 (2000)
33. T. Erdmann, U. Schwarz, Stability of adhesion clusters under constant force. Phys. Rev. Lett. **92**(10), 108102 (2004)
34. N. Etemadi, M. Kaminski, Strong law of large numbers for 2-exchangeable random variables. Stat. Probab. Lett. **28**(3), 245–250 (1996)

35. M. Feito, J.P. Baltanás, F.J. Cao, Rocking feedback-controlled ratchets. Phys. Rev. E **80**(3), 031128 (2009)
36. M. Feito, F. J. Cao, Time-delayed feedback control of a flashing ratchet. Phys. Rev. E **76**(6), 061113 (2007)
37. É. Fodor, W.W. Ahmed, M. Almonacid, M. Bussonnier, N.S. Gov, M.-H. Verlhac, T. Betz, P. Visco, F. van Wijland, Nonequilibrium dissipation in living oocytes (2015). arXiv:1511.00921
38. C. Fogle, J. Rudnick, D. Jasnow, Protein viscoelastic dynamics: a model system (2015). arXiv:1502.00343 [cond-mat]
39. F. Fritzen, D.M. Kochmann, Material instability-induced extreme damping in composites: a computational study. Int. J. Solids Struct. **51**(23–24), 4101–4112 (2014)
40. R. Gallardo, O. Idigoras, P. Landeros, A. Berger, Analytical derivation of critical exponents of the dynamic phase transition in the mean-field approximation. Phys. Rev. E **86**(5), 051101 (2012)
41. L. Gammaitoni, P. Hänggi, P. Jung, F. Marchesoni, Stochastic resonance: a remarkable idea that changed our perception of noise. Eur. Phys. J. B **69**(1), 1–3 (2009)
42. M.A. Geeves, Stretching the lever-arm theory. Nature **415**(6868), 129–131 (2002)
43. B. Geislinger, R. Kawai, Brownian molecular motors driven by rotation-translation coupling. Phys. Rev. E **74**(1), 011912 (2006)
44. A. Grosberg, J.-F. Joanny, Nonequilibrium statistical mechanics of mixtures of particles in contact with different thermostats. Phys. Rev. E **92**(3), 032118 (2015)
45. T. Guérin, J. Prost, P. Martin, J.-F. Joanny, Coordination and collective properties of molecular motors: theory. Curr. Opin. Cell Biol. **22**(1), 14–20 (2010)
46. T. Guérin, J. Prost, P. Martin, J.-F. Joanny, Dynamical behavior of molecular motor assemblies in the rigid and crossbridge models. Eur. Phys. J. E **34**(6), 60 (2011)
47. A.N. Gupta, A. Vincent, K. Neupane, H. Yu, F. Wang, M.T. Woodside, Experimental validation of free-energy-landscape reconstruction from non-equilibrium single-molecule force spectroscopy measurements. Nat. Phys. **7**(8), 631–634 (2011)
48. P. Hänggi, P. Jung, Colored noise in dynamical-systems, in *Advances in Chemical Physics*, vol. 89 (Wiley, London, 1995), pp. 239–326
49. P. Hänggi, F. Marchesoni, Artificial Brownian motors: Controlling transport on the nanoscale. Rev. Mod. Phys. **81**(1), 387–442 (2009)
50. D. Hennig, Current control in a tilted washboard potential via time-delayed feedback. Phys. Rev. E **79**(4), 041114 (2009)
51. A.V. Hill, The heat of shortening and the dynamic constants of muscle. Proc. R. Soc. Lond. B **126**, 136–195 (1938)
52. T. Hill, Theoretical formalism for the sliding filament model of contraction of striated muscle. part I. Prog. Biophys. Mol. Biol. **28**, 267–340 (1974)
53. J. Howard, *Mechanics of Motor Proteins and the Cytoskeleton* (Sinauer Associates, Sunderland, 2001)
54. A.F. Huxley, R.M. Simmons, Proposed mechanism of force generation in striated muscle. Nature **233**(5321), 533–538 (1971)
55. A. Ichiki, Y. Tadokoro, M.I. Dykman, Singular response of bistable systems driven by telegraph noise. Phys. Rev. E **85**(3), 031106 (2012)
56. M. Joyeux, E. Bertin, Pressure of a gas of underdamped active dumbbells. Phys. Rev. E **93**(3), 032605 (2016)
57. F. Jülicher, Force and motion generation of molecular motors: a generic description, in *Transport and Structure* (Springer, Berlin, 1999), pp. 46–74
58. F. Jülicher, A. Ajdari, J. Prost, Modeling molecular motors. Rev. Mod. Phys. **69**(4), 1269–1281 (1997)
59. F. Jülicher, J. Prost, Spontaneous oscillations of collective molecular motors. Phys. Rev. Lett. **78**(23), 4510–4513 (1997)
60. K. Kawaguchi, S. Ishiwata, Temperature dependence of force, velocity, and processivity of single Kinesin molecules. Biochem. Bioph. Res. Commun. **272**(3), 895–899 (2000)

61. M. Khoury, J.P. Gleeson, J.M. Sancho, A.M. Lacasta, K. Lindenberg, Diffusion coefficient in periodic and random potentials. Phys. Rev. E **80**(2), 021123 (2009)
62. K. Kitamura, M. Tokunaga, S. Esaki, A. Iwane, T. Yanagida, Mechanism of muscle contraction based on stochastic properties of single actomyosin motors observed in vitro. Biophysics **1**, 1–19 (2005)
63. P. Kloeden, E. Platen, *Numerical Solution of Stochastic Differential Equations*. Applications of Mathematics, vol. 23 (Springer, Berlin, 1992)
64. V. Klyatskin, Dynamic systems with parameter fluctuations of the telegraphic-process type. Radiofizika **20**(4), 562–575 (1977)
65. G. Lan, S.X. Sun, Dynamics of myosin-driven skeletal muscle contraction: I. Steady-state force generation. Biophys. J. **88**(6), 4107 (2005)
66. P.S. Landa, P.V.E. McClintock, Nonlinear systems with fast and slow motions. changes in the probability distribution for fast motions under the influence of slower ones. Phys. Rep. **532**(1), 1–26 (2013)
67. A. Lewalle, W. Steffen, O. Stevenson, Z. Ouyang, J. Sleep, Single-molecule measurement of the stiffness of the Rigor myosin head. Biophys. J. **94**(6), 2160–2169 (2008)
68. Y.-X. Li, Brownian motors possessing internal degree of freedom. Phys. A **251**(3), 382–388 (1998)
69. M. Linari, M. Caremani, V. Lombardi, A kinetic model that explains the effect of inorganic phosphate on the mechanics and energetics of isometric contraction of fast skeletal muscle. Proc. Biol. Sci. **277**(1678), 19–27 (2010)
70. B. Lindner, M. Kostur, L. Schimansky-Geier, Optimal diffusive transport in a tilted periodic potential. Fluct. Noise Lett. **1**(1), R25–R39 (2001)
71. V. Lombardi, G. Piazzesi, The contractile response during steady lengthening of stimulated frog-muscle fibers. J. Physiol. Lond. **431**, 141–171 (1990)
72. R. Lymn, E. Taylor, Mechanism of adenosine triphosphate hydrolysis by actomyosin. Biochemistry **10**(25), 4617–4624 (1971)
73. Magnasco, Molecular combustion motors. Phys. Rev. Lett. **72**(16), 2656–2659 (1994)
74. M.O. Magnasco, Forced thermal ratchets. Phys. Rev. Lett. **71**(10), 1477–1481 (1993)
75. Y.A. Makhnovskii, V.M. Rozenbaum, D.-Y. Yang, S.H. Lin, Net transport due to noise-induced internal reciprocating motion. J. Chem. Phys. **130**(16), 164101 (2009)
76. L. Marcucci, L. Truskinovsky, Mechanics of the power stroke in myosin II. Phys. Rev. E **81**(5), 051915 (2010)
77. P. Martin, A.D. Mehta, A.J. Hudspeth, Negative hair-bundle stiffness betrays a mechanism for mechanical amplification by the hair cell. PNAS **97**(22), 12026–12031 (2000)
78. J.L. Mateos, F. Alatriste, Brownian motors and stochastic resonance. Chaos **21**(4) (2011)
79. J. Menche, L. Schimansky-Geier, Two particles with bistable coupling on a ratchet. Phys. Lett. A **359**(2), 90–98 (2006)
80. E. Meyhöfer, J. Howard, The force generated by a single Kinesin molecule against an elastic load. Proc. Nat. Acad. Sci. U.S.A. **92**(2), 574–578 (1995)
81. M.M. Millonas, M.I. Dykman, Transport and current reversal in stochastically driven ratchets. Phys. Lett. A **185**(1), 65–69 (1994)
82. A. Mogilner, A.J. Fisher, R.J. Baskin, Structural changes in the neck linker of Kinesin explain the load dependence of the motor's mechanical cycle. J. Theor. Biol. **211**(2), 143–157 (2001)
83. A. Månsson, Actomyosin-ADP states, interhead cooperativity, and the force-velocity relation of skeletal muscle. Biophys. J. **98**(7), 1237–1246 (2010)
84. A. Muhlrad, Y.M. Peyser, M. Nili, K. Ajtai, E. Reisler, T.P. Burghardt, Chemical decoupling of ATPase activation and force production from the contractile cycle in myosin by steric hindrance of lever-arm movement. Biophys. J. **84**(2), 1047 (2003)
85. M.A. Muñoz, F.D.L. Santos, M.M.T.D. Gama, Generic two-phase coexistence in nonequilibrium systems. Eur. Phys. J. B **43**(1):73–79 (2005)
86. K.H. Nagai, Y. Sumino, R. Montagne, I.S. Aranson, H. Chaté, Collective motion of self-propelled particles with memory. Phys. Rev. Lett. **114**(16), 168001 (2015)

87. E. Pate, G. Wilson, M. Bhimani, R. Cooke, Temperature-dependence of the inhibitory of effects on orthovanadate on shortening velocity in fast skeletalimuscle. Biophys. J. **66**(5), 1554–1562 (1994)
88. G. Piazzesi, V. Lombardi, A cross-bridge model that is able to explain mechanical and energetic properties of shortening muscle. Biophys. J. **68**(5), 1966–1979 (1995)
89. K.R. Pilkiewicz, J.D. Eaves, Reentrance in an active glass mixture. Soft Matter **10**(38), 7495–7501 (2014)
90. M. Porto, Molecular motor based entirely on the coulomb interaction. Phys. Rev. E **63**(3), 030102 (2001)
91. J. Prost, J.-F. Chauwin, L. Peliti, A. Ajdari, Asymmetric pumping of particles. Phys. Rev. Lett. **72**(16), 2652 (1994)
92. G. Puglisi, L. Truskinovsky, Cohesion-decohesion asymmetry in geckos. Phys. Rev. E **87**(3), 032714 (2013)
93. H. Qian, Vector field formalism and analysis for a class of thermal ratchets. Phys. Rev. Lett. **81**(15), 3063–3066 (1998)
94. P. Recho, L. Truskinovsky, Asymmetry between pushing and pulling for crawling cells. Phys. Rev. E **87**(2), 022720 (2013)
95. P. Reimann, Brownian motors: noisy transport far from equilibrium. Phys. Rep. **361**(2–4), 57–265 (2002)
96. P. Reimann, Brownian motors: noisy transport far from equilibrium. Phys. Rep. **361**(2–4), 57–265 (2002)
97. P. Reimann, C. Van den Broeck, H. Linke, P. Hänggi, J.M. Rubi, A. Pérez-Madrid, Giant acceleration of free diffusion by use of tilted periodic potentials. Phys. Rev. Lett. **87**(1), 010602 (2001)
98. H. Risken, *The Fokker–Planck Equation* (Springer, Berlin, 1989)
99. V.M. Rozenbaum, Y.A. Makhnovskii, S.-Y. Sheu, D.-Y. Yang, S.H. Lin, Two-state brownian motor driven by synchronously fluctuating unbiased forces. Phys. Rev. E **84**(2), 021104 (2011)
100. P. Sarkar, A.K. Maity, A. Shit, S. Chattopadhyay, J.R. Chaudhuri, S.K. Banik, Controlling mobility via rapidly oscillating time-periodic stimulus. Chem. Phys. Lett. **602**, 4–9 (2014)
101. P. Sarkar, A. Shit, S. Chattopadhyay, S. K. Banik, Profiling the overdamped dynamics of a nonadiabatic system. Chem. Phys. **458**, 86–91 (2015)
102. S. Savel'ev, F. Marchesoni, F. Nori, Stochastic transport of interacting particles in periodically driven ratchets. Phys. Rev. E **70**(6), 061107 (2004)
103. G. Schappacher-Tilp, T. Leonard, G. Desch, W. Herzog, A novel three-filament model of force generation in eccentric contraction of skeletal muscles. PLoS One **10**(3), e0117634 (2015)
104. M.J. Schnitzer, K. Visscher, S.M. Block, Force production by single Kinesin motors. Nat. Cell Biol. **2**(10), 718–723 (2000)
105. K. Sekimoto, Kinetic characterization of heat bath and the energetics of thermal ratchet models. J. Phys. Soc. Jpn. **66**(5), 1234–1237 (1997)
106. M. Sheinman, C.P. Broedersz, F.C. MacKintosh, Actively stressed marginal networks. Phys. Rev. Lett. **109**(23), 238101 (2012)
107. R. Sheshka, P. Recho, L. Truskinovsky, Rigidity generation by nonthermal fluctuations. Phys. Rev. E **93**(5), 052604 (2016)
108. R. Sheshka, L. Truskinovsky, Power-stroke-driven actomyosin contractility. Phys. Rev. E **89**(1), 012708 (2014)
109. D.A. Smith, M.A. Geeves, J. Sleep, S.M. Mijailovich, Towards a unified theory of muscle contraction. I: foundations. Ann. Biomed. Eng. **36**(10), 1624–1640 (2008)
110. A.P. Solon, J. Stenhammar, R. Wittkowski, M. Kardar, Y. Kafri, M.E. Cates, J. Tailleur, Pressure and phase equilibria in interacting active Brownian spheres. Phys. Rev. Lett. **114**(19), 198301 (2015)
111. H. Sugi, T. Kobayashi, T. Tsuchiya, S. Chaen, S. Sugiura, Evidence for the essential role of myosin head lever arm domain and myosin subfragment-2 in muscle contraction, in Skeletal Muscle—From Myogenesis to Clinical Relations, ed. by J. Cseri, chap. 6 (InTech, 2012), pp. 125–140

112. H. Sugi, H. Minoda, Y. Inayoshi, F. Yumoto, T. Miyakawa, Y. Miyauchi, M. Tanokura, T. Akimoto, T. Kobayashi, S. Chaen, et al., Direct demonstration of the cross-bridge recovery stroke in muscle thick filaments in aqueous solution by using the hydration chamber. Proc. Nat. Acad. Sci. U.S.A. **105**(45), 17396–17401 (2008)
113. H.L. Sweeney, A. Houdusse, Structural and functional insights into the myosin motor mechanism. Annu. Rev. Biophys. **39**, 539–557 (2010)
114. S.C. Takatori, J.F. Brady, Forces, stresses and the (thermo?) dynamics of active matter. Curr. Opin. Colloid Interface Sci. **21**, 24–33 (2016)
115. T. Tomé, M.J. de Oliveira, Dynamic phase transition in the kinetic Ising model under a time-dependent oscillating field. Phys. Rev. A **41**(8), 4251 (1990)
116. G. Tsiavaliaris, S. Fujita-Becker, D.J. Manstein, Molecular engineering of a backwards-moving myosin motor. Nature **427**(6974), 558–561 (2004)
117. M. Tyska, D. Warshaw, The myosin power stroke. Cell Mot. Cytoskel. **51**(1), 1–15 (2002)
118. C. Van den Broeck, J.M.R. Parrondo, R. Toral, Noise-induced nonequilibrium phase transition. Phys. Rev. Lett. **73**(25), 3395 (1994)
119. C. Veigel, C.F. Schmidt, Moving into the cell: single-molecule studies of molecular motors in complex environments. Nat. Rev. Mol. Cell Bio. **12**(3), 163–176 (2011)
120. A. Vilfan, T. Duke, Instabilities in the transient response of muscle. *Biophys. J.* **85**(2), 818–827 (2003)
121. A. Vilfan, T. Duke, Synchronization of active mechanical oscillators by an inertial load. Phys. Rev. Lett. **91**(11), 114101 (2003)
122. A. Vilfan, E. Frey, F. Schwabl, Force-velocity relations of a two-state crossbridge model for molecular motors. Europhys. Lett. **45**(3), 283–289 (1999)
123. K. Visscher, M.J. Schnitzer, S.M. Block, Single Kinesin molecules studied with a molecular force clamp. Nature **400**(6740), 184–189 (1999)
124. S. von Gehlen, M. Evstigneev, P. Reimann, Dynamics of a dimer in a symmetric potential: Ratchet effect generated by an internal degree of freedom. Phys. Rev. E **77**(3), 031136 (2008)
125. S. Walcott, P. Fagnant, K. Trybus, D. Warshaw, Smooth muscle heavy meromyosin phosphorylated on one of its two heads supports force and motion. J. Biol. Chem. **284**(27), 18244–18251 (2009)
126. H. Wang, G. Oster, Ratchets, power strokes, and molecular motors. Appl. Phys. A **75**(2), 315–323 (2002)
127. H. J. Woo, C.L. Moss, Analytical theory of the stochastic dynamics of the power stroke in nonprocessive motor proteins. Phys. Rev. E **72**(5), 051924 (2005)
128. M.T. Woodside, C. García-García, S.M. Block, Folding and unfolding single rna molecules under tension. Curr. Opin. Chem. Biol. **12**(6), 640–646 (2008)
129. A.A. Zaikin, J. Kurths, L. Schimansky-Geier, Doubly stochastic resonance. Phys. Rev. Lett. **85**(2), 227 (2000)
130. X.-J. Zhang, H. Qian, M. Qian, Stochastic theory of nonequilibrium steady states and its applications. Part I. Phys. Rep. **510**(1), 1–86 (2012)